UNIVERSIDADE FEDERAL DE VIÇOSA

NANOFABRICATION AND INVESTIGATION OF GROUND STATE DEGENERACY IN ARTIFICIAL SPIN ICE LATTICES

Lara Braga de Oliveira
Magister Scientiae

VIÇOSA - MINAS GERAIS
2024

LARA BRAGA DE OLIVEIRA

NANOFABRICATION AND INVESTIGATION OF GROUND STATE DEGENERACY IN ARTIFICIAL SPIN ICE LATTICES

Dissertation submitted to the Physics Graduate Program of the Universidade Federal de Viçosa in partial fulfillment of the requirements for the degree of *Magister Scientiae*.

Adviser: Clodoaldo I L de Araujo

VIÇOSA - MINAS GERAIS
2024

Ficha catalográfica elaborada pela Biblioteca Central da Universidade Federal de Viçosa - Campus Viçosa

T
O48n
2024

Oliveira, Lara Braga de, 1999-
Nanofabrication and investigation of ground state degeneracy in artificial spin ice lattices / Lara Braga de Oliveira. – Viçosa, MG, 2024.
1 dissertação eletrônica (96 f.): il. (algumas color.).

Inclui apêndice.
Orientador: Clodoaldo Irineu Levartoski de Araujo.
Dissertação (mestrado) - Universidade Federal de Viçosa, Departamento de Física, 2024.
Referências bibliográficas: f. 89-95.
DOI: https://doi.org/10.47328/ufvbbt.2024.733
Modo de acesso: World Wide Web.

1. Campos eletromagnéticos. 2. Monopoles magneticos. 3. Látices (Física). I. Araujo, Clodoaldo Irineu Levartoski de, 1977-. II. Universidade Federal de Viçosa. Departamento de Física. Programa de Pós-Graduação em Física. III. Título.

CDD 22. ed. 539.7546

Bibliotecário(a) responsável: Euzébio Luiz Pinto CRB-6/3317

LARA BRAGA DE OLIVEIRA

NANOFABRICATION AND INVESTIGATION OF GROUND STATE DEGENERACY IN ARTIFICIAL SPIN ICE LATTICES

Dissertation submitted to the Physics Graduate Program of the Universidade Federal de Viçosa in partial fulfillment of the requirements for the degree of *Magister Scientiae*.

APPROVED: August 8, 2024.

Assent:

Lara Braga de Oliveira
Author

Clodoaldo Irineu Levartoski de Araujo

ACKNOWLEDGMENTS

I am a very lucky person to have people in my life who inspire, support, encourage and teach me every day. Without them, nothing makes sense, and for that I would like to thank them with all my heart.

Firstly, I would like to thank my parents, Eliane and Geraldo, for being my greatest example of honesty, humility, commitment and determination. Thank you for going to great lengths to help me complete my studies, often giving up your own dreams so that I could achieve mine. I love you more than anything and I hope I can repay everything you have always done and continue to do for me. My sister Luiza, being my first best friend, is the person I always turn to in the most difficult moments. Furthermore, she was the one who gave me and my family the greatest joy and the most beautiful gift we could receive: José Miguel, my dear nephew and godson. I hope to introduce Physics to him and make him fall in love with science, my dear Zuzu.

I am immensely grateful to my life partner, Mateus, for always encouraging me, cheering me, and being my best friend. Thank you for making me laugh during tough times and for being by my side to celebrate the good moments. You are the calm amidst the chaos, and with you, I am much happier. To my godmother Elisete, for being my second mother and my great role model as a woman, teacher, and activist. I will be eternally grateful for everything you do for me. To my aunt Eliza, because it was thanks to her, who opened her home to me, that I have valued public, free, and quality education from a very young age.

To my advisor Clodoaldo for the numerous teachings, advice, opportunities, encouragement, and of course, for the patience. I have learned much more than physics during these three years under your excellent guidance.

To my childhood and teenage friends: Clara, Nina, Biel, Duda, Isa, Let, Lice, Ju, Vitor, and João. Despite the physical distance, you have always been present in the best way possible. I am a bit of each of you. My physicist friends: Hugo, Thai, Emílio, Ju, Gustim, Karol, and Vic, for being the main reason I stayed in Viçosa for so long. You made this journey much more enjoyable. I also apologize for all the times I pestered you with so many doubts, as not everyone has such incredible and intelligent friends! I am very lucky. I also thank the other colleagues from the `lower room' and `upper room' for all the support and great conversations. To Bel, with whom I shared a home for 6 years, and Duda, my great partner in laughter and craziness. Although we grew up in the same city, it was in Viçosa that I got closer to them and had the opportunity to know how amazing they are. To República Interditados, for providing me with great friendships, laughter, and good barbecues.

I thank my research group, especially Hamilton, Eloi, and Daniel, for all the support and teachings.

Finally, I thank the Fundação de Amparo à Pesquisa do Estado de Minas Gerais (FAPEMIG) for the financial support in research projects. This study was financed in part by the Coordenação de Aperfeiçoamento de Pessoal de Nível Superior – Brasil (CAPES) – Finance Code 001.

Se o ar não se movimenta, não tem vento; se a gente não se movimenta, não tem vida - Itamar Vieira Junior, Torto Arado

ABSTRACT

OLIVEIRA, Lara Braga de, M.Sc., Universidade Federal de Viçosa, August, 2024. **Nanofabrication and Investigation of Ground State Degeneracy in Artificial Spin Ice Lattices**. Adviser: Clodoaldo Irineu Levartoski de Araujo.

Arrays of geometrically frustrated nanomagnets known as artificial spin ices (ASIs) have been proposed as an intriguing system for investigating collective excitations that behave as emergent magnetic monopoles at room temperature. This was only made possible due to advances in lithography techniques, enabling the nanofabrication of two-dimensional lattices with potential use in devices. However, in general, in these artificial systems, emergent magnetic monopoles cannot move freely as in their natural counterpart because energy strings connecting monopoles of opposite charges arise. Furthermore, the energy of the string connecting them is strictly related to the non-degeneracy of the ground state. Therefore, several theoretical works have proposed that two-dimensional lattices with specific geometries could exhibit a highly degenerate ground state and, consequently, free monopoles in the lattice. Such specific geometries are rectangular arrays of disconnected nanomagnets, where the ratio between the horizontal and vertical distances between them is equal to square root of three; and connected square arrays of nanomagnets. In this context, the present work aimed to experimentally investigate the proposed degeneracy in such ASI geometries through characterization techniques such as magnetic force microscopy and magnetoresistance. Additionally, these systems are usually fabricated by nanofabrication processes involving expensive and time-consuming physical vapor deposition techniques. As a possible solution to this problem, we present a new nanofabrication route using the electrodeposition technique for the growth of Permalloy, offering an alternative to manufacture ASIs quickly and affordably.

Keywords: artificial spin ice; ground state degeneracy; electrodeposition

RESUMO

OLIVEIRA, Lara Braga de, M.Sc., Universidade Federal de Viçosa, agosto de 2024. **Nanofabricação e Investigação da Degenerescência do Estado Fundamental em Redes de Gelos de Spin Artificiais**. Orientador: Clodoaldo Irineu Levartoski de Araujo.

Matrizes de nanomagnetos geometricamente frustrados, denominadas spin ices artificiais (ASIs), foram propostas como um sistema interessante para investigar excitações coletivas que se comportam como monopolos magnéticos emergentes à temperatura ambiente. Isso só foi possível devido à avanços nas técnicas de litografia, que possibilitaram a nanofabricação de redes bidimensionais com potencial uso em dispositivos. Porém, em geral, nesses sistemas artificiais os monopolos magnéticos emergentes não podem se mover livremente como em sua contraparte natural, uma vez que surgem cordas energéticas conectando os monopolos de cargas opostas. Ademais, a energia da corda que os conecta está estritamente relacionada à não degenerescência do estado fundamental. Por isso, diversos trabalhos teóricos propuseram que redes bidimensionais com geometrias específicas poderiam apresentar um estado fundamental altamente degenerado e, consequentemente, monopolos livres na rede. Tais geometrias específicas são as redes retangulares de nanomagnetos não conectados, cuja razão entre as distâncias horizontal e vertical entre eles é igual a raiz quadrada de três; e redes quadradas de nanomagnetos conectados. Neste aspecto, o presente trabalho pretendeu investigar experimentalmente a degenerescência proposta em tais geometrias de ASIs através de técnicas de caracterização por microscopia de força magnética e magnetorresistência. Além disso, esses sistemas são usualmente fabricados por processos de nanofabricação envolvendo técnicas caras e demoradas de deposição física de vapor. Como possível solução para este problema, também apresentamos uma nova rota de nanofabricação usando a técnica de eletrodeposição para crescimento de Permalloy, oferecendo uma alternativa para fabricar ASIs de forma rápida e de baixo custo.

Palavras-chave: gelo de spin artificial; degenerescência do estado fundamental; eletrodeposição

List of Figures

List of Acronyms and Abbreviations

AMR	Anisotropic Magnetoresistance
ASI	Artificial Spin Ice
DPF	Department of Physics
EBL	Electron-beam lithography
EDS	Energy Dispersion Spectroscopy
FEG	Field Emission Gun
FQHE	Fractional Quantum Hall Effect
GMR	Giant Magnetoresistance
INL	Iberian Institute of Nanotechnology
IQHE	Integer Quantum Hall Effect
MFM	Magnetic Force Microscopy
MR	Magnetoresistance
MSF	Magnetic Structure Factor
OMR	Ordinary Magnetoresistance
SEM	Scanning Electron Microscope
UFV	Universidade Federal de Viçosa

Contents

1 Introduction

Different alternatives for improving the transport, processing and storage data information have been investigated with the aim of enabling the development of high efficiency technologies with low energy costs. In this aspect, several properties and phenomena involving magnetic materials have proven extremely interesting for this purpose, as occurs with the so-called *spin ices*, the central focus of this work. They are geometrically frustrated magnetic materials, increasingly studied due to their great technological potential to contribute, for example, to advances in areas such as mangetricity [21], which involves transport of magnetic charges with less energy dissipation than in electricity with transport of electrical charges. They have also been important for advances in other areas such as magnonics, which investigates the effect of spin wave propagation in nanomagnetic materials [22], and even neuromorphic computing [23].

Spin ices are found in nature in the form of crystalline structures with pyrochlore-type lattices, such as the rare-earth oxides $Dy_2Ti_2O_7$, $Ho_2Sn_2O_7$ and $Ho_2Ti_2O_7$ [24]. Their important property of geometric frustration causes them to possess a highly macroscopically degenerate ground state that follows the Pauling's ice rule. However, the presence of high-energy vertices in the crystal violating this rule own it to exhibit collective excitations behaving like magnetic monopoles connected by a non-energetic Dirac string [25]. Such absence of energy in the string is strictly related to the degeneracy of the ground state, and allows a certain freedom of movement of the monopoles in the lattice. Although this property makes such crystals excellent objects of study, they are difficult to reproduce in laboratory and have impractical application in devices.

Due to advances in lithography techniques, a two-dimensional system called artificial spin ice (ASI) [8], usually composed of Permalloy, was created with the aim of trying to imitate the main properties of natural ones, but with some advantages: greater reprodutibility and applicability in devices, control of geometry and dimensions of the nanomagnets forming the lattice, possibility of probing the system's individual magnetic moments, ease of exploring degenerate states, more stability at room temperature due to the greater intensity of magnetic moments, among others [6, 9, 26].

Nevertheless, in most two-dimensional geometries, the monopole-antimonopole pairs are connected by an energetic string, limiting their movement in the lattice. Aiming

to reduce this energy, researchers from the Department of Physics at Universidade Federal de Viçosa (UFV) showed in [27–29] that in the case of non-thermodynamic unconnected samples, there is a considerable decrease in the energy of the string in rectangular geometries, more specifically when the ratio between the horizontal and vertical distances between nanomagnets is equal to $\sqrt{3}$. For non-thermodynamic samples of connected nanomagnets, the degeneracy of the ground state is related to the appearance of magnetic domain walls whose behavior resembles that of monopoles emerging from unconnected lattices. In this case, degeneracy is observed in square geometry, as predicted in literature [12].

The objective of this work was to experimentally verify the degeneracies theoretically predicted for the aforementioned geometries. To achieve this, topological, magnetic, and transport characterizations were performed on connected and unconnected samples of different geometries. More specifically, the studied geometries of two-dimensional spin ices included square and rectangular lattices, with the ratio between the horizontal and vertical distances of the nanomagnets varying between 1, $\sqrt{2}$, $\sqrt{3}$ and $\sqrt{4}$. Additionally, this work also aimed to explore nanofabrication techniques for samples, presenting prosperous and innovative results regarding the fabrication of spin ices using the electrodeposition technique. This method offers several advantages over sputtering, the most commonly used technique for this type of fabrication.

Therefore, this work is organized as follows: In Chapter 2, a literature review of the main concepts in the field of magnetism essential for understanding spin ices will be provided. Chapter 3 details some concepts of condensed matter physics, also crucial for understanding the main topic of this work. Chapter 4 defines natural and artificial spin ices and includes literature reviews of some of the main studies on the degeneracy of ground states in these systems. Chapter 5 explains the experimental techniques used in this work, both for nanofabrication and characterization. Chapter 6 details the measurement processes and results obtained, along with discussions of these results. Finally, Chapter 7 describes the main conclusions of the work. Three articles have been published as a result of this work and are referenced in the appendix of this dissertation.

2 Important Definitions in Magnetism

2.1 Dipolar Interaction

Dipolar interaction occurs due to the interaction between magnetic dipoles that constitute a system, and has a purely magnetic origin. In other words, it is caused exclusively due to the influence that one dipole exerts on another, and to better understand it, we will first address the definition of a *magnetic dipole*. Intuitively, it can be thought of as approached by Gilbert model (Fig. 1**(a)**), in which there are positive and negative 'magnetic charges' (or north and south 'poles'), separated by a small distance, just as occurs in electric dipoles (Fig. 1**(b)**). Although there are several similarities in some equations involving the magnetic ($\mathbf{m}$) and electric ($\mathbf{p}$) dipole moments, it is necessary to emphasize that magnetic monopoles are not found freely in nature as is the case with electrical charges, as expressed in Gauss's law for magnetism ($\nabla \cdot \mathbf{B} = 0$). Therefore, a more realistic and necessary definition for solving some problems involves treating magnetic dipoles as tiny current loops (Fig. 1**(c)**), since magnetism comes from moving electrical charges, and not from 'magnetic charges' [1]. However, within the scope of this work it is sufficient to think of magnetic dipoles according to Gilbert model, but with the magnetic poles separated by a very small distance, so that the dipole moment is basically centered at one point.

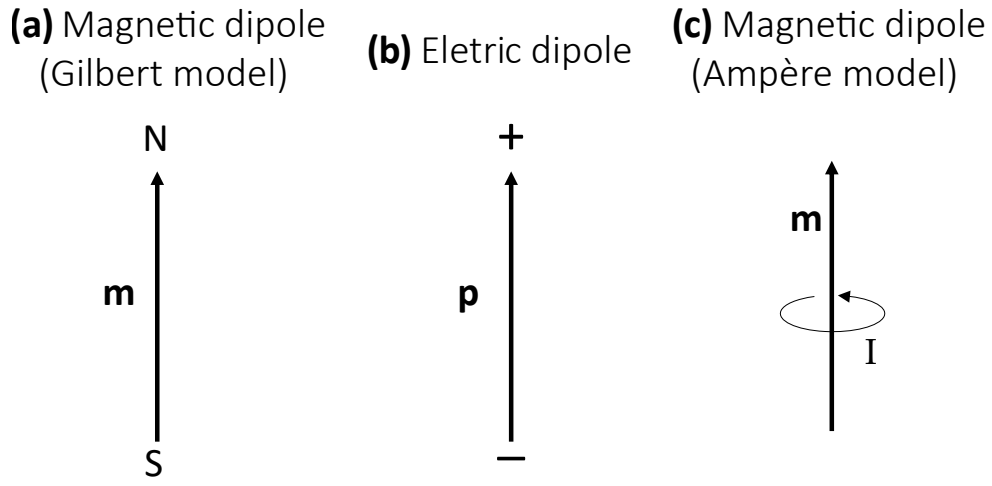

Figure 1: Description of magnetic and electric dipoles. Figure adapted from Ref. [1].

Let $\mathbf{m}_j$ be the magnetic moment of a dipole located at position $\mathbf{r}_j$. The magnetic field generated by this magnetic dipole at a certain point located in $\mathbf{r}_i$ is given by Eq. 2.1:

$$\mathbf{B}_{dip}(\mathbf{r}_i) = \frac{\mu_0}{4\pi r_{ij}^3}\left[3(\mathbf{m}_j \cdot \hat{r}_{ij})\hat{r}_{ij} - \mathbf{m}_j\right] \tag{2.1}$$

Where μ_0 is the vacuum magnetic permeability, $\mathbf{r}_{ij}$ is the position vector that connects the dipole in $\mathbf{r}_j$ with the point in $\mathbf{r}_i$, and $\hat{r}_{ij}$ the unit vector. Now considering a set of magnetic dipoles located at positions $\{\mathbf{r}_j\}$ and with respective moments $\{\mathbf{m}_j\}$, with j = 1,2,3... . The magnetic field in $\mathbf{r}_i$ arising from this arbitrary distribution of magnetic dipoles is given by:

$$\mathbf{B}_{dip}(\mathbf{r}_i) = \frac{\mu_0}{4\pi}\sum_{j=1}\frac{1}{r_{ij}^3}\left[3(\mathbf{m}_j \cdot \hat{r}_{ij})\hat{r}_{ij} - \mathbf{m}_j\right] \tag{2.2}$$

Regarding the interaction energy between dipoles, we can obtain it from the energy of a dipole in the presence of a magnetic field, which is:

$$E_{dip} = -\mathbf{m} \cdot \mathbf{B} \tag{2.3}$$

In this way, it is possible to obtain the interaction energy between a dipole with moment $\mathbf{m}_i$ located at a certain position $\mathbf{r}_i$ in space, and the field generated by the distribution of dipoles described in Eq. 2.2:

$$E_{dip}^{(i)} = \frac{\mu_0}{4\pi}\mathbf{m}_i \cdot \sum_{j=1}\frac{1}{r_{ij}^3}\left[\mathbf{m}_j - 3(\mathbf{m}_j \cdot \hat{r}_{ij})\hat{r}_{ij}\right] \tag{2.4}$$

To find the energy of the dipole distribution, simply restrict the sum in j to all values $j > i$:

$$E_{dip} = \sum_i E_{dip}^{(i)} = \frac{\mu_0}{4\pi}\sum_{\substack{i,j \\ j>i}}\frac{1}{r_{ij}^3}\left[\mathbf{m}_i \cdot \mathbf{m}_j - 3(\mathbf{m}_i \cdot \hat{r}_{ij})(\mathbf{m}_j \cdot \hat{r}_{ij})\right] \tag{2.5}$$

Therefore, it is possible to see that the energy between dipoles depends on the distance and the degree of alignment between them, being a long-range energy as it decays smoothly with $\frac{1}{r_{ij}^3}$. To illustrate, consider two dipoles separated by a distance r = 1 Å, with magnetic moments of magnitude $m_1 = m_2 = \mu_B$, and with μ_B being the Bohr magneton. Furthermore, consider that the magnetic moments are aligned parallel to each other, i.e., they are ferromagnetically ordered (Fig. 2). In this case, the interaction energy between the moments is of the order of 10^{-24} J, which corresponds to a temperature

of approximately 1K according to the relation $E = k_B T$, where k_B is the Boltzmann constant. However, in general, ferromagnetic materials order themselves at much higher temperatures: for example, the Curie temperature [1] of materials such as iron (Fe), cobalt (Co) and nickel (Ni) are 1043 K, 1388 K and 627 K, respectively. Therefore, ferromagnetic ordering could not be explained by dipolar interaction.

2.2 Exchange Interaction

To explain room-temperature ferromagnetic ordering in certain materials, it is necessary to introduce another interaction, the so-called *exchange interaction*. It has a purely quantum origin, caused by overlap of the electronic wave functions. It is strictly related to the Pauli exclusion principle, which establishes that two or more identical fermions cannot occupy the same quantum state simultaneously. Due to the quantum origin, the interaction strength decreases rapidly with distance and it is a short-range interaction, so that only interactions between nearest neighbors are relevant [30].

In 1928, the German physicist Werner Heisenberg developed, for the first time, a theoretical model capable of describing this interaction and explaining magnetic ordering in matter through the Hamiltonian that bears his name, the Heisenberg Hamiltonian:

$$H = -\sum_{<i,j>} J_{ij}\, \mathbf{S}_i \cdot \mathbf{S}_j \tag{2.6}$$

Where $<i,j>$ indicates a sum over only the nearest neighbours and J_{ij} is the so-called *exchange constant*. Here, it is convenient to adopt a classical spins model, or *Ising spins* [2], represented by the variable $\mathbf{S}$ with the spins $\mathbf{S}_i$ and $\mathbf{S}_j$ located in sites i and j of the lattice, respectively. If $J_{ij} > 0$, the energy is minimized when the spins are parallel to each other ($\mathbf{S}_i \cdot \mathbf{S}_j > 0$) and they align ferromagnetically. For $J_{ij} < 0$, the antiparallel orientation between the spins is favored ($\mathbf{S}_i \cdot \mathbf{S}_j < 0$), and an antiferromagnetic order is established (Fig. 2).

[1] The Curie temperature or Curie point corresponds to the temperature at which a ferromagnetic material loses its ferromagnetic ordering properties and starts to behave like a paramagnet, in which the magnetic moments are disordered.

[2] The Ising model is a statistical model of magnetism with classical spins, called Ising spins, represented by a variable S that can assume two states, +1 (spin up) or -1 (spin down), so that its orientation is restricted to just one direction. Furthermore, the interaction occurs between the nearest neighbours. It was proposed by Wilhelm Lenz in 1920 and solved analytically in one dimension by Ising in 1925. In two dimensions the model was only solved in 1942 by Onsager, and there is still no exact calculation for three spatial dimensions [30].

When the material has an ordered ferromagnetic phase, spontaneous magnetization is observed, that is, its magnetization can be different from zero even in the absence of the applied magnetic field. In antiferromagnets, as the spins are antiparallel, the net momentum is zero even at temperatures lower than the ordering temperature, called *Néel temperature* [3]. It may happen that there is zero spontaneous magnetization in a sample even though it is in its ferromagnetic phase due to cancellation effects between magnetic domains, a concept that will be discussed in the next section, as a result of the dipolar interaction being relevant at long range [30].

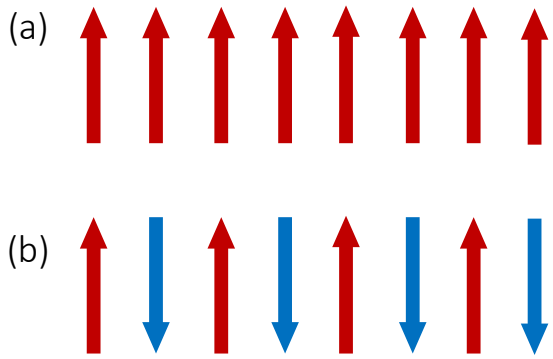

Figure 2: Illustration of a one-dimensional lattice ordered **(a)** ferromagnetically; **(b)** antiferromagnetically. For the case **(a)**, we have in Eq. 2.6 the parameter $J_{ij} > 0$; and for the case **(b)** we have $J_{ij} < 0$.

For systems where both interactions play a significant role, and describing the magnetic moments in terms of an Ising spin ($\mathbf{m}_i = m\mathbf{S}_i$) in Eq. 2.5, the total Hamiltonian of the system would be given by:

$$H = -\sum_{<i,j>} J_{ij}\ \mathbf{S}_i \cdot \mathbf{S}_j + \frac{\mu_0 m^2}{4\pi} \sum_{\substack{i,j \\ j>i}} \frac{1}{r_{ij}^3} \left[\mathbf{S}_i \cdot \mathbf{S}_j - 3(\mathbf{S}_i \cdot \hat{r}_{ij})(\mathbf{S}_j \cdot \hat{r}_{ij})\right] \tag{2.7}$$

With the first term referring to the exchange interaction between the spins and the second referring to the dipolar interaction between all of them. For materials such as Fe and Ni, for example, the exchange interaction is much more relevant than the dipolar one, and the system is ordered ferromagnetically, meaning the latter interaction can be neglected. In systems such as spin ice, the central theme of this work, both interactions are relevant when it comes to systems found in nature. For artificial spin ices, only the dipolar interaction is significant. More details about this will be discussed later.

[3] Above a specific temperature for each antiferromagnet, called the Néel temperature, the material ceases to be in the antiferromagnetic phase and enters the paramagnetic phase, meaning the magnetic moments become disordered. In this sense, the Néel temperature for antiferromagnets is analogous to the Curie temperature for ferromagnets.

2.3 Magnetic Domains

Ferromagnetic materials at temperatures much lower than the Curie temperature tend to have their magnetic moments parallelly aligned due to the exchange interaction, as explained above, even in the absence of an external magnetic field. However, the magnetostatic energy required to keep all the magnetic moments of the material aligned in the same direction (Fig. 3**(a)**), ensuring uniform magnetization, is relatively high. Therefore, this configuration is not energetically stable. In a configuration where half of the magnetic moments of the material are aligned in one direction and the other half in the opposite direction (Fig. 3**(b)**), the magnetic field generated by the poles at the ends will be smaller, and consequently, the magnetostatic energy will also decrease by approximately half compared to the situation in **(a)**. A configuration that further reduces the energy of the system is shown in Fig. 3**(c)**, where there are small regions with different magnetizations, so that each one of them has its magnetization saturated in a given direction. These regions are called *magnetic domains*, and despite having an internal net magnetization, the average magnetization of the material is insignificant [2].

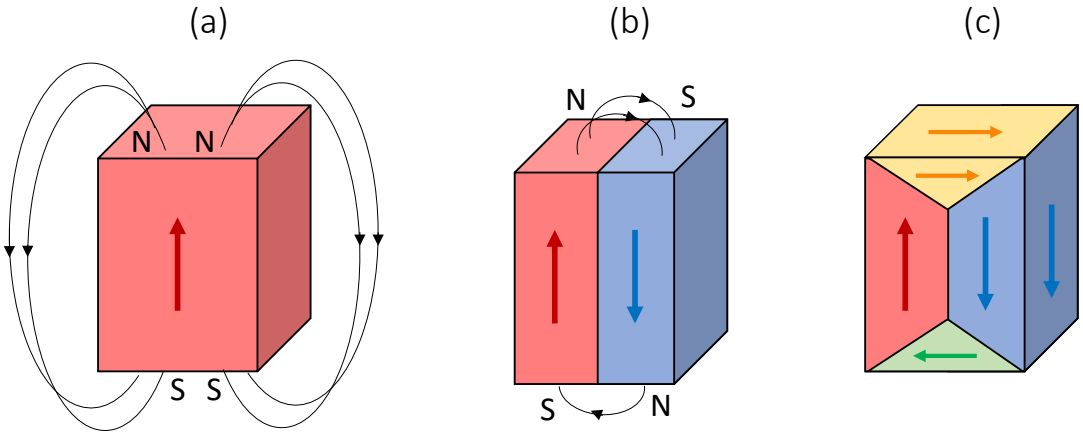

Figure 3: Illustration of magnetic domains formed in a system. Each color represents a domain whose magnetization within it is saturated in a given direction. The magnetostatic energy of **(a)** is greater than that of **(b)**, which is greater than that of **(c)**. Figure adapted from Ref. [2].

In this way, the formation of magnetic domains always results from the minimization of the system energy, going from a high-energy configuration with total saturated magnetization to a lower-energy configuration with small regions within the local magnetization saturated. Additionally, the Russian physicists Landau and Lifshitz showed that the formation of domains is a consequence of the contributions from exchange energy,

magnetostatic energy, Zeeman energy (due to the interaction of the moments with the externally applied field), and the magnetocrystalline anisotropy energy [2, 31]. This last one tends to direct the magnetization vector along certain crystallographic axes of the ferromagnetic material, called *directions of easy magnetization*, due to the interaction between the orbital angular momentum and the electric field of the crystal lattice.

The narrow region separating the magnetic domains is called *domain wall* (Fig. 4), with a typical thickness of about 100 to 1000 nm (while the domains can range from μ m to mm, depending on the material and applied field) [2]. In this region, the orientation of the moments varies gradually from one domain to another, otherwise the exchange energy would be very high. As the spins contained in the wall are not oriented along the axis of easy magnetization, there is a magnetocrystalline anisotropy energy associated with this wall that is approximately proportional to its width and limits its size. However, domain walls can easily move through the material and change in size with the application of external parameters such as magnetic field or electric current [31].

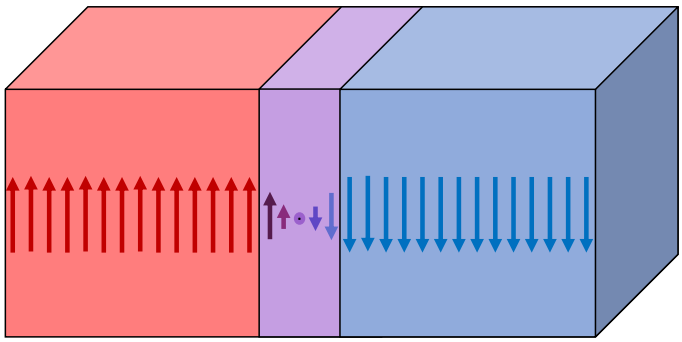

Figure 4: Illustration of a domain wall, represented in the image by the color purple. Figure adapted from Ref. [2].

The magnetic domains are capable of dictating how the magnetization (M) of the material behaves as a function of the external magnetic field (H). For the case of an initially demagnetized ferromagnetic material, it is possible to observe the behavior indicated in Fig. 5**(a)**. As long as the applied field is low, the domain walls can shift reversibly, and removing the field the domains return to their initial configuration. As the field intensity increases, the wall displacements become irreversible due to imperfections, and the magnetization also increases, until the field is high enough to rotate all domains and completely saturate the magnetization.

After the material is initially magnetized, with its magnetic moments all saturated in a given direction, it is possible to probe what happens to M if we vary both the intensity

and the direction of H. This behavior is described in the so-called *hysteresis curve*, which can be seen in Fig. 5**(b)**. Analyzing the curve, it is clear that when H gradually decreases, M does not return through the same curve referring to its increase, because due to the effects of rotations and irreversible displacements, part of the magnetic domains remains in the same initial direction. Thus, even when there is no field being applied ($H = 0$), there is a non-zero magnetization ($M = M_r$), called *remanent magnetization*, or *remanence*. As H increases its intensity in the opposite direction to the initial magnetization, the material becomes increasingly demagnetized, until it has zero magnetization at $H = -H_c$, called *coercive field* or *coercivity*. Continuing to increase the intensity of H, the magnetic domains will align until the material completely saturates the magnetization in the opposite direction, and the cycle repeats itself reversing the direction of the field again.

It is interesting to mention that the domains do not occur exclusively in ferromagnets, as they are also formed in antiferromagnetic, ferroelectric, antiferroelectric, superconducting materials, among others [31].

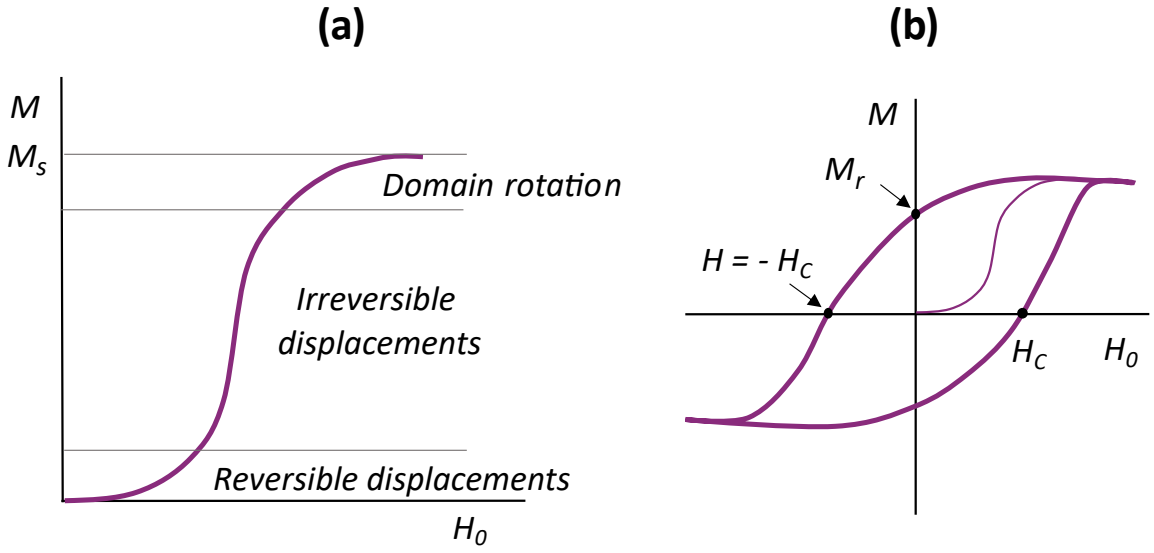

Figure 5: Variation of the magnetization of a ferromagnetic material under an applied external field. **(a)** Sample initially demagnetized. **(b)** Hysteresis curve. Figure adapted from Ref. [2].

3 Crucial Concepts

3.1 Emergence

Some areas of physics aim to find and study the fundamental constituents of matter, as occurs in the field of high-energy physics, for example. In this aspect, scientific investigation relies on a reductionist vision, in the sense of a search for increasingly smaller elementary units that constitute the macroscopic universe. However, the collective behavior arising from the interaction of microscopic constituents, such as electrons, atoms, molecules and others, can provide the emergence of new phenomena and properties not observed in the individual behavior of each of them. This is the concept of *emergence* addressed in this topic, that is, the appearance of a new physical entity due to competitive interactions between many microscopic constituents of a given system [11,26,32]. If these constituents are decoupled and there are no interaction competitions between them, the collective behavior of the system will be directly related to their individual properties [26].

Due to the large number of elements involved in this type of phenomenon, it appears in condensed matter physics and is responsible for explaining several properties in different systems and materials. When it comes to solids, for example, a quantum treatment of collective behavior of atoms vibrating in a crystalline lattice provides the emergence of a collective excitation that behaves like a particle, or simply a quasiparticle, called *phonon*. More specifically, it is the quantum of energy associated with the vibrational movement of the bonded atoms constituting a crystal lattice. In this way, the system has a large number of atoms as fundamental constituents and, because they are bonded in a crystalline lattice, they have the collective behavior described by an emerging particle which is not present considering the individual behaviors of the physical entities [31].

The concept of phonon was essential in the formulation of the BCS theory[1] to explain the formation of Cooper pairs and, consequently, superconductivity at low temperatures. It also plays a fundamental role in understanding the thermal capacity of

[1] First microscopic theory to explain superconductivity at low temperatures developed by Bardeen, Cooper, and Schrieffer in 1957. In it, electrons form pairs (called Cooper pairs) by phonon-mediated interactions, and superconductivity persists in the material as long as the pairs of Cooper are not broken by a temperature, magnetic field, or electric current above a certain critical value, which depends on each material. The researchers received the Nobel Prize in Physics in 1972 for this theory. There are still no well-established theories to explain superconductivity at high temperatures.

crystal lattices [31], thermal transport in materials [33,34], among countless other contributions to solid state physics.

Another example of collective excitations behaving like emerging particles are the so-called *magnons*, discovered in 1930 by Felix Bloch [35] whose research enabled a greater understanding of the magnetic properties of matter and, consequently, new technological applications. In the case of ferromagnetic materials, for example, whose classical representation of the ground state consists of all spins pointing in one direction, it was expected that the first excited state would correspond to an inverted localized spin, as demonstrated in Fig. 6. However, Bloch showed that lower energy excitations in a spin system actually correspond to collective and non-localized spin deviations [3], the so-called spin waves (Fig. 7), differently from what had been imagined until then. Such waves can be understood as oscillations in the relative orientations of the spins in a crystalline lattice, analogously to the vibrations discussed in the case of phonons, corresponding to oscillations in the relative positions of the bonded atoms of a lattice [31]. Just as lattice vibrations are quantized through phonons, elementary spin excitations (or spin waves) are quantized through magnons, defined as the energy quantum of a spin wave.

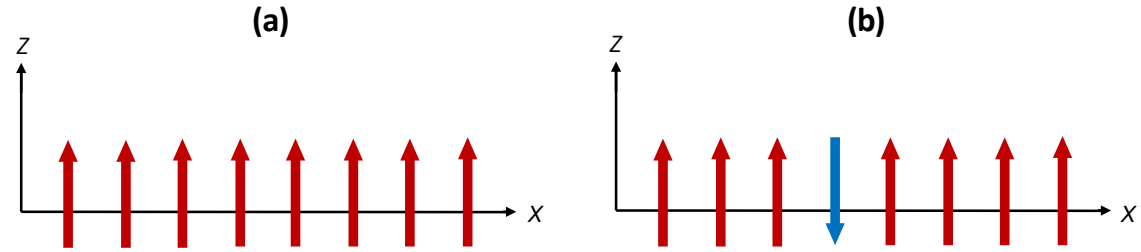

Figure 6: **(a)** Classical representation of the ground state of a linear chain of spins in a ferromagnetic material. **(b)** Classical representation of what was believed to be the first excited state: the inversion of one of the spins in the linear chain. Figure adapted from Ref. [3].

The discovery of magnons was of great importance for the advancement of spintronics, an area dedicated to the study of electron spin as the main physical entity for application in information transport, storage and processing devices. Its relevance resulted in the creation of a subarea dedicated to phenomena based on the properties of these emerging particles, called *magonics* or *magnon spintronics*, which has shown interesting application possibilities. An example is the contribution of magnons to logical processing without the need for electrical current, reducing the necessary energy consumption required in conventional electronics [3].

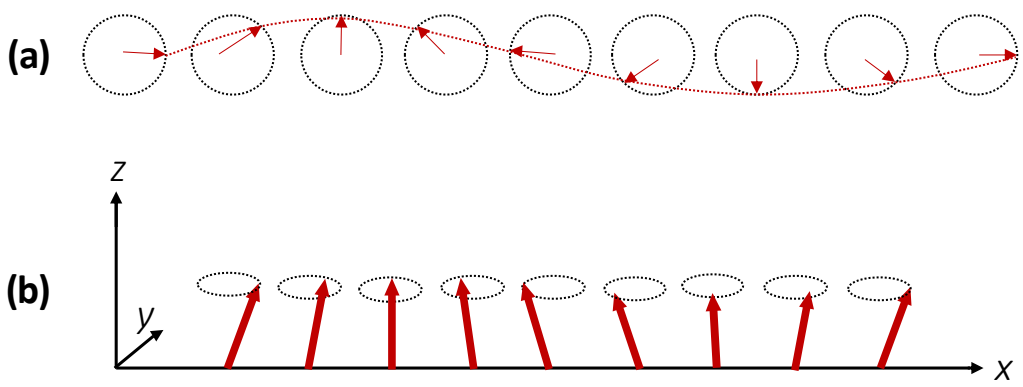

Figure 7: Illustration of a spin wave, representing the lowest energy excitations, propagating in the $+x$ direction formed by classical spins arranged one-dimensionally. Here, the spins precess with respect to the alignment direction. **(a)** Top view; **(b)** Side view; both corresponding to a wavelength. Figure adapted from Ref. [3].

There are several other emerging particles in addition to phonons and magnons discussed above, such as vortices, skyrmions, among others, with the last two being excitations of a topological character. Each of them plays an extremely important role in condensed matter physics and they all provide countless possibilities for discovering new phenomena and applications.

3.2 Fractionalization

The phenomenon of fractionalization is strictly related to emergence, considering that in many-body systems whose emerging particles present only part of certain properties of their fundamental constituents, fractionalization is said to have occurred [26, 36]. This phenomenon was approached theoretically for the first time in a one-dimensional system involving the formation of topological excitation soliton, or mobile domain wall, in the conjugated organic polymer polyacetylene [37, 38]. It was observed that a neutral soliton would have spin $\frac{1}{2}$, while a charged soliton (with charge $\pm e$) would have spin 0. Thus, in one-dimensional cases like this one, electrons behave as if they were being "split" to overcome strong Coulombic repulsion and maintain the system stable. In this way, quasi-particles emerge with only electron spin (and no charge), or only with charge (and no spin). In the former type, they are called *spinons*. In the latter, such emerging particles can have a positive charge e, called *holons*, or a negative charge $-e$, called *chargons*.

In order to exemplify fractionalization in two-dimensional systems, it is interesting

to mention the Fractional Quantum Hall Effect (FQHE), discovered experimentally in 1982 by D. C. Tsui and H. L. Stormer [39], and explained theoretically a year later by R. B. Laughlin [40]. But first of all, it is appropriate to provide a brief context of what preceded this discovery to better explain it.

In 1879, Edwin Hall discovered the (classical) Hall Effect [41], in which a transverse voltage (or Hall voltage) appears perpendicular to the electric current in a three-dimensional conductor under the influence of a magnetic field. Consequently, there is a transversal resistivity (also called *Hall resistivity*) to the current varying linearly with the field. However, at the end of the 20^{th} century, the investigation of electronic behavior in low-dimensional materials under high magnetic fields led to the discovery of new effects associated with the Hall Effect. The first of which was the so-called Integer Quantum Hall Effect (IQHE), discovered in 1980 by Klaus von Klitzing [42], who noted plateaus in transverse resistivity in relation to the high-intensity applied field at low temperatures. He realized that in these plateaus, the Hall resistivity was given exactly by $\frac{h}{e^2}\frac{1}{\nu}$, with h being the Planck constant, e the elementary charge and ν a constant that could only take on integer values. In this way, the Hall conductivity would be quantized into integer multiples of $\frac{e^2}{h}$. Basically, this effect is related to the quantization and degeneracy of Landau levels [2], so that ν can be interpreted as a filling factor for the levels. Furthermore, IQHE can be understood in terms of single-particle considerations [43].

Finally, just two years after the discovery of the IQHE, the FQHE brought to light a new and intriguing observation: the presence of quasiparticles with fractions of the elementary charge, with new Hall conductivity plateaus being a fraction of $\frac{e^2}{h}$ (with ν being able to take on non-integer values). Both effects, IQHE and FQHE, occur in two-dimensional systems, at low temperatures and are subjected to intense magnetic fields. Nevertheless, the explanation for the FQHE includes the high electron density and high electron mobility, providing strong interactions between them. Under these conditions, electrons can organize themselves to form a new state of matter, an incompressible quantum liquid [43]. Therefore, this excited state carries a fractional electrical charge so that the properties of these objects are not related to the properties of individual electrons, but rather to the properties arising from interactions between electrons.

In three spatial dimensions, fractionalization was observed in systems called spin

[2] Landau levels are the energy levels of electrons subject to a uniform magnetic field. The energy values are quantized and the levels are highly degenerate, so that the filling of the levels is proportional to the intensity of the applied field [30].

ices, the central theme of this research, and will therefore be covered in more detail in the following chapters. In this case, fractionalization occurs because emerging particles originating from excited states of the system behave as magnetic monopoles, that is, a fraction of its constituents, which are magnetic dipoles.

3.3 Geometric Frustration

The important property of *frustration* consists in the impossibility of a system to satisfy and minimize all its energies and interactions between pairs simultaneously. Such impossibility may arise due to an intrinsic structural disorder of the system, as in spin glasses [3], or also due to its geometry, as occurs in spin ices [45]. In this work we will only address the second case, the so-called *geometric frustration*.

A simple way to exemplify it is using spins from the Ising model subject to antiferromagnetic interactions, favoring the anti-alignment of neighboring spins [46]. In this example, they are arranged in two different lattice geometries: one square and the other triangular, as shown in Fig. 8. In the square lattice, the interaction can be fully satisfied for all pairs of neighboring spins. In other words, it is possible to organize the lattice spins so that they all interact antiferromagnetically, simultaneously, with their nearest neighbors, minimizing the energy of the system. However, the same does not happen in the triangular lattice: regardless of the orientation of the spins allocated to each vertex, there will always be a frustrated interaction in which the spins will be aligned parallel to each other. Thus, if two spins of the triangular lattice are antiferromagnetically aligned, the third will necessarily be interacting ferromagnetically with one of them, and the interactions cannot be minimized simultaneously. In this case, antiferromagnetic interactions are incompatible with the triangular geometry.

Here, it is already possible to see that frustration is closely related to degeneracy: the spins arranged in the square lattice can be organized so that we have two degenerate states, while in the triangular lattice there is the possibility of six degenerate states, as seen in Fig. 8. In fact, geometrically frustrated systems have this property as being responsible for degenerate ground states, which are generally not related by any symmetry

[3] Spin glass refers to a system whose low-temperature state is marked by disordering and freezing of spins. In this aspect, it is characterized by exhibiting frustration due to competition among different interactions, not favoring any specific configuration of magnetic moments, and the interactions must be at least partially random. The term *glass* is due to an analogy with an ordinary glass, due to its amorphous and non-regular structure [44].

operation, instead of just having one stable configuration as the ground state [46].

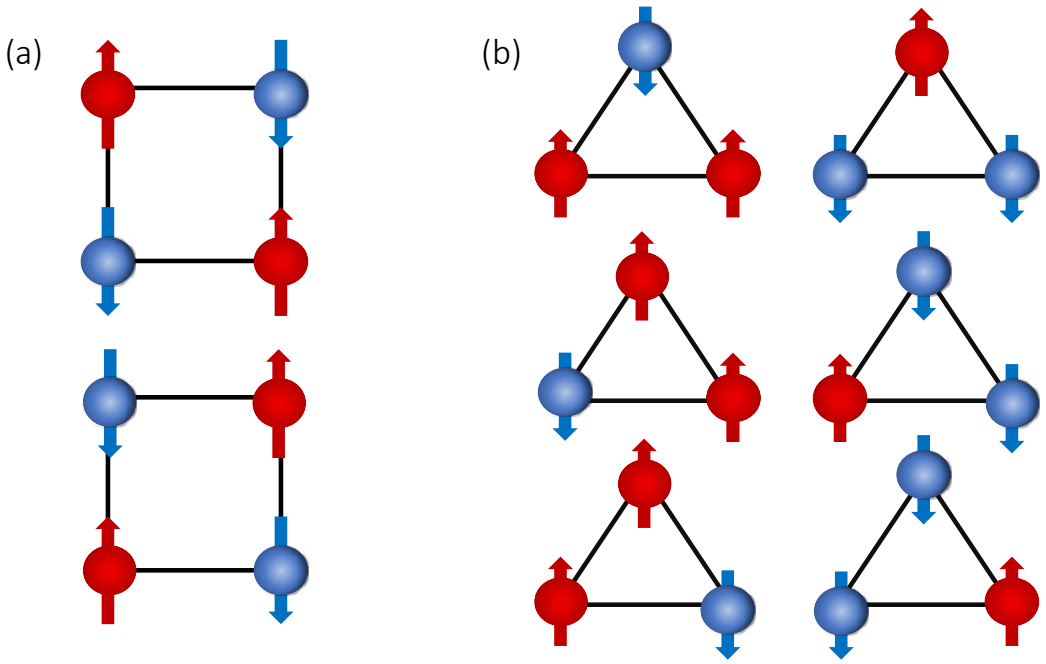

Figure 8: Square and triangular lattices with Ising spins interacting antiferromagnetically. While a square lattice has only two degenerate ground states, the triangular lattice has six due to geometric frustration.

4 Spin Ices

4.1 Natural Spin Ices

Spin ices are geometrically frustrated magnetic materials that exhibit collective excitations behaving like emergent magnetic monopoles. They receive this name due to some similarities with water ice, and therefore it is worth explaining these common characteristics to better understand these systems.

In the tetrahedral crystal structure of water ice (Fig. 9**(a)**), an oxygen ion O^{-2} located at the center of a tetrahedron connects to the four nearest O^{-2} ions located at the vertices of this tetrahedron. Between each pair of oxygen ions, there is a hydrogen ion H^{+}, or simply a proton. However, contrary to what one might assume, the lowest energy configuration for the H^{+} ions is not at the midpoints between the O^{-2} ions. In fact, the proton comes closer to one of the O^{-2} than the other. So, when analyzing the four $O-O$ segments referring to the bonds between the central O^{-2} and those at the vertices, it is clear that two H^{+} ions are close to the central O^{-2}, while the other two H^{+} ions are further away.

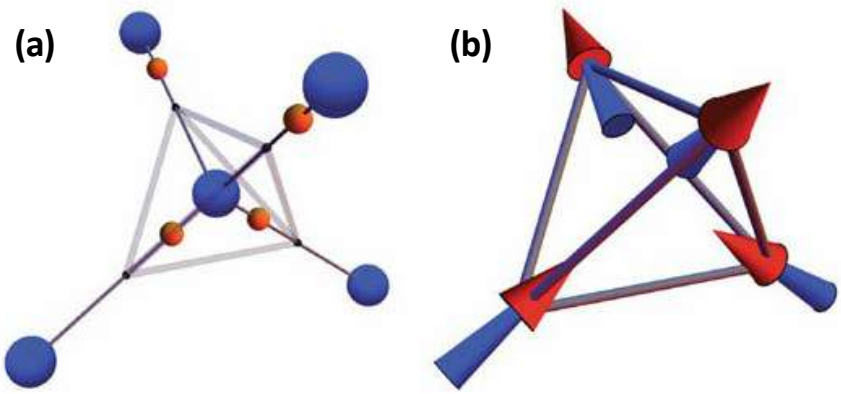

Figure 9: **(a)** Schematic illustration of the tetrahedral crystal structure of water ice, in which the larger spheres in blue represent the O^{-2} ions, and the smaller spheres in orange represent the H^{+} ions. It is possible to see that two H^{+} ions are close and covalently linked to the central O^{-2}, and two are further away from this O^{-2}, but close to two of the four neighboring oxygen ions. **(b)** Illustration of the tetrahedral structure of spin ice, in which the arrows represent the magnetic moments. Two point toward the center of the tetrahedron, while two point outward, obeying the ice rule. Figures taken from Ref. [4].

This configuration was first described in 1933 by the British physicists John Bernal and Ralph Fowler, derived from spectral and X-ray data [47]. To explain the position of hydrogen and oxygen ions in water ice, they created the so-called *ice rule* or *two-in-two-out rule*, which was in accordance with the knowledge that separation between the oxygen ions in the lattice was approximately 2.75 Å, and that the separation between the O^{-2} and H^{+} ions was approximately 0.96 Å, which implied the non-centered position of the proton between an $O-O$ connection [47]. Still in 1933, William Giauque and Muriel Ashley [48] indicated the possibility of a non-zero residual entropy in water ice in the limit of low temperatures, i.e., $T \to 0$, due to the large number of ways in which the system can organize itself into different microstates without changing its macroscopic properties even at temperatures close to 0K.

Based on these works, two years later Linus Pauling developed a theory [49] capable of explaining and calculating this residual entropy considering the ice rule: between each bond of the type $O-O$ there must be a proton, and this proton can assume two possible positions, with the restriction that there must always be two H^{+} closest and two H^{+} furthest from each O^{-2} ion. From this, Pauling was able to estimate in his calculations that the residual entropy value for water ice would be 0.81 cal K^{-1} mol^{-1} [50]. In 1936, W. F. Giauque and J. W. Stout verified this prediction experimentally [51], obtaining the value of 0.82 ± 0.05 cal K^{-1} mol^{-1}, exactly as predicted by Pauling (within error).

Similar to what occurs with water ice, spin ices are found in nature in the form of crystalline structures that have a pyrochlore-type lattice, which consists of tetrahedra connected by their vertices, as can be seen in Fig. 10. They are composed by rare-earth insulating oxides, and the most common ones studied in the literature are holmium titanate ($Ho_2Ti_2O_7$), holmium stannate ($Ho_2Sn_2O_7$) and dysprosium titanate ($Dy_2Ti_2O_7$) [52–54]. In general, these crystals are of the form $T_2A_2O_7$, where the ion T^{+3} is a rare-earth magnetic element and the A^{+4} is a non-magnetic ion. Due to the presence of rare-earth magnetic elements such as dysprosium (Dy) and holmium (Ho) in these materials, the electronic distribution of Dy^{+3} and Ho^{+3} ions makes the exchange interaction weak. Furthermore, these materials have a very low Curie temperature, on the order of a few Kelvin. Added to these factors, the dipolar interaction is favored due to magnetic moments of the order of $10\mu_B$ and lattice spacing of a few Angströns. In other words, dipolar interactions are more significant than exchange interactions in natural spin ices, and these systems must be described by a model that includes the exchange interaction

for first-neighbor pairs and the long-range dipolar interaction between all moments, as in Eq. 2.7.

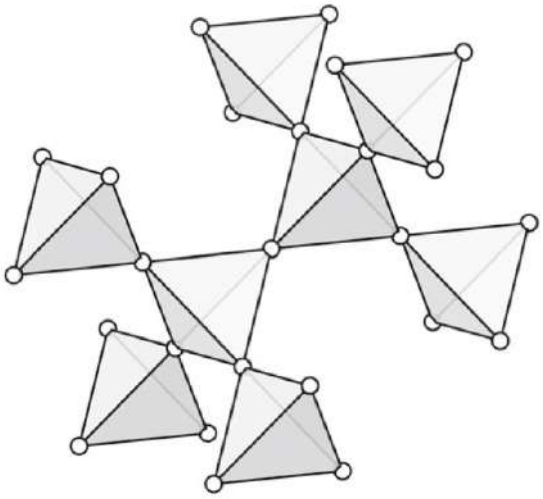

Figure 10: Illustration of a projection of a part of the pyrochlore lattice. Figure taken from Ref. [5].

In addition to the pyrochlore-type lattice, another extremely important similarity with water ices is the fact that the configuration that minimizes the energy of natural spin ices is also of the *two-in two-out* type, with two moments (or spins) pointing to the center of the tetrahedron and two spins pointing outward, as seen in Fig. 9**(b)**. At temperatures below hundreds of Kelvin for these crystals, the magnetic moments present at the vertices of the tetrahedral structure align parallel to the line that connects the centers of two consecutive tetrahedra due to the anisotropy of the crystal, i.e., there is a directional tendency for the moments due to the crystalline arrangement itself. Consequently, these moments behave like Ising spins.

Furthermore, in both cases there is geometric frustration. In water ice, there are six different possibilities of rearranging the protons between the O^{-2} ions in the system, maintaining the restriction of two H^{+} being closer and two being further away from an O^{-2} ion. In spin ices, there are also six possible different configurations that obey the ice rule (Fig. 11), that is, six configurations that minimize the energy of the system and correspond to the ground state, among sixteen possible configurations. This makes the residual entropy at $T \to 0$ of both systems equal. Moreover, since the ice rule can be satisfied by different configurations, the ground state is degenerate.

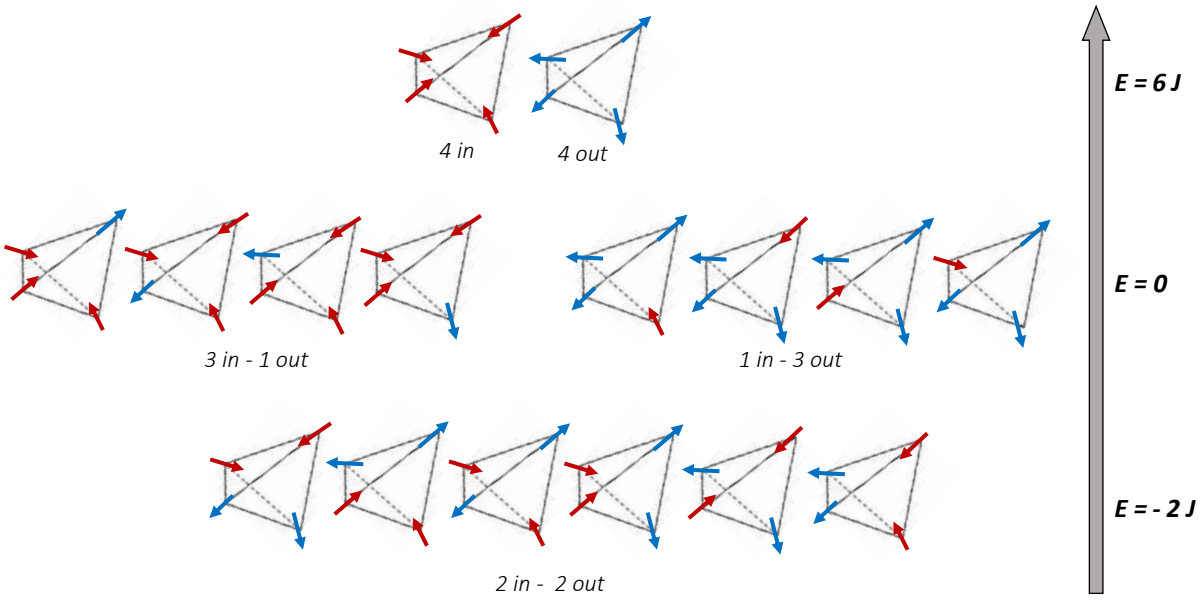

Figure 11: Representation of the 16 possible moment configurations at the vertices of a tetrahedron. The red arrows represent moments pointing towards the center of the tetrahedron, and the blue ones pointing outwards. The energies indicated on the right were accounted for exchange interactions between ferromagnetically interacting spins [6]. Figure adapted from Ref. [6].

As a consequence of the dipolar interaction being dominant in spin ices, the effective interaction between first neighbors has to be ferromagnetic. Otherwise, for the first neighbors interacting antiferromagnetically the system would not be frustrated. If this occurred, the 4 in and 4 out configurations would no longer be the ones with the highest energy, but rather the ones with the lowest energy, and there would be no geometric frustration. As a result, the fundamental state of the system would not be degenerate and there would be no residual entropy [6].

4.2 The Dumbbell Model

In a work of extreme importance for advances in the area of research on spin ices, Castelnovo and his collaborators [7] proposed a model in which a magnetic dipole moment was treated as a pair of opposite and rigid charges, analogous to a dumbbell, and the two possibilities of assigning charges to the dumbbell represent the two possible orientations of the original dipole moment. These charges are determined quantitatively through the relationship $q = \pm m/d$, with d being the distance between neighboring magnetic ions, corresponding to the size of the dipole, and m being the magnitude of the magnetic moment. Using this model, the authors showed that excitations of the type $3in - 1out$

or $1in - 3out$, represented in Figure 11, can be considered a violation of the ice rule, behaving in a manner analogous to an emerging magnetic monopole.

The representation of magnetic moments or spins in the dumbbell model is illustrated in Fig. 12, with two neighboring tetrahedra connected at their vertices. The total charge at the center of each tetrahedron α is given by $Q_\alpha = \sum_{i\in\alpha} q_i$. In Fig. 12**(a)**, it is possible to observe the spins obeying the ice rule, with two pointing towards the center and two pointing outside the tetrahedron. In **(c)** we have the same case, but using the dumbbell model. Here, we could interpret that two north poles and two south poles meet in the center of the tetrahedron, resulting in a zero residual charge in this location, i.e., $Q_\alpha = 0$. Subjecting this lattice to some excitation, for example, to an external magnetic field strong enough to reverse the magnetization of a dipole (in letter **(b)**, we can observe a change in the direction of the spin located at the common vertex), we obtain an excited state. This causes a neighboring monopole-antimonopole pair to be formed at the centers of the two adjacent tetrahedra, easily visualized with the dumbbell model in **(d)**, with net magnetic charge $Q_\alpha = \pm 2m/d$ on each of them. Therefore, the centers of the tetrahedra become generators or sinks of magnetic flux, that is, there is a creation of 'magnetic monopoles' due to a non-zero residual magnetic charge, which can be described as violations of the ice rule.

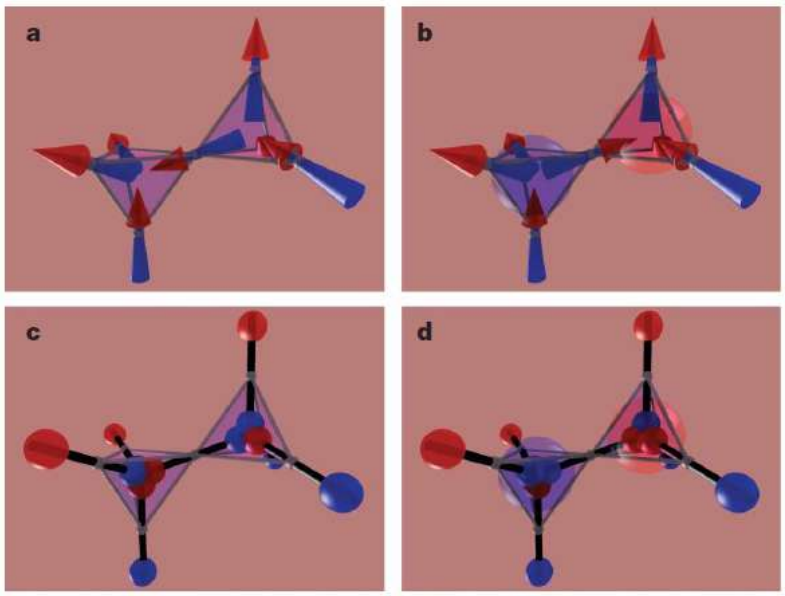

Figure 12: Illustration of two tetrahedra in a natural spin ice lattice **(a)** obeying the ice rule; **(b)** violating the ice rule with the creation of the monopole-antimonopole pair due to the spin inversion between the two tetrahedra. Letters **(c)** and **(d)** illustrate the cases in **(a)** and **(b)**, respectively, but using the representation of the dumbbell model. Figure taken from Ref. [7].

It is possible to increasingly distance a monopole from its antimonopole through successive inversions of adjacent spins, giving the monopoles freedom to move in the lattice. In Fig. 13, we can see the blue and red spheres, representing the monopole-antimonopole pair, far from each other. However, both are connected by a string represented by the color white. This string is formed by the chain of inverted spins in the process of pair separation, and locally has the restoring function of the ice rule. It is called *Dirac string* due to its non-energetic character, similar to what occurs in the model proposed by Paul Dirac for magnetic monopoles [55]. However, in the Dirac model this string could not be observable, and in spin ices it is.

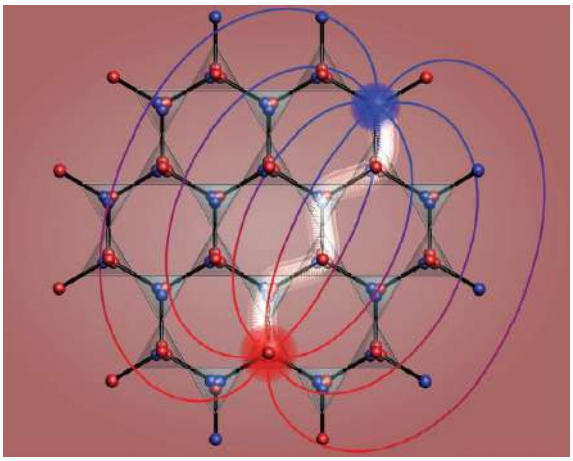

Figure 13: Dirac string, in white, connecting the monopole-antimonopole pair. Figure taken from Ref. [7].

4.3 Artificial Spin Ices

As the name suggests, *artificial spin ices* (ASIs) are structures produced in the laboratory, with the aim of imitating their natural analogues. The first experimental realization of these systems occurred due to advances in lithography techniques,with the work of Wang and his collaborators [8] in 2006. They proposed building two-dimensional lattices of ferromagnetic nanoislands arranged in a square geometry configuration so that they presented geometric frustration (Fig. 14). These materials were called *artificial spin ices* (ASIs) and are usually nanofabricated using electron-beam lithography (EBL), a process that will be described in more detail in the next chapter.

Nanoislands (or nanomagnets) are generally made of permalloy, a metallic alloy composed of 70% to 90% of nickel (Ni) and the remainder of iron (Fe), with effectively zero crystalline anisotropy. Because of this, the magnetic moments align along the longest

length of the nanomagnet due to shape anisotropy[1], causing the nanoislands to behave as a magnetic monodomain, which can be interpreted as an Ising-type macrospin. Furthermore, they usually have dimensions around 80 nm × 200 nm × 30 nm, so that in general each nanoisland has a volume of $V = 4.8$ x 10^5 nm^3. Since the saturation magnetization of permalloy is equal to $M = 8.6$ x 10^5 A m^{-1}, the magnetic moment per nanomagnet is $m = MV = 4.1$ x 10^{-16} A m^2, so that $m \simeq 10^7 \mu_B$, a value considered very high. Using it to calculate the temperature regime under which the ASIs are influenced by thermal excitations obtained through the dipolar interaction energy and the Boltzmann energy term ($E = k_B T$), it is obtained that only temperatures higher than 10^4 K could induce the inversion of the nanomagnet magnetization. Therefore, we can consider these systems as being athermal, making it possible to study them at room temperature without any modification of their magnetic properties due to thermal fluctuations, which even allows the probing of the system's magnetic moments by magnetic force microscopy (MFM).

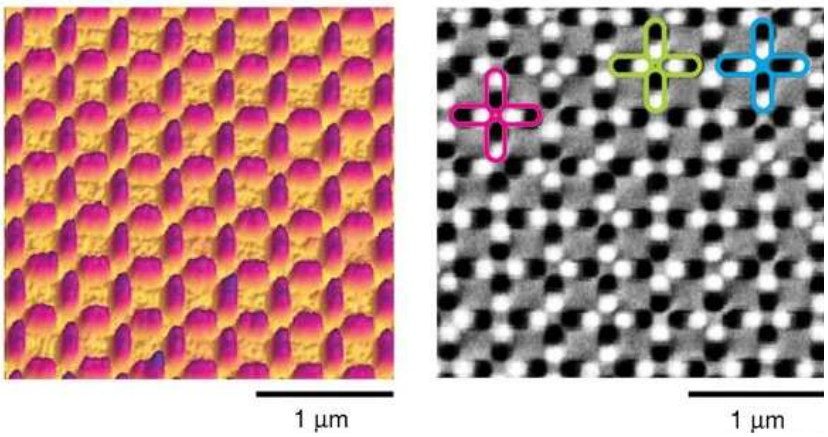

Figure 14: On the left, an atomic force microscopy (AFM) image of the artificial spin ice square lattice experimentally produced by Wang and his collaborators [8]. On the right, an MFM image obtained from the same array. The black and white dots represent the north and south poles of the nanoislands, reflecting their magnetic monodomain character. The contours colored in pink, blue and green indicate examples of vertices T_1, T_2 and T_3, respectively, which will be explained below. Figure taken from Ref. [8].

Due to the dimensions of the nanomagnets, whose length is on the order of hundreds of nanometers with ends separated by tens of nanometers, the dipolar interaction is sufficient to describe the system, as the exchange interaction is only significant for

[1] Shape anisotropy is associated with the influence of the system shape on its physical properties. In the case of magnetic systems such as ASIs, composed of nanomagnets with an elongated geometry and a generally cylindrical shape, the magnetic moments tend to align along the longest axis, also called the easy axis.

distances of just a few Angströns. Therefore, in theoretical models each nanoisland is considered to be an ideal dipole, with dipolar interaction between them.

In addition to ASIs reproducing the main characteristics of their natural analogues, they offer several advantages. Not only the emergence of magnetic monopoles can be observed in ASIs, but they are also highly reproducible in the laboratory and possess extremely small dimensions, facilitating their application in devices. Furthermore, it is possible to control, create, and explore different geometries depending on the arrangement of the nanoislands in the lattice (Fig. 15). This capability enhances the investigation and visualization of exotic behaviors arising from the geometric frustration of the structures.

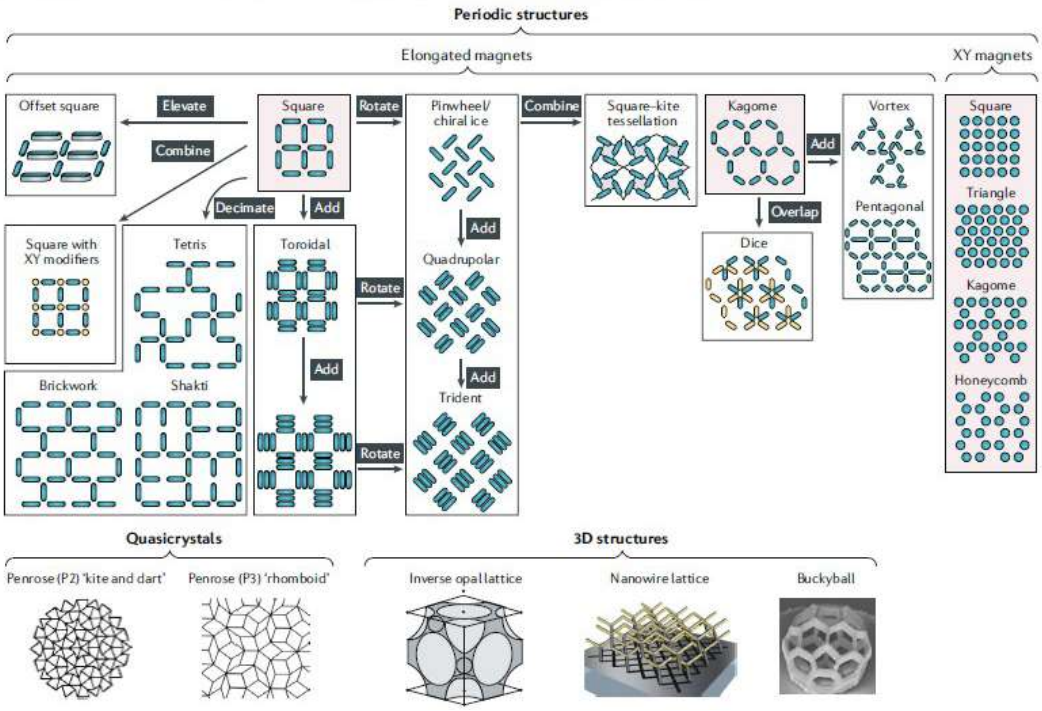

Figure 15: Example of possible ASIs lattices. Figure taken from Ref. [9].

4.3.1 Unconnected Square Lattices

Despite the freedom to create various types of lattices, square geometry lattices are prominently featured in the literature because they are considered the closest analog to natural spin ices. Like their natural counterparts, they also have four spins per interaction vertex, resulting in sixteen possible configurations for each vertex, as can be seen in Fig. 16. However, there are some important differences between them. While in natural counterparts there are six configurations obeying the ice rule, all of them with the same minimum energy and fitting into the same topology, in the square geometry of ASIs there

are two topologies with different energies obeying the ice rule, called T_1 and T_2 (or *type I* and *type II*, respectively). For unconnected nanoislands, like those developed by Wang and his collaborators [8], the lowest energy state is the one in which they are in the T_1 configuration. Topologies T_3 and T_4 (or *type III* and *type IV*, respectively) are violations of the ice rule and the emergence of a non-zero residual magnetic charge, unlike T_1 and T_2 with zero residual charge. Because of this, they represent magnetic monopoles in the lattice.

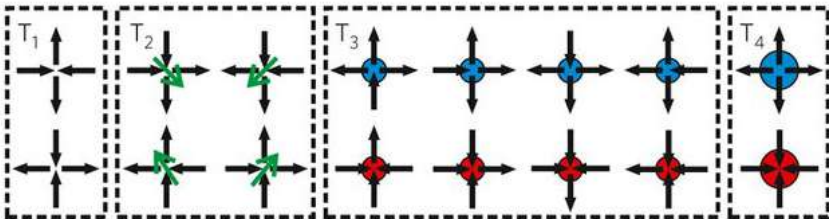

Figure 16: The sixteen possibilities for spin configuration in an ASI vertex of a two-dimensional square lattice. The topologies are energetically ordered, with T_1 the least energetic and T_4 the most. Figure taken from Ref. [10].

Therefore, a square ASI lattice with unconnected nanomagnets does not present a degenerate ground state as occurs in natural ones, as the two topologies obeying the ice rule have different energies, unlike the case of a tetrahedron in natural three-dimensional spin ice. This lack of degeneracy prevents the magnetic monopoles from moving freely in the square arrangement, causing them to be considered as *Nambu* type rather than *Dirac* type. The main difference between them is that while Dirac monopoles are connected by a non-energetic string, Nambu monopoles are confined by an energetic string, which restricts their freedom of movement in the lattice. According to Nambu, in addition to being energetic, this string is oriented, which is exactly what happens in ASIs with a square lattice considering that the energy depends on the shape of the string.

The first theoretical modeling of this behavior was conducted by Mól and his collaborators [56] using the *simulated annealing* method, which involves raising the temperature of the system to the Curie Temperature, and then gradually reducing it until the minimum energy configuration is found. The analysis also considered the dipolar interaction between the nanomagnetic islands, and correctly reproduced the experimentally observed ground state [10].

The model proposes that the total energetic cost to separate a pair of charges involves a Coulomb potential and a linear confining potential, the latter related to an excitation similar to an energetic string that connects the monopole-antimonopole pair.

Thus, the most general expression for the total cost of a pair of magnetic monopoles separated by a distance R could be expressed in a potential given by Eq. 4.1:

$$V(R) = \frac{q}{R} + bX(R) + c \tag{4.1}$$

Where q/R is the Coulombic-type term, $q < 0$ is a constant defined as being the product of charges of the monopole-antimonopole pair, $X(R)$ is the length of the string connecting the monopoles, $b > 0$ is a constant related with the effective string tension, and c is a term associated with the energy required to create magnetic charges. Note that the size of the string X is different from the distance R between the monopole-antimonopole pair, as can be seen in Fig. 17, even though there is a proportional relationship between these values.

The $bX(R)$ term is explained due to the linear increase in energy to separate a monopole from its antimonopole as these magnetic charges separate with the reversal of the chain of magnetic moments. In this process, the string appears due to a change in topology in the region between the charges, going from T_1 to T_2. As T_2 is more energetic than T_1, even obeying the ice rule, there is a clear energetic cost associated with moving these charges away from each other. In Fig. 18, it is possible to better visualize the process of creating a monopole-antimonopole pair and its separation due to spin inversion, forming various T_2 topologies along the path.

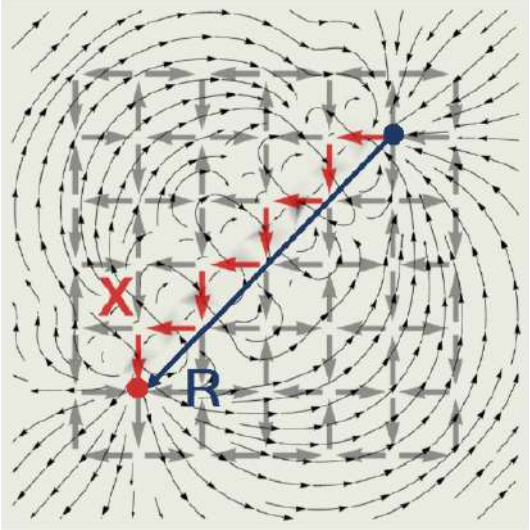

Figure 17: Difference between X (string length represented in red) and R (distance between the monopole-antimonopole pair represented by the blue line) in a square lattice with two. Figure taken from Ref. [11].

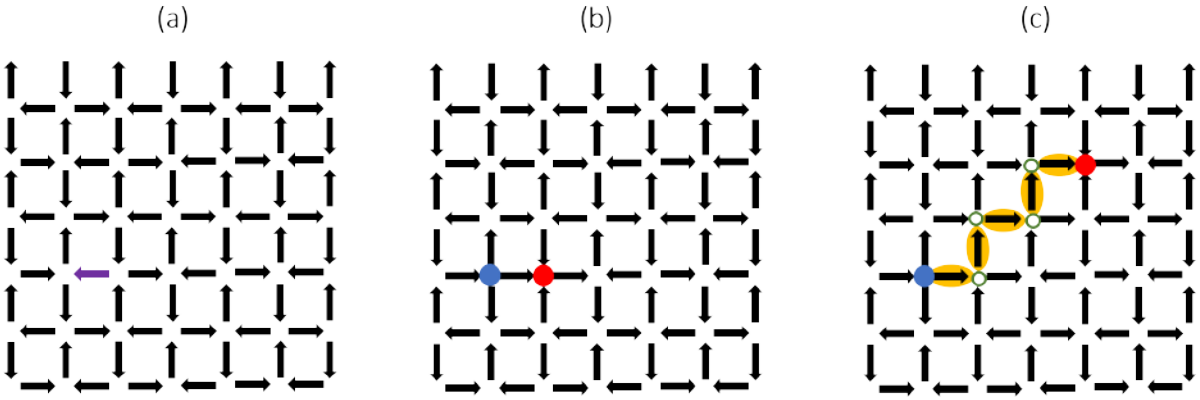

Figure 18: **(a)** Representation of the ground state formed by T_1 topologies. The purple arrow represents the magnetization of the nanoisland that will reverse. **(b)** Formation of the T_3 topologies, or simply the monopole-antimonopole pair, represented by the blue and red circles. **(c)** Formation of the energetic string, whose length corresponds to that of the nanoislands highlighted in orange. These had their magnetic moments reversed, allowing the magnetic charges to move away. The green circles corresponds to the T_2 topologies.

In an effort to reduce the energetic string in ASIs, some studies have proposed methods to equalize the energy between T_1 and T_2 vertices, thereby making the ground state degenerate and deconfining the monopole pairs, providing them with greater freedom in lattices. One of the ways to do this while maintaining the quadrilateral geometry was also proposed by Mól and his collaborators [57], introducing a displacement of height h between the dipoles (or nanoislands). The idea was that if h was chosen so that the energies of all vertices that obey the ice rule would become degenerate. It was observed that for h varying between 0 and $0.444a$: the linear confining term present in the energy equation of monopole-antimonopole pairs decreased rapidly as h increased up to $0.444a$, although it did not disappear completely. Here, a is the lattice spacing, or simply the distance between the nanomagnets. Above $h = 0.444a$, the ground state changes its configuration from an ordered antiferromagnetic arrangement to a ferromagnetic one. However, this system is three-dimensional and considerably more difficult to implement experimentally, in addition to having restricted applications due to its dimensions. Another alternative involves modifying the lattice by making it rectangular, as will be explained in the following section.

4.3.2 Unconnected Rectangular Lattices

As previously noted, ASIs with a square lattice have a non-degenerate ground state because the two topologies that obey the ice rule have different energies. The main reason for this difference in energy is the lack of equivalence in the distances of the six possible bonds between the four magnetic dipoles forming a vertex, as depicted in Fig. 19**(a)**. As a result, the monopoles formed are always connected by an energetic string and cannot move freely in the lattice as in natural spin ices.

To minimize this problem in ASIs, Nascimento *et al.* [27] proposed, based on their theoretical studies, an intentional change in the horizontal and vertical lattice spacings, so that they become rectangular. In this geometry, each site in the lattice is characterized by parameters a and b, as demonstrated in Fig. 20. Here, we will define the parameter $\gamma = a/b$, which will always be used in this work to define the ratio between a and b. In the work of Nascimento *et al.*, arrangements with different ratios γ were studied, and it was theoretically concluded that for $\gamma = a/b = \sqrt{3}$, the ground state becomes degenerate. With this, the magnetic charges become free to move in the lattice. For this specific value of γ, the energy degeneracy is related to the fact that the distance between all dipoles is equal, as demonstrated in Fig. 19**(b)**. In their computational simulations, the nanoislands were treated as an ideal dipole interacting only by dipolar interaction, a good approximation considering that the length of the exchange interaction is smaller than the separation distance between the nanoislands.

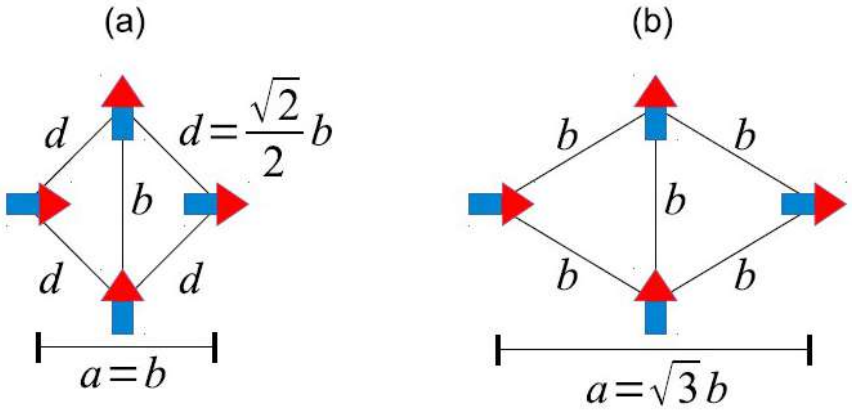

Figure 19: **(a)** For the square lattice, the distance b between two adjacent spins pointing along the same direction is greater than the distance $\sqrt{2}b/2$ between the two adjacent spins pointing in the perpendicular direction. **(b)** For $a = \sqrt{3}b$, these distances become equal. Figure taken from Ref. [6].

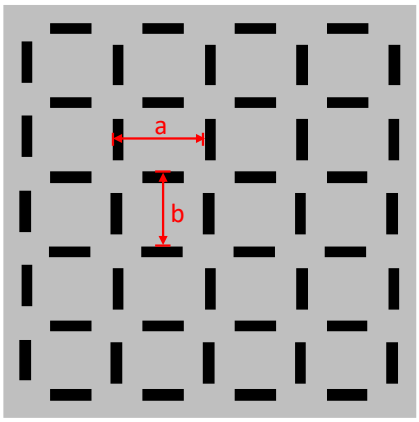

Figure 20: Rectangular geometry of an ASI lattice. The parameter a corresponds to the horizontal distance between the nanomagnets, and parameter b corresponds to the vertical distance between them.

Experimental studies carried out by Ribeiro *et al.* [28] also showed a strong indication that in samples with $\gamma = \sqrt{3}$, there would be deconfinement of magnetic charges. In this work, the researchers investigated samples with $\gamma = \sqrt{2}$, $\gamma =$ $sqrt3$ and $\gamma = \sqrt{4}$. The samples were demagnetized and probed by MFM, and it was noticed that for $\gamma = \sqrt{3}$, the topologies corresponding to the excitations above the ground state, giving rise monopole-antimonopole pairs, appeared in greater numerical density compared to the other values of γ. Such observations were carried out at room temperature and indicated that, in fact, the number of monopoles in the lattice was a consequence of a purely geometric factor, so that they could be generated spontaneously in lattice whose $\gamma = \sqrt{3}$. As the total energy of a pair of magnetic charges depends on the energy of the string connecting them, this experiment is in accordance with the idea that the geometry of the lattice is associated with the decrease in the energy of the string $\gamma = 3$.

In the case of rectangular geometries, there are also sixteen possible configurations for the magnetic moments at the vertices, but with five different energy topologies, which can be seen in Fig. 21. In addition to the T_1, T_2 and T_4 topologies, it is possible to see that the T_3 topology is divided into T_{3-1} and T_{3-2}. In this aspect, some important differences between square and rectangular lattices topologies should be highlighted: in the particular case of the square lattice ($\gamma = 1$), the energies of T_{3-1} and T_{3-2} are equal, and that is why they are grouped in the same topology. When the lattice becomes rectangular ($\gamma \neq 1$), topologies T_{3-1} and T_{3-2} have different energies and charges. For the case of $\gamma > 1$, that is, $a > b$,the vertices in the T_{3-2} topology have more residual charge than those in the T_{3-1} topology. Furthermore, for $\gamma \neq 1$, the vertices in the T_1 topology have a residual

charge even obeying the ice rule, but they do not have a residual magnetic moment (Fig. 22**(a)**). Those in the T_2 topology, also in rectangular lattices, have zero residual charge but effective residual magnetic moment (Fig. 22**(b)**). In lattices with $\gamma = 1$, these vertices did not have residual charges and moments.

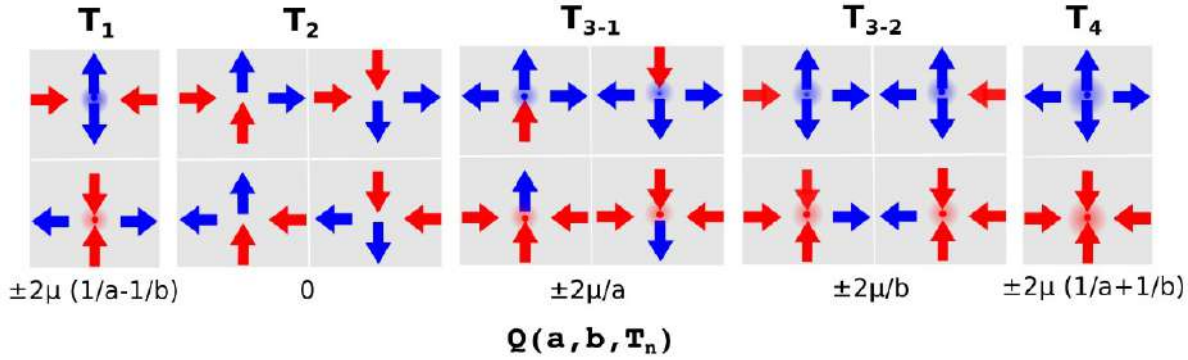

Figure 21: The 16 possible configurations for the magnetic moments at the vertices classified into five distinct topologies. Below, the residual magnetic charges of each of them are indicated. Figure taken from Ref. [6].

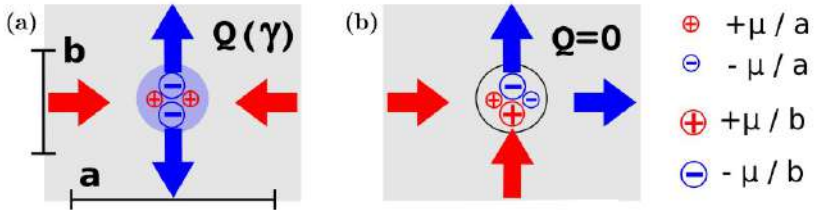

Figure 22: Representation of topologies **(a)**T_1, with non-zero residual charge due to the fractionalization of dipoles; and ((**(b)** T_2, without residual charge. Figure taken from Ref. [6].

The acquired characteristics of residual charge at the T_1 vertices and effective magnetic moment ('spin') at the T_2 vertices of rectangular lattices play a crucial role in obtaining a degenerate ground state. For a specific value of γ, it is possible to obtain a balance in the charge and spin values, causing the energies of T_1 and T_2 to be equal and the energy of the string connecting the monopoles to decrease. Nascimento and his collaborators [6, 27] showed analytically that the energies of the T_1 and T_2 topologies approach the same value when the nanoislands are arranged in a rectangular geometry with $\gamma \to \frac{1}{\sqrt{3}}$ and $\gamma \to \sqrt{3}$. This result is easily estimated by observing the graph in Fig. 23.

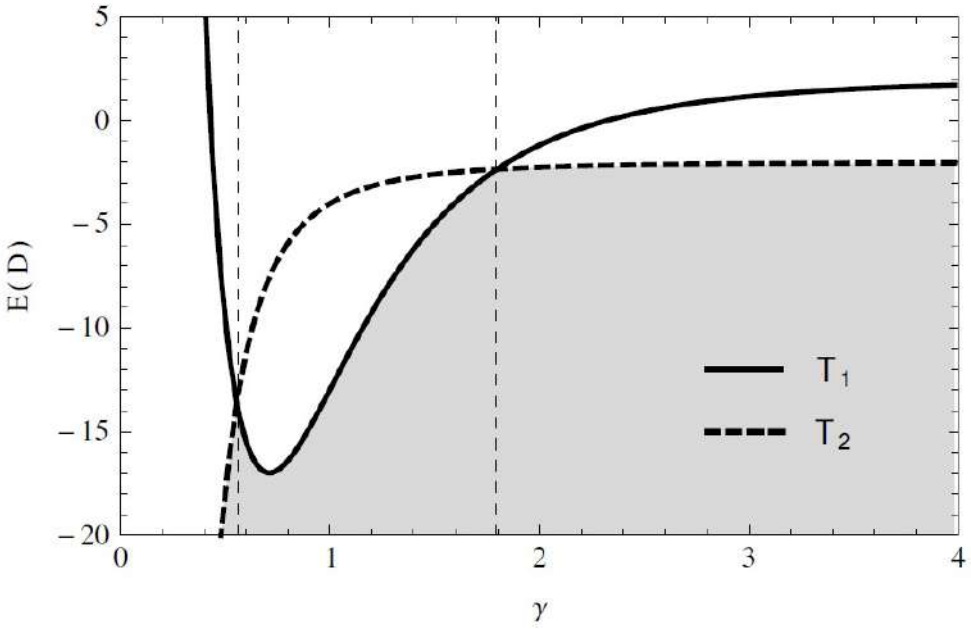

Figure 23: Total energy due to dipolar interaction for the 4 dipoles that make up a vertex of a rectangular lattice, configured in topologies T_1 and T_2 as a function of the parameter γ. Figure taken from Ref. [6].

Looking at the graph above, it is possible to notice that there are two equivalent ground state transitions in the rectangular lattice. For $\frac{1}{\sqrt{3}} < \gamma < \sqrt{3}$, the T_1 topology is the ground state, as occurs in the square lattice. However, as previously stated, in the rectangular lattice this topology is marked by the presence of non-zero residual charge at each vertex, as depicted in '*state-0*' in the Fig. 24. For $\gamma < \frac{1}{\sqrt{3}}$ or $\gamma > \sqrt{3}$, the ground state is characterized by all vertices in the T_2 topology, which is represented in Fig. 24 as '*state-1*'. Therefore, the ground state of the rectangular lattice is a state with residual charge at each vertex, but with zero net magnetization (T_1); or a state with residual magnetization at each vertex, but with zero net charge (T_2).

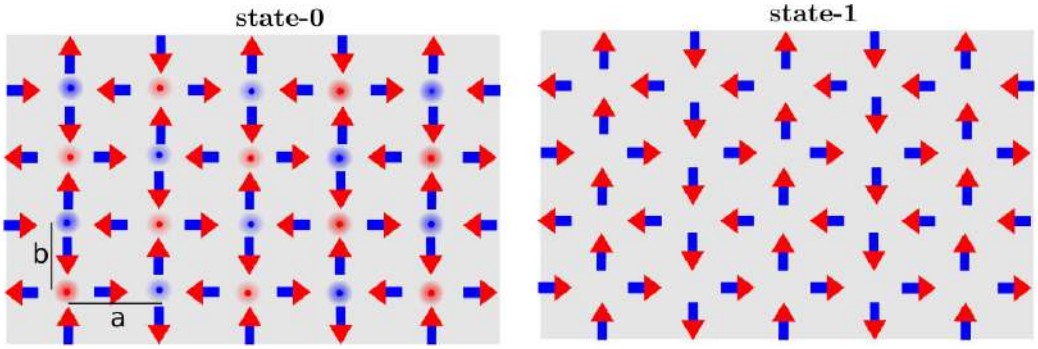

Figure 24: State-0 is the ground state of the square lattice and rectangular lattices with $\frac{1}{\sqrt{3}} < \gamma < \sqrt{3}$, formed by the T_1 topology. State-1 is the ground state of rectangular lattices with $\gamma < \frac{1}{\sqrt{3}}$ or $\gamma > \sqrt{3}$, constituted by the T_2 topology. Figure taken from Ref. [6].

4.3.3 Connected Square Lattice

As seen earlier, non-equivalent forces from the magnetostatic interaction between neighboring nanomagnets in a square lattice, whether they are orthogonal or collinear, cause the ground state of the system to be non-degenerate. However, some studies [12,13] have proposed that, for a two-dimensional square spin ice lattice, where the nanomagnets are physically connected at the vertices, such degeneracy is expected to be observed.

In this type of system, in addition to the dipolar interaction, the exchange interaction becomes relevant and plays a crucial role in the system's behavior. Due to the competition between these two interactions, different micromagnetic textures are formed at the vertices depending on how the magnetization is oriented locally. Through micromagnetic simulations, it is possible to estimate the energy associated with these different magnetization distributions, a value that also depends on the system's lattice parameters.

While in square lattices with unconnected nanomagnets the vertices with the lowest energy are those of type T_1, in general, for this same geometry but with the nanomagnets connected, the vertex with the lowest energy becomes type T_2. However, the energy difference between T_1 and T_2 for the connected square lattice can decrease considerably when the width and thickness of the nanoislands are chosen appropriately, and the states that obey the ice rule have very similar values [12].

It is worth noting that the vertices of connected and unconnected lattices are different, despite the same nomenclature. Using micromagnetic simulations performed on a single vertex made of four connected nanomagnets, it is seen that the magnetization distribution at the vertices resembles the magnetic domain walls, as can be seen in Fig. 25. Type I vertices have the shape of a magnetic antivortex, type II vertices are magnetized almost homogeneously in the same direction; type III have the shape of a transverse domain wall that separates the two horizontal nanomagnets; and type IV ones resemble a vortex domain wall with a counterclockwise chirality [12].

As the energy of the vertices depends on the geometry of the lattice, Perrin and his collaborators [12] investigated, using micromagnetic simulation, samples with different geometric parameters for the nanomagnets. Widths were varied from 50 to 400 nm, and thicknesses varied from 0.5 to 40 nm. The results obtained indicated that type II vertices, in fact, had lower energy than type I, unlike what occurs for unconnected nanomagnets. However, both asymptotically tend to the same energy in the limit of thick and/or wide

nanomagnets, as shown in Fig. 26. It is possible to see that, even in this limit, type II vertices still have lower energy. However, for thicknesses on the order of 30-40 nm and widths on the order of 200 nm or more, it is possible to estimate that sample defects, for example, will allow the system to select both types of vertices equivalently.

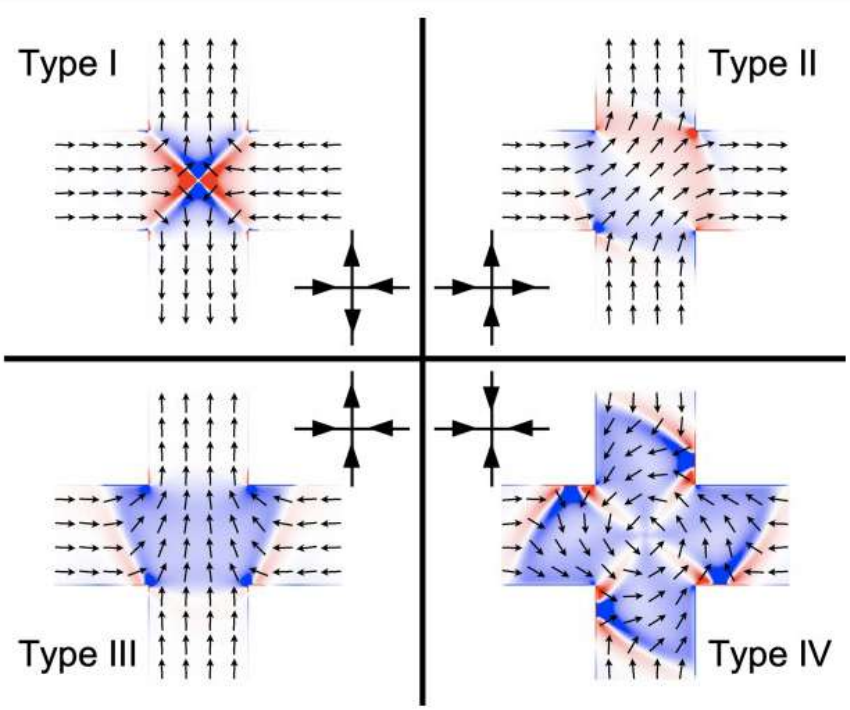

Figure 25: Micromagnetic configurations of type I, II, III, and IV vertices for 200-nm-wide, 20-nm-thick permalloy nanomagnets. Figure taken from Ref. [12].

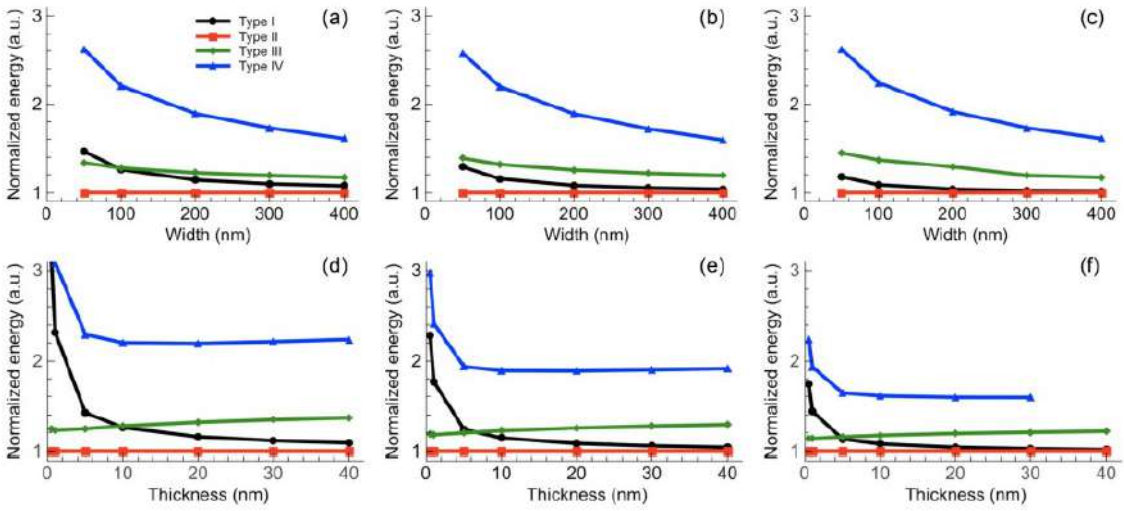

Figure 26: Normalized micromagnetic energy of the four vertex types as a function of the width and thickness of the nanomagnets. Nanomagnets are 10-, 20-, and 40-nm-thick in **(a)**–**(c)**, respectively, while they are 100-, 200-, and 400-nm-wide in **(d)**–**(f)**, respectively. Figure taken from Ref. [12].

To deeply understand the magnetic properties of spin ices, the magnetic structure factor (MSF) is a crucial measurement. This factor can be investigated directly through neutron diffraction experiments, which reveal the arrangement of the spins and the correlation between them. However, such experiments require sophisticated and expensive infrastructure, such as nuclear reactors or high-intensity neutron sources. These installations are rare and are concentrated in a few developed countries, such as the United States, France, United Kingdom, Japan, among others. In Brazil and many other countries, the lack of such resources significantly limits the carrying out of this type of experiment. Even in countries where these resources are available, access is competitive and costs are high.

An alternative to solving these limitations consists of carrying out micromagnetic simulations to estimate, predict and support experiments and theories on spin ice lattices. Using computational models that indicate the behavior of spins in these systems, it is possible to analyze the MSF without the need for large experimental installations. Simulations offer enormous flexibility, allowing exploration of a wide variety of experimental parameters, such as temperature, magnetic field, and spin interactions, without the physical constraints and high costs associated with neutron diffraction experiments.

Furthermore, the analysis of the MSF through simulations can provide detailed information about the ground state of the system. If it is ordered, so that the spins are organized in a periodic manner, the magnetic structure factor will present distinct and well-defined Bragg peaks, indicating a long-range correlation between the spins. On the other hand, if the ground state is disordered, the simulation results will show diffuse patterns in the magnetic structure factor, which reflect the absence of long-range correlation and a more random distribution of the spins.

In the work of Nascimento and his collaborators [13], micromagnetic simulations were carried out using the dumbbell model with the objective of obtaining the MSF to better understand issues involving the ground state energy of planar ASIs, considering both the size/length of the nanoisland and the geometry proportion of the rectangular lattice. Therefore, the simulations considered both the $\gamma = \frac{a}{b}$ parameter and the length ℓ of the nanomagnet. In them, the value of b of the rectangular lattices remained fixed, the value of a varied between $(b, 2b)$, and the length ℓ of the nanoisland varied between $(0, b)$. For $\ell = a = b$, the islands are physically connected. Furthermore, each of them had matrices of 20 x 20 vertices and 840 nanomagnets.

Considering the configuration **GS1** as the ground state populated only by vertices

of type T_1, and **GS2** as the ground state populated only by vertices of type T_2, the relative energy $\frac{E_{GS2}-E_{GS1}}{E_{GS2}}$ of a given arrangement as a function of γ and ℓ/b estimated by the dumbbell model can be seen in Fig. 27. Along the gray line, **GS1** and **GS2** have the same energy and are expected to fill the ground state equally. The **GS1** (**GS2**) state is energetically favorable below (above) such a line.

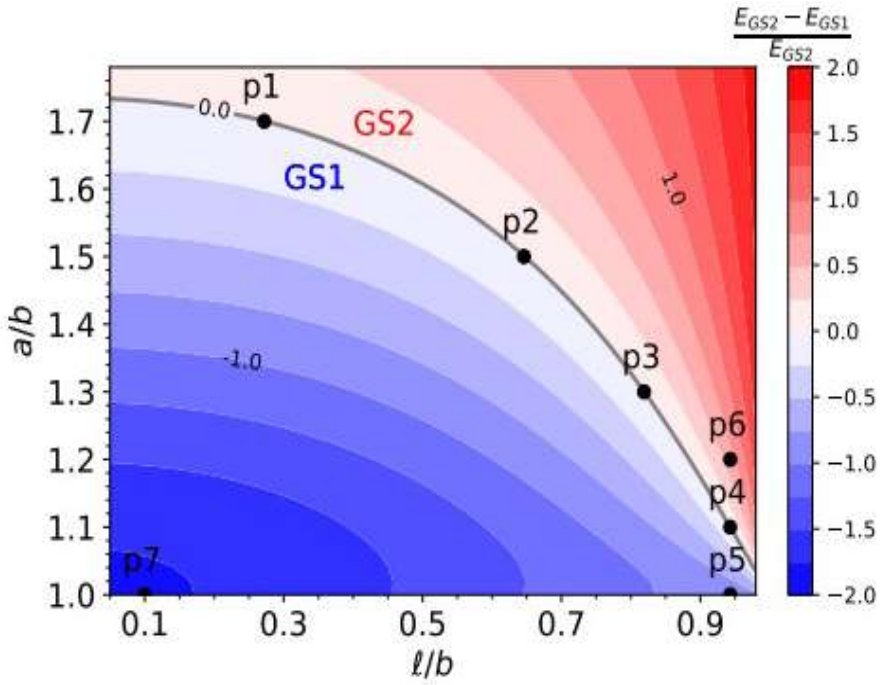

Figure 27: Phase diagram showing the favorable ground state depending on the ratios $\gamma = \frac{a}{b}$ and ℓ/b. The relative energy $\frac{E_{GS2}-E_{GS1}}{E_{GS2}}$ is represented in the $\gamma \times \ell/b$ plane. Along the critical curve (gray line), both configurations share the same energy. Above this curve, **GS2** is energetically favorable, while below, **GS1** becomes the ground state. Figure taken from Ref. [13].

In Fig. 28, it is possible to visualize the MSF patterns (on the left) and the **GS1** and **GS2** configurations (on the right), represented by points **p5** and **p6** in the graph of Fig. 27, respectively. At point **p5**, the ground state is ordered and primarily composed of T_1 vertices. The MSF pattern consists of distinct Bragg peaks at the corners of the Brillouin zone, which indeed indicate magnetic ordering. At point **p6**, however, the ground state is formed by T_2 vertices, and the MSF pattern exhibits broad lines and lacks Bragg peaks, suggesting a breakdown of long-range antiferromagnetic order in the system.

In Fig. 29**(a)**–**(d)**, it is possible to visualize how the MSF pattern and the spin configuration depend on γ and ℓ along the critical line. In panel **(a)**, we have the representation of point **p1**, which shows an MSF with broadly connected points, unlike the

sharp Bragg peaks observed in ordered systems seen in the previous figure. This suggests the occurrence of a degenerate ground state, where T_1 and T_2 (white and yellow regions, respectively) have the same energy. The number and distribution of these two types of vertices are comparable; statistically, the number of T_2 vertices (four possibilities) tends to be twice the number of T_1 vertices (two possibilities).

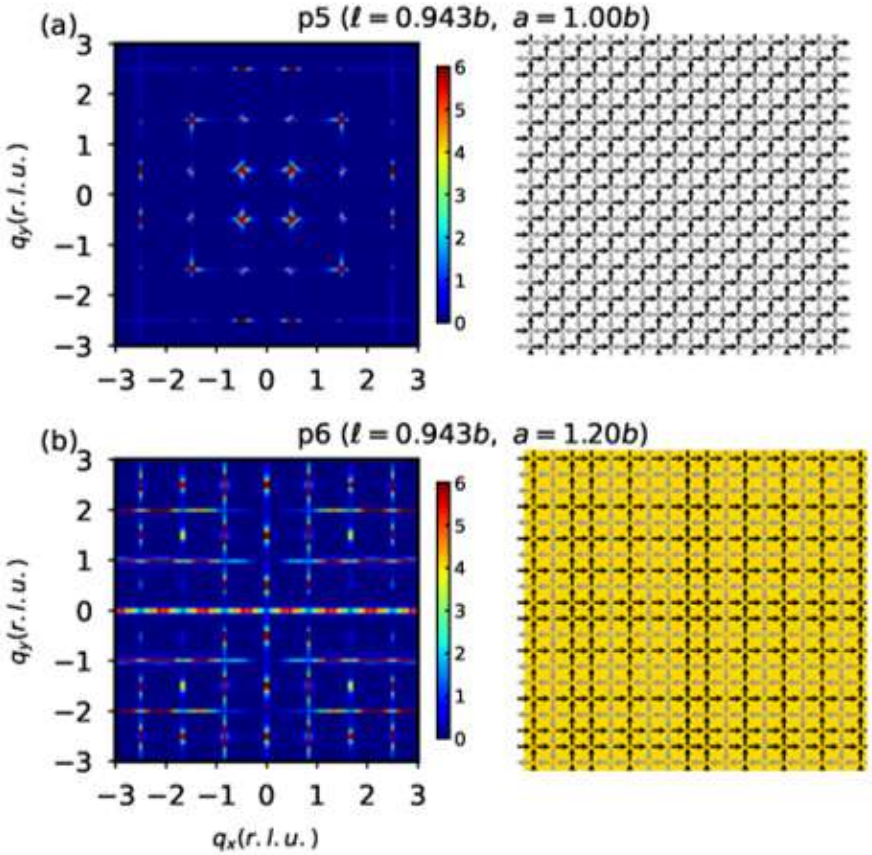

Figure 28: On the left, the average MSF of the low energy states of 100 samples simulated using the dumbbell model. On the right, a representative sample of the spin configuration. In **(a)**we have a point below the critical line, and in **(b)** a point above the critical line. Figure taken from Ref. [13].

As the value of ℓ increases along the critical line, the MSF indicates that the physical states become more densely populated. Although the number of types of vertices T_1 and T_2 is statistically equivalent for the situations shown in the figures, the distribution of these vertices changes, so that the ground state becomes more disordered as ℓ increases and the distribution of T_1 and T_2 becomes becomes more arbitrary across the lattice. This explains the fact that the discontinuity in the structure factor, which takes the shape of a butterfly, starts to become more evident for cases **p2**, **p3** and is even more pronounced for **p4**. From this last point onwards, pronounced narrowing points (the so-called *pinch*

points) are the main characteristic of the structure factor and are a signature of the degeneracy of the ground state, very similar to what occurs with natural spin ices.

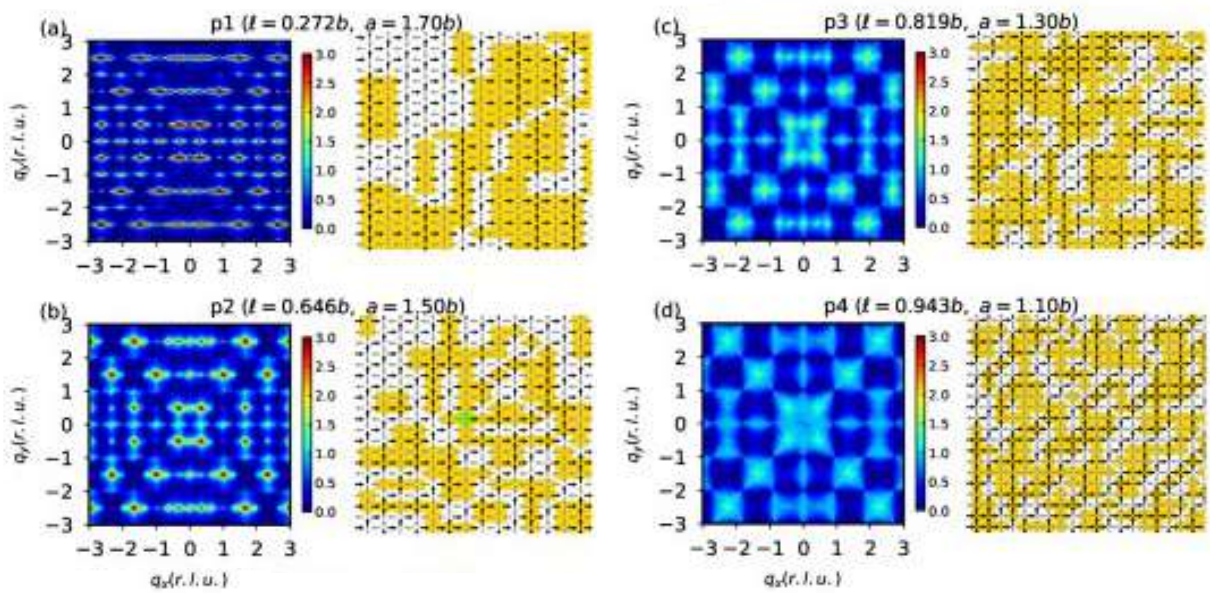

Figure 29: On the left, the average MSF of the low energy states of 100 samples simulated using the dumbbell model. On the right, a representative sample of the spin configuration. Here, four sets of parameters $(\ell/b, a/b)$ are taken along the critical line of the phase diagram (Fig. 27): **(a)** (0.272, 1.7), **(b)**(0.646, 1.5), **(c)** (0.819, 1.3), and **(d)** (0.943, 1.1). Figure taken from Ref. [13].

In the MSF calculated with the dumbbell model in [13], for very small nanoislands ($\ell << b$), the model captures degenerate ground states that are not entirely disordered. Although this is an excellent indication of ground state degeneracy and suggests the freedom of magnetic monopoles in two-dimensional rectangular lattices, this result is not fully compatible with the theoretical predictions mentioned earlier. This is because the spin configurations are divided into isolated domains of T_1 and T_2 vertices. However, for larger nanoislands, the results are more consistent with the literature. Extrapolating the graph in Fig. 27, it is possible to see that for connected square lattices with parameters $\ell \to b \to a$, the system's ground state is degenerate, as discussed in the work of Perrin et al [12].

5 Experimental Techniques

5.1 Electron-Beam Lithography

The nanofabrication process for ASI samples begins with electron-beam lithography (EBL). The word *lithography* comes from the combination of the Greek words *litho* and *graphy*, meaning *stone* and *writing*, respectively [58]. According to its etymology, it is possible to interpret it as referring to a method of printing on a rigid surface such as stone. In fact, lithography is a process used in micro and nanofabrication to pattern specific shapes on a thin film or substrate.

The most used types of lithography are optical and electronic, and the choice between them depends on the sample manufacturing volume, dimensions and desired resolution, with their systems integrated into an optical or electron microscope, respectively. In this work, the EBL system of the FEG-SEM (field emission gun – scanning electron microscope) equipment from the UFV Physics Department was used. As it is an electron microscope, this equipment offers high resolving power, allowing the visualization of materials on nanometric and even atomic scales (Fig. 30), in addition to an excellent depth of field, allowing greater focus and consequently greater image sharpness and contrast [14]. Therefore, it is a very versatile tool for micro and nanofabrication, since the same microscope used to produce the samples is also used to visualize the resulting structures.

The FEG-SEM equipment is very similar to the usual SEM, but it provides even higher resolution images and consequently much more detailed information on the sample surfaces. The operation of the SEM is based on projecting and sweeping a focused flow of electrons over surfaces, and thus collecting the different signals produced resulting from the interaction of electrons with the atoms that form the sample. Signals are collected through detectors, and the two most common types used to obtain high-resolution images in a SEM are the secondary electron detector (SED) and the backscattered electron detector (BSD). The images obtained from the surface are viewed in real time on a monitor using software that correlates the position of the beam with the intensity of the electrons acquired by the detector(s). BSD detects elastically dispersed electrons that have higher energy and originate below the surface of the sample. SED allows the visualization of ine-

lastically scattered electrons generated close to the sample surface, providing topographic information with the best possible resolution. Therefore, the resolution of a BSD image is worse than that of an image acquired with an SED [14, 59, 60].

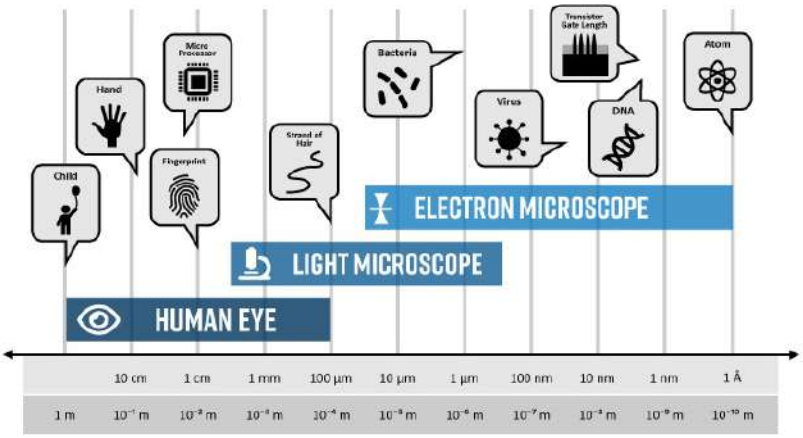

Figure 30: Comparing length scales accessible by different types of microscopes. Figure taken from Ref. [14].

Basically, the SEM is composed of an electron source (gun), electromagnetic lenses to manipulate the beam, detectors, sample stage, computer and display to view the images, as well as external vacuum pump(s). In general, the most common electron source (or electron gun) due to its low cost consists of a tungsten filament that is resistively heated to produce electrons (thermionic effect), which are then accelerated by a potential difference. In the case of FEG-SEM, the electron source consists of a tungsten wire with a very sharp tip, less than 100 nm, and an electric field is applied to this tip to extract the electrons. Then, a second field is used to accelerate them to the sample. This considerably increases the density, brightness, coherence and focus of the beam, providing very high resolution [14, 59, 60].

An interesting feature of the SEM is that, along with it, it is possible to use the energy dispersion spectroscopy (EDS) technique, which is very useful for knowing the chemical elements present at a microscopic level in a sample. This technique uses the characteristic X-rays emitted by the sample during SEM imaging in a fast, precise and non-destructive way, in order to identify its elemental composition. This is because the electron beam displaces an electron from the inner layer of an atom, and it is replaced by another from the outer layer. In this process, X-rays are emitted with specific energies, as each chemical element has a characteristic energy difference between the outer and inner electronic layers. Thus, the energies of the detected X-rays are directly related to the

elements that make up the sample [14].

In relation to the nanofabrication process, the first step consists of completely cleaning the substrate, which is typically silicon. The substrate is immersed in acetone and subjected to ultrasonic cleaning for three minutes. After this, it is immersed in isopropyl alcohol and then in deionized water, with both processes also carried out for three minutes in the ultrasonic bath to ensure the complete removal of any residues. If necessary, it is also possible to use plasma procedures to remove contaminants.

The next step consists of applying a layer of electron-sensitive resist such as polymethylmethacrylate (PMMA) on the surface of the silicon substrate (Fig. 31**(a)**). This process is done by spin-coating, which controls the thickness of the resist by the rotation speed. After that, the sample receives a heat treatment and is heated to improve the adhesion of the resist to the substrate. Both the rotation speed and the heating temperature depend on the type of resist used.

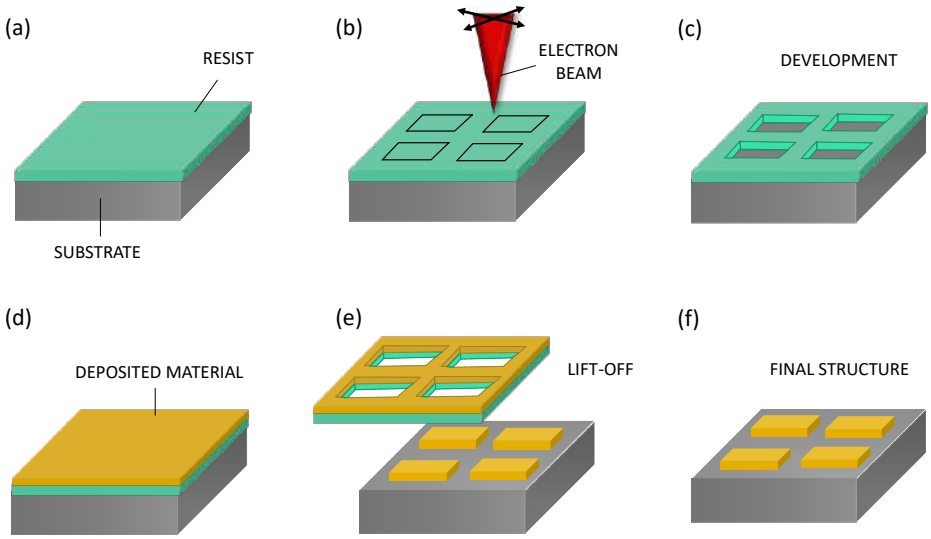

Figure 31: Sample nanofabrication process using EBL. (**a**) A silicon substrate was covered by a positive PMMA electroresist, which is chemically sensitive to the electron beam. (**b**) The silicon covered by the resist is exposed to a focused electron beam, used to establish both the shape of the nanomagnets and the shape of the contacts for samples that would be characterized by magnetoresistance. (**c**) After this, a chemical developing solvent is used to remove the areas of the resist exposed to the beam. (**d**) Permalloy, the material from which nanomagnets are made, is deposited on the entire surface above the resist, even covering the areas where the resist was removed. (**e**) A chemical lift-off process using acetone was carried out to remove all the resist from the silicon substrate, leaving only the permalloy on it. (**f**) Final structure of the sample deposited on the silicon substrate with the desired shape.

After that, the sample is ready to be taken to the FEG equipment. The areas that will be exposed to the electron beam are pre-determined digitally before the lithography process using software (in this case, the software used is *KLayout*) linked to the equipment, which allows for the digitization of the desired shapes and patterns. This process is described in Fig. 31**(b)**.

The areas of the resist that are exposed to the beam have their chemical properties changed, depending on the type of resist, which is crucial for the next step: development (Fig. 31**(c)**). In the case of so-called positive resists, exposure breaks the polymer chains and becomes soluble in the developing solvent. Therefore, in the development process, the areas that were exposed by the beam are removed. In negative resists, the exposed areas are cross-linked and are not soluble in the developing solvent. In the case of this work, the resist used was positive, so that the areas of the resist exposed to the electron beam were removed, leaving specific parts of the substrate exposed.

Continuing the process, the material from which the sample is made (in the case of ASIs, this material is permalloy) is deposited over the entire surface, covering the areas with and without resist (Fig. 31**(d)**). The processes used for permalloy deposition will be covered in the next sections of this chapter.

Afterwards, a chemical process is carried out using acetone to remove the resist, called *lift-off*. At this stage, the material deposited above the resist is also removed from the substrate (Fig. 31**(e)**). The final result of the structure consists of the material deposited above the substrate with the specific desired shape, determined at the beginning of the lithographic process (Fig. 31**(f)**).

5.2 Sputtering

Sputtering is a physical vapor deposition technique that consists of ionizing molecules of an inert gas and accelerating them toward the surface of a certain material of interest, called *target*, so that the atoms of this material are ejected due to the transfer of momentum after the collision. Some of these ejected atoms travel and deposit themselves on a substrate, forming a layer of the desired material on it. In this work, the technique used was the so-called *magnetron sputtering*, whose schematic representation can be seen in Fig. 32, and the processes involved in it will be detailed below.

The sputtering process takes place in an evacuated chamber with very low pressure

(the so-called base pressure) of the order of 10^{-6} torr. This low pressure is maintained to eliminate impurities inside the chamber and ensure that other atoms do not contaminate the sample during the deposition of the material of interest. After the base pressure is reached, a gas is injected to be ionized, as the ions must be fired at the target material in the plasma medium. This gas must be from the group of noble gases in the last column of the periodic table, as it must have a considerable atomic weight and cannot react chemically with the target material. In general, the most used gas is argon (Ar) due to its low cost, chemical inertness and ability to provide high sputtering performance [15,61]. During gas injection, the chamber is constantly evacuated by pumps, maintaining a working pressure of the order of 10^{-3} torr.

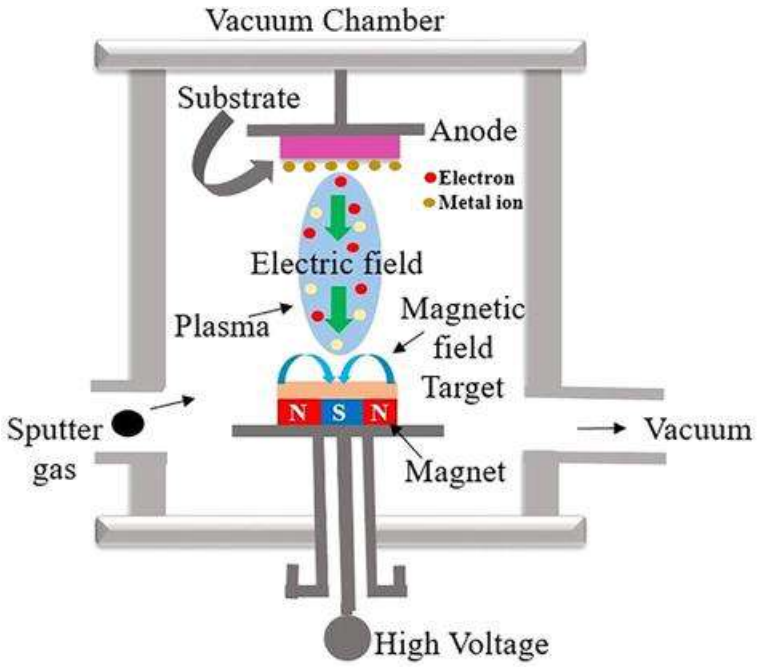

Figure 32: Schematic representation of a typical magnetron sputtering deposition system. Figure taken from Ref. [15].

Gaseous plasma is composed of neutral atoms, ions, electrons and photons. It is created by applying a DC or RF voltage to the system's cathode, which corresponds to the target material. As the substrate (or chamber) is considered the anode of the system, the potential difference applied between the target (cathode) and the substrate (anode) generates an electric field, thus accelerating the free electrons present in the chamber, which collide with neutral atoms of argon, ionizing them. This causes electrons from the last layers of Ar atoms to be ejected, creating a cascade effect and, consequently, ionizing all the gas in the chamber [61].

These created ions are accelerated towards the target material and there is a collision between them, resulting in a transfer of kinetic energy from the ions to the atoms of the material and, consequently, the ejection of some of these atoms. Those that are more energetic reach the substrate and are deposited on its surface. During the deposition process, the kinetic energy of the atoms is redistributed on the surface of the substrate, creating bonds between them and forming the first layer of the film. If the kinetic energy of the ions is much greater than the binding energy of the surface atoms of the target, they can damage the target and even the substrate [15, 61].

As targets are exposed to external factors when not in the chamber, they can become contaminated by impurities or oxidized. Therefore, before the deposition of the target material on the substrate is carried out, a pre-sputtering process is carried out to eliminate this unwanted layer from the target surface. In it, the target is generally covered by a shutter, so that the initial bombardment by plasma ions removes impurities and contaminants from the target's surface, and the shutter prevents them from reaching the substrate, keeping it clean. If these particles were deposited directly on the substrate, they could compromise the quality and properties of the deposited film. Furthermore, the shutter allows precise control of the start of deposition and, consequently, the thickness of the layer of material grown on the substrate, as the equipment operator has full control of when the ejection of atoms from the target material will begin. It is worth noting that the targets used in this technique are of high purity (>99.5%), requiring the removal of only surface atoms during the cleaning process in the pre-sputtering process [15, 61].

There are some classifications of sputtering processes depending on the way the plasma is produced. The main ones are: DC sputtering, RF sputtering and magnetron sputtering. In DC Sputtering, the plasma is formed and sustained by applying a DC voltage, making it a suitable method for metals and materials that are electrically conductive. This is because if insulating materials are used in this method, they accumulate positive charges and limit the sputtering process. The DC power supply used in this method is less complex, and has a lower manufacturing cost. In the process of RF sputtering, a radio frequency voltage (usually 13.56 MHz) is applied to the cathode to generate the plasma, rather than a direct voltage. This causes a continuous change of the negative/positive pole, preventing the accumulation of charge on the surface of insulating targets. However, both methods have low ionization efficiency, as most of the electrons disperse and collide with the chamber walls, not interacting with the Ar molecules to

produce the plasma [15, 61].

In the magnetron sputtering method, some permanent magnets are placed close to the target, the cathode, in order to create a magnetic field to confine the electrons close to the surface of the target. This generates an increase in gas ionization, in addition to a greater rate, efficiency and quality of deposition. Magnetron sputtering uses both DC and RF sources, depending on the nature of the target, but the equipment is more complex and has a higher initial cost compared to those previously mentioned [61].

5.3 Electrodeposition

The electrodeposition technique is an electrochemical process used to form clusters and even for the growth of thin films through reactions at solid/liquid interfaces. The process begins with small agglomerates, then they form nuclei that are distributed throughout the substrate until generating a structure that covers the entire surface. It has several advantages as it is simple to implement under ambient temperature and pressure conditions, has a low cost, provides rapid deposition of materials, and is highly reproducible.

The process is carried out in an electrochemical cell containing two electrodes immersed in an ionic solution (or electrolyte), so that both are controlled by an external source. Electrodeposits are formed from reduction reactions of ions in the solution caused by the action of electrical currents. Such reduction reactions occur at the cathode, which has negative polarization and is called the working electrode. In it, the metallic ions present in the electrolyte gain electrons and are deposited as a solid metal on its surface. The anode is called the counter electrode and is essential for closing the electrical circuit. It is where oxidation reactions take place, considering that its metal atoms lose electrons to the electrolyte, causing metal ions to be formed in the solution. Thus, the solution that forms the electrolyte contains positive and negative ions from the dissociation of metallic salts, and it is through it that the electric current flows between the electrodes, more specifically from the anode to the cathode [18, 62].

In the formation of the deposit, the transport of ions to the working electrode is governed by the mechanisms of diffusion, migration and convection. Diffusion is the process by which ions move from a region of high concentration to a region of low concentration, due to the concentration gradient, seeking to balance the concentration of

ions in the solution. Migration occurs under the influence of an applied electric field, causing charged ions to move toward the oppositely charged electrode, facilitating deposition. Convection, in turn, involves the movement of ions caused by flow currents in the solution, which can be induced mechanically (agitation) or thermally (temperature differences), helping to continually renew the layer of solution close to the electrode and promoting a more efficient transport of ions. These three mechanisms work together to ensure that ions reach the working electrode effectively, allowing the desired deposit to form [62].

In this work, potentiostatic electrodeposition was used, that is, the potential at the working electrode is kept constant in relation to the so-called reference electrode, which also makes up the electrolytic cell and allows the potential to be measured separately at each electrode. The cell configuration containing the reference electrode, the working electrode, the counter electrode and a potentiostat can be seen in Fig. 33. The potentiostat is an electronic device that controls the potential difference between the working electrode and the counter electrode, maintaining the potential difference between the working electrode and the reference electrode.

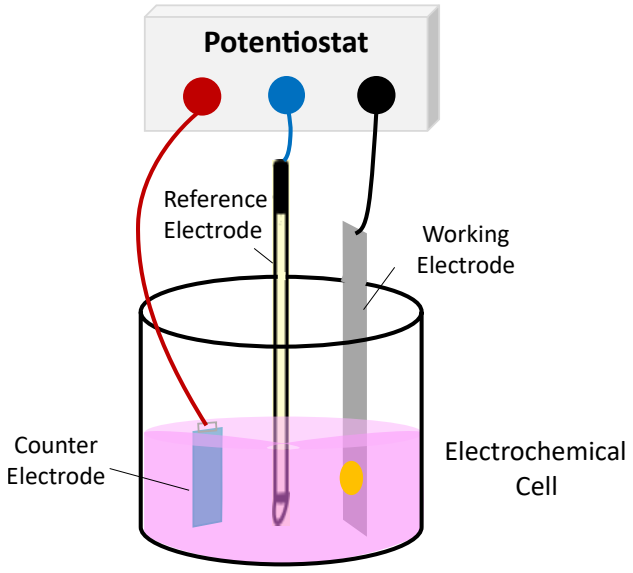

Figure 33: Illustration of an electrochemical cell containing the reference electrode, the working electrode, the counter electrode and the potentiostat.

As this process involves transferring electrons from an electrode to an electrolyte, by measuring the current in the cell it is possible to calculate the thickness of the deposited material. Assuming that no other parallel reaction occurs, that the reaction at the working electrode is simple reduction, and that all ions are reduced on the electrode surface, the

amount of electrodeposited material can be calculated from the electrodeposited charge, determined by the integration of current transient ($Q = \int idt$). This is possible using the expressions for density ($d = m/V$), charge ($Q = Nne$), height ($h = V/A$), and Faraday constant ($F = N_a e = 96485\ \mathrm{C} \cdot \mathrm{mol}^{-1}$) . Here, N corresponds to the number of atoms and can be expressed as $N = mN_aM$, where m is the electrodeposited mass, $N_a = 6.02 \times 10^{23}$ is the Avogadro number (number of atoms in one mole), M is the atomic weight, A is the area to be deposited, and V is the volume of material deposited. The thickness will then be determined by the Eq. 5.1:

$$h = \frac{MQ}{ndAF} \tag{5.1}$$

5.4 Atomic Force Microscopy and Magnetic Force Microscopy

The morphology and local surface properties of a sample are usually obtained by scanning probe microscopy (SPM), a generic name for a variety of techniques that use a mechanical probe to detect detect different surface features of the material. Each technique varies depending on the interaction between the probe and the sample, and the main ones are: scanning tunneling microscopy (STM), atomic force microscopy (AFM), electrical force microscopy (EFM), magnetic force microscopy (MFM) and scanning near-field optical microscopy (SNOM) [16]. Despite providing different information about the object of study, they all have the same basic operating principle. However, in this section we will mainly emphasize the working mechanism of the AFM and MFM techniques, as they were used to develop the work.

AFM is an excellent method for obtaining three-dimensional images containing information on the topography and roughness of the sample, with a vertical resolution of the order of 0.5 Å. Its operating principle (Fig. 34) is based on the use of a mechanical probe (tip + cantilever) placed in contact or very close to the sample surface, creating a highly localized physical interaction between them. A piezoelectric[1] scanner promotes lateral movement of the sample in relation to the probe, following a scanning pattern. During this scan, the surface roughness interferes with the tip-sample interaction, generating deflections in the cantilever. These deflections are monitored by an optical mechanism

[1] A piezoelectric material can generate electrical voltage in response to an applied mechanical stress, due to the accumulation of charges on the surface of the material.

consisting of a laser beam, which is reflected and directed to a four-quadrant photodetector. The difference in the intensity of the detected laser causes changes in the received signal relative to the sample surface, and this information is passed to a feedback system in the positioning of the piezoelectric scanner that controls the vertical position of the probe, and consequently the distance between the tip and the sample. A computer controls the process, moving the scanner, receiving and converting the data to form the sample image. More specifically, the value is first recorded as a function of coordinates (X,Y) and is then translated into topography Z(X,Y) [16, 60].

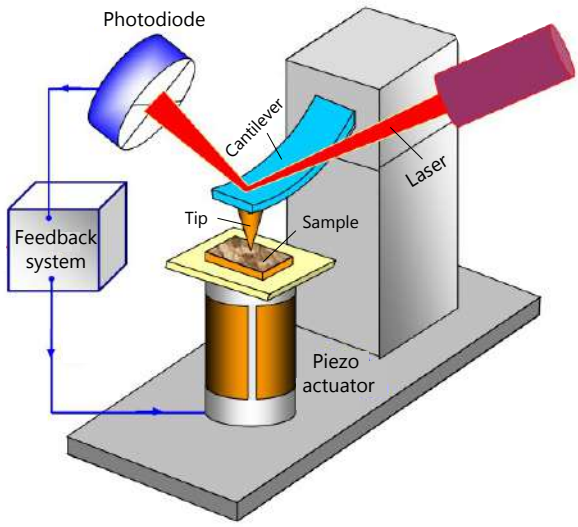

Figure 34: Schematic representation of the AFM components. Figure adapted from Ref. [16].

The AFM image acquisition modes are related to the interactive forces between the probe and sample considering the distance between them, and can be explained based on van der Waals forces. The van der Waals potential energy of two atoms, located at a distance r from each other, is approximated by the exponential function (Lennard-Jones potential) described in Eq. 5.2:

$$U_{LD}(r) = U_0 \left\{ -2 \left(\frac{r_0}{r} \right)^6 + \left(\frac{r_0}{r} \right)^{12} \right\} \tag{5.2}$$

The first term of the sum describes the long-distance attraction caused, basically, by a dipole-dipole interaction. The second considers short-range repulsion due to the Pauli exclusion principle. The parameter r_0 is the equilibrium distance between the atoms, and U_0 is the lowest energy value. Although, in fact, the interaction between tip and sample has a more complex character, roughly speaking, it can be said that the tip is attracted

when it is at great distances from the sample, and repelled when it is at small distances. This behavior is qualitatively described in Fig. 35.

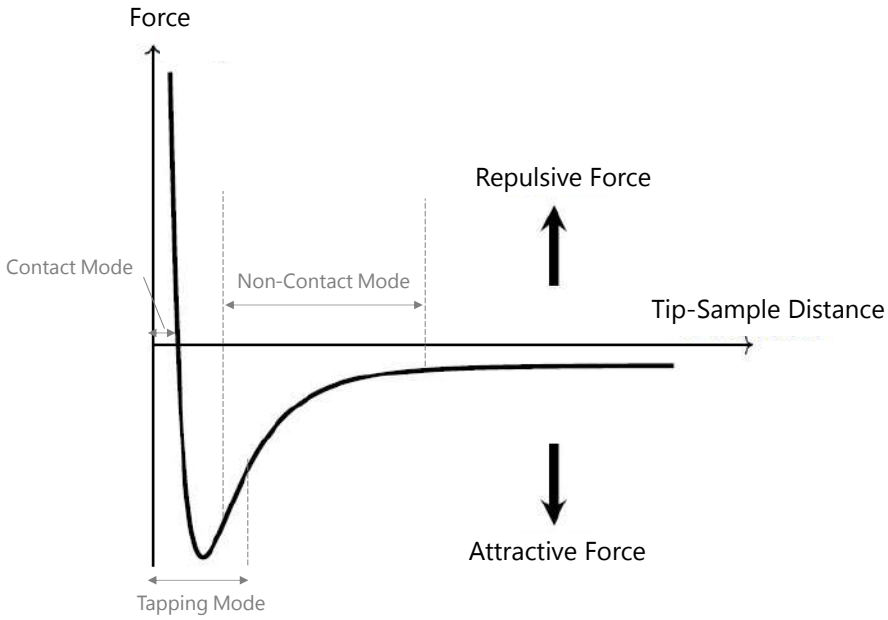

Figure 35: Behavior of the probe-sample interaction force as a function of the separation distance between them. Figure adapted from Ref. [17].

The methods used in AFM to acquire images are classified as contact, non-contact, and semi-contact modes. In contact mode, the tip is in direct contact with the surface and the probe-sample interaction becomes dominated by repulsive forces. The cantilevers used in this mode have low rigidity and high sensitivity, and the best results using this mode are achieved on hard sample surfaces, without steep edges or points. However, although the risks of damaging the sample are minimal, detecting changes in the amplitude and phase of cantilever oscillations in this mode requires very high sensitivity and stability of the feedback system. In practice, the most used mode is semi-contact, also called *intermittent-contact mode* or *tapping mode*. This was the mode used to carry out the measurements contained in this work, and in it the probe is forced to oscillate close to the resonant frequency of the cantilever with an amplitude of around 10 to 100 nm. During cantilever oscillation, the tip comes into contact with the surface at the lower end of its vertical movement, which corresponds to the repulsive interaction region in the force-distance diagram. During scanning, changes in amplitude and phase of the cantilever oscillations are recorded, while the oscillation frequency remains constant [20, 60, 63].

In addition to topographic analysis of samples, AFM offers several other functionalities depending on the tip used. One notable functionality is the investigation of

the distribution of magnetization on material surfaces using MFM technique. For MFM, the tip must be coated with a ferromagnetic material with specific magnetization. This technique operates in intermittent-contact mode, allowing the distribution of magnetic domains to be associated with the sample's surface morphology. Typically, MFM uses a two-pass method to distinguish magnetic signals from other types of interactions (Fig. 36). The first pass aims to obtain the topographic image of the material's surface. In the second pass, the probe is raised to a height, chosen by the operator, ranging from 10 to 500 nm. The probe then scans at this constant height, using the information obtained from the first pass. This approach helps to isolate the magnetic interaction signal from the influence of the material's topographic properties, providing a clear observation of the magnetic domains. [20, 60].

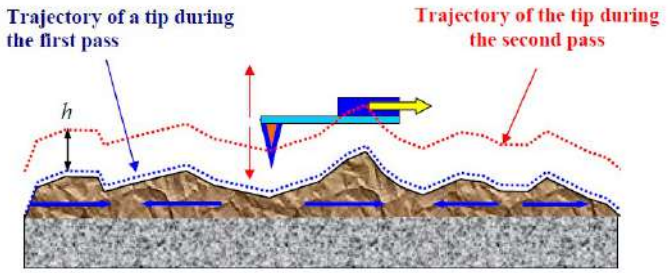

Figure 36: Two-pass technique of the MFM acquisition. Figure taken from Ref. [16].

5.5 Magnetoresistance

Magnetoresistance (MR) consists of the change in electrical resistance to the transport of electric current in materials when they are subjected to the application of external magnetic fields. This effect has been fundamental to technological advances in areas such as magnetic sensors and data storage. There are different types of magnetoresistance, each with its specific characteristics and mechanisms.

Ordinary magnetoresistance (OMR), also known as classical or normal magnetoresistance, is a fundamental phenomenon observed in non-magnetic conductive and semiconductor materials when they are subjected to an external magnetic field. It is characterized by a change in the electrical resistance of the material due to the presence of the magnetic field [18].

The primary mechanism behind OMR is the Lorentz force, which acts on the charge carriers moving through the material. When a magnetic field is applied perpendicular

to the flow of current, the Lorentz force causes charge carriers to experience a curved trajectory. This curvature results in an increased path length for charge carriers as they pass through the material, effectively increasing their scattering events and, consequently, electrical resistance. If the magnetic field is applied in a different direction, there will still be a change in resistance, but this change will be less pronounced than in the perpendicular case [18, 64].

Anisotropic magnetoresistance (AMR) is a phenomenon where the electrical resistance of a material changes depending on the angle between the direction of current and the magnetization of the material. This effect is particularly prominent in ferromagnetic materials such as iron, nickel and cobalt. Discovered by William Thomson in 1857, AMR arises from the intrinsic properties of the electronic structure of these materials [64].

When the magnetic field is parallel to the applied electric current, the so-called longitudinal AMR, magnetoresistance is negative, as the resistance value is lower with zero magnetic field and increases with the application of an external field. For a perpendicular orientation between current and field, which characterizes transverse AMR, the magnetoresistance is positive, as the resistance with zero magnetic field is greater than with the application of an external field. This behavior can be better seen in Fig. 37, and occurs because the density of states at the Fermi level, which affects electron scattering, changes with the direction of magnetization. Therefore, the spin-orbit interaction in ferromagnetic materials causes this anisotropy in electron scattering [18, 64].

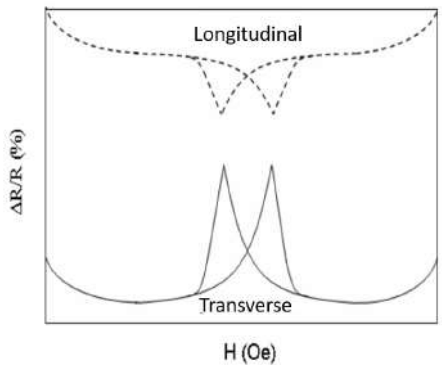

Figure 37: Longitudinal and transverse AMR curve for ferromagnetic materials. Figure taken from Ref. [18].

The separation between the peaks observed in the curves in the Figure comes from the coercivity of the material. As the magnetic domains tend to align with the external field, the field value at the magnetoresistance peak corresponds to the field necessary to

invert the material's magnetization, called the coercive field H_c. Above this point, the magnetization saturates in the direction of the external field [18].

Another type of magnetoresistance is the so-called giant magnetoresistance (GMR). Its discovery in 1988 by Baibich et al. [65] opened a path for the efficient control of charges and spins in ferromagnetic materials with major applications in current electronics. Devices that feature GMR are spintronic devices that use nanostructured metallic multilayers to generate spin currents, being able to transfer information, reduce energy consumption, in addition to being faster than conventional semiconductor devices.

In FM/NM/FM spin valve structures, where FM corresponds to a ferromagnetic material and NM to a non-magnetic metal, the relative magnetoresistance can reach values much higher than those observed in AMR. This is because when this type of structure is subjected to external magnetic fields, its resistance may undergo changes depending on the parallel and anti-parallel magnetic orientation of the ferromagnetic layers, as a result of the difference in conductivity encountered by the electrons when crossing the structure [19].

As the number of spins up and down at the Fermi level is equal in a metal, electrons pass through it with the same probability. However, in a spin polarized metal there are more Fermi level states in one direction than in another. Therefore, the configuration in which the ferromagnetic layers have parallel magnetization generates low resistance in the valve, as only electrons with spin up or down will be scattered. However, if the FM layers have anti-parallel magnetization between them, the density of states for spins up and down are inverted and both will be scattered, this being a high resistance configuration. This process is schematized in Fig. 38 [19].

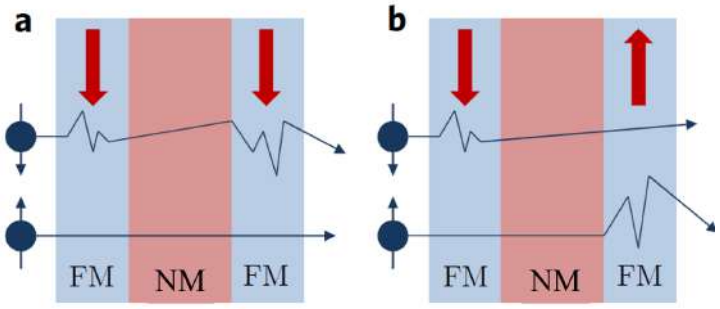

Figure 38: Schematic representation of the spin current scattering in a spin valve in relation to the **(a)** parallel magnetization orientation of the FM layers presenting low scattering for electrons with spins up (low resistance); and **(b)** high scattering of electrons for anti-parallel orientation (high resistance). Figure taken from Ref. [19].

6 Results and Discussions

In the first section of this chapter, the experimental results obtained from the MFM characterization of unconnected rectangular ASI samples with different lattice parameters will be presented and discussed. The samples were fabricated at the Iberian Institute of Nanotechnology (INL) in Portugal and characterized at UFV. In the second section, ASI samples containing connected lattices of different geometries were studied. Nanofabrication and characterization processes using EBL, electrodeposition, MR, SEM, EDS, and MFM will be addressed. Both the nanofabrication and characterization of these samples were performed at UFV.

In both sections, the methodologies used and the characteristics of the samples will be described in detail. The main objective of these investigations was to experimentally verify the ground state degeneracy theoretically predicted for certain geometries, as discussed previously.

6.1 Unconnected Lattices

In this first study, the samples were nanofabricated at the INL using EBL and sputtering, with matrices of 100 μm x 100 μm of nanomagnets composed of 3 nm tantalum/ 20 nm permalloy/ 3 nm of tantalum, sized 3 μm $\times$ 400 nm on a commercial silicon substrate. Tantalum layers were used both to improve adhesion and as a cover layer to prevent oxidation of the magnetic material. Permalloy, as previously mentioned, guarantees the stability of the system at room temperature, ensuring that thermal excitations do not alter the magnetization of the nanoislands, and making it possible to obtain MFM images of the samples. Furthermore, three different types of unconnected lattice geometries were investigated: the ratio $\gamma = a/b$ of each of them was equal to $\sqrt{2}, \sqrt{3}$ and $\sqrt{4}$, which will be described in this work respectively by R2, R3 and R4.

To try to observe the freedom of magnetic monopoles emerging in the lattice, different values of magnetic fields were applied to the samples in different directions, so that after each application they were characterized by MFM in the Department of Physics at UFV. This made it possible to probe the topologies formed at the vertices as the fields were applied, until the magnetization was saturated in a direction opposite to the initial

saturation direction.

Firstly, a source was used to apply different values of electric current to a cylindrical coil, generating a uniform magnetic field inside it. The samples were positioned horizontally, vertically, and diagonally in relation to the coil, both immediately at the end of its extension and in its central region, as can be seen in Fig. 39. The proportionality factor between the currents and the field produced was 405 Oe/A, a value extracted from the calibration curve that can be seen in Fig. 40.

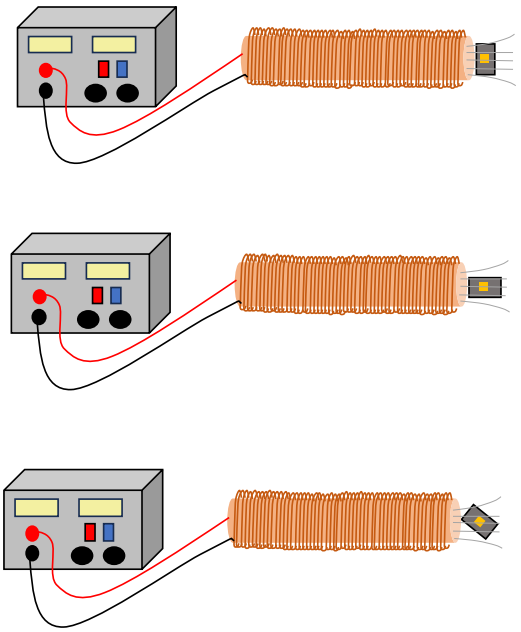

Figure 39: Schematic representation of field application in horizontal, vertical and diagonal directions using a coil.

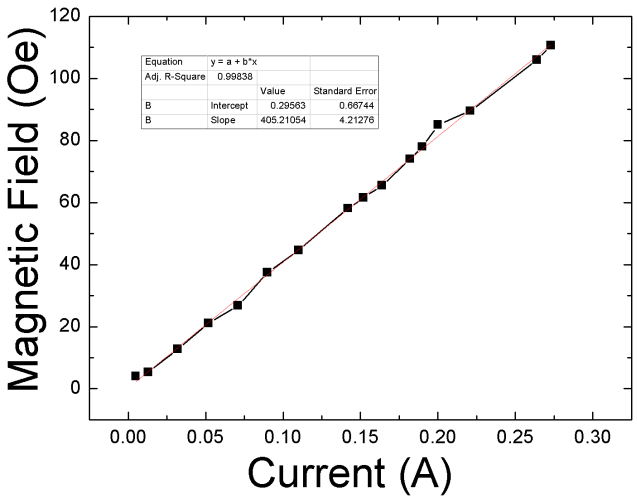

Figure 40: Correspondence curve between current applied to the coil and generated magnetic field. The angular coefficient of the red line obtained in the linear adjustment was (405 ± 4) Oe/A.

Before applying different values of magnetic fields to the samples, all of them were subjected to a field of 245 Oe in the negative direction of the horizontal, vertical, or diagonal axis, ensuring that all nanoislands were magnetized in the same direction. This initial step was verified by MFM characterization. After that, increasingly larger magnetic fields were applied in the opposite direction to the initial magnetization on each sample for 3 seconds in the three directions. The first field applied in the opposite direction to the initial magnetization was approximately 50 Oe. Subsequently, the application occurred in increments of approximately 10 Oe, up to approximately 220 Oe. For each applied field, the distribution of magnetic moments was verified using the MFM, and an example of these measurements can be seen in Fig. 41.

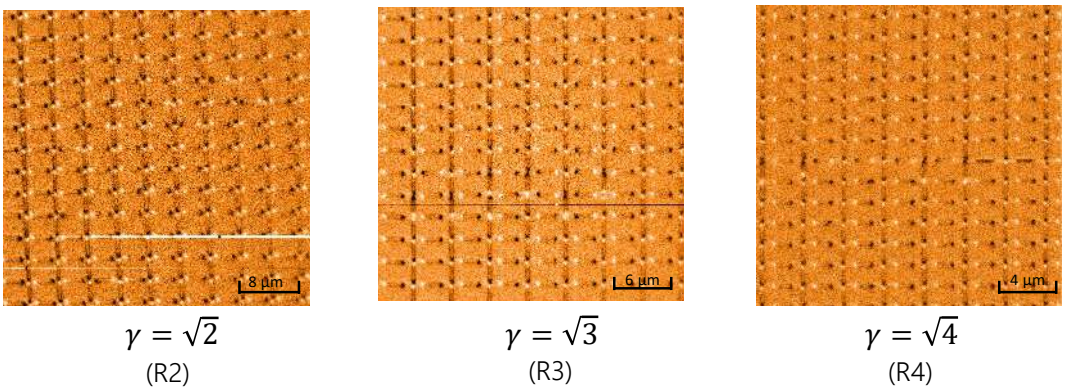

Figure 41: MFM measurements of samples R2, R3 and R4.

The experimental procedure basically consisted of enabling a magnetic reversal process in the samples. On average, measurements were repeated around three times, with irrelevant differences obtained. It is worth noting that the field application did not occur close to the MFM equipment to avoid possible interference in the system, which could compromise both the reliability of the results obtained and the functionality of the equipment. Furthermore, all MFM measurements were made in the same region of the sample. This could only be done by choosing a region close to the edge. It is important to highlight that the edges that had incomplete vertices were not taken into account in the analyzes carried out, although their effects were not negligible.

Since the main objective of this work was to observe the freedom of emerging monopoles in the lattice as a consequence of the degeneracy of the ground state and the reduction of the string energy connecting monopole-antimonopole pairs, there was a significant focus on monitoring the behavior of T_3 topology vertices with the images obtained by MFM. Those with three spins pointing towards the center of the vertex were

called T_{3I} (or T_3-in), and those with three spins pointing outwards from the vertex were called T_{3O} (or T_3-out). Both form a monopole-antimonopole pair, and their configurations are outlined in Fig. 42.

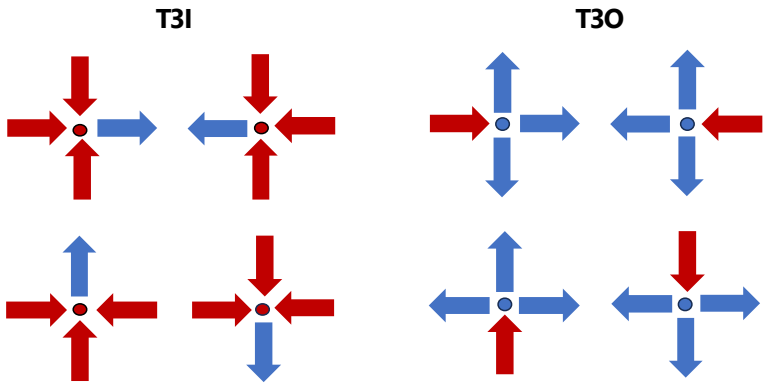

Figure 42: Representation of T_{3I} (or T_3-in) and T_{3O} (or T_3-out) topologies.

The results obtained for sample R2 can be seen in Fig. 43. It shows the percentages of each topology formed at the vertices after applying different magnetic field values in the horizontal, vertical, and diagonal directions, respectively. It is possible to notice that, for the three directions, when the sample is initially saturated, the vertices only present T_2 topologies. As the external field increases, the T_2 topologies become mostly T_3, until the sample saturates again in the opposite direction and the topology returns to being just T_2. In these graphs, the T_3 topology represents the sum of T_{3I} and T_{3O}. Additionally, it is worth noting that the samples did not undergo thermal annealing to reach the initial minimum energy configuration. Therefore, for these experimental results, the percentage of T_1 and T_2 topologies in the samples is not a good indication or parameter of ground state degeneracy.

When analyzing the evolution of the T_3 topology for horizontally applied fields (Fig. 43**(a)**), it is observed that they evolve by the same amount gradually from 50 Oe to 180 Oe, together reaching the maximum value around 50% of the sample vertices when the applied field is approximately 150 Oe. The appearance of such vertices is clear evidence of the emergence of magnetic monopole pairs in the system, while their decrease indicates the annihilation of the pairs. In this case, the recombination and annihilation processes occur in the field range from 150 Oe to 180 Oe. For the vertically applied field (Fig. 43**(b)**), there is a large creation of monopoles close to 120 Oe, to reach a maximum value of around 40% in a field of 140 Oe. Recombination and annihilation occur over a wider range of magnetic field, from 140 Oe to 220 Oe. For the field applied diagonally to

the sample (Fig. 43**(c)**), creation occurs at around 140 Oe, and annihilation at around 200 Oe, both being very sharp. A plateau with a higher population of monopoles occurs around 50%, being observed in the range from 160 Oe to 190 Oe.

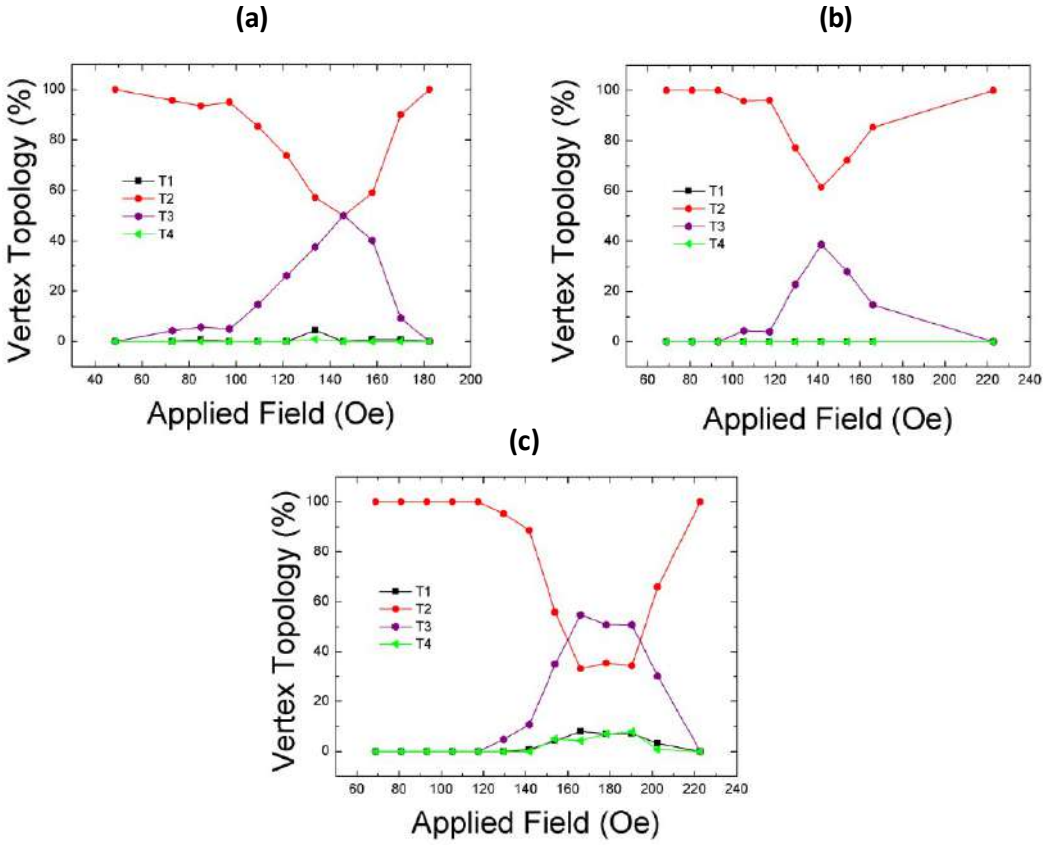

Figure 43: Evolution of the topologies of sample R2 as a function of the external magnetic field applied **(a)** horizontally; **(b)** vertically; **(c)** diagonally.

The differences observed in the vertices created for each applied field direction may be related to the dipolar interaction between the nanomagnets, considering that the vertical distance between the nanomagnets was smaller than the horizontal distance. Furthermore, the approximate equality of both the creation and recombination and annihilation of the topologies of opposing magnetic monopoles T_{3I} and T_{3O} for each applied external field direction stands out, as evidenced in the Fig. 44. This behavior is expected, since there is an energy chain in the main axes of the system. The small deviations may be associated with fixed monopoles at the edges observed during the characterization.

Differently from what occurs in sample R2, for the field applied horizontally in sample R3, the maximum population of monopoles (50%) occurs in a lower field, around 120 Oe, as can be seen in Fig. 45. Furthermore, the greater observation of T_1 topologies from 110 Oe to 160 Oe when the field is applied horizontally, and from 180 Oe to 210

Oe when the field is applied diagonally, may be an experimental sign of the system's degeneracy, although the samples did not undergo thermal annealing and this is not a strong indication. When the field is applied vertically, T_3 are approximately 30% of the topologies around 140 Oe, and when it is applied diagonally, again T_{3I} and T_{3O} are about 50% of the total system vertices, occurring around 190 Oe.

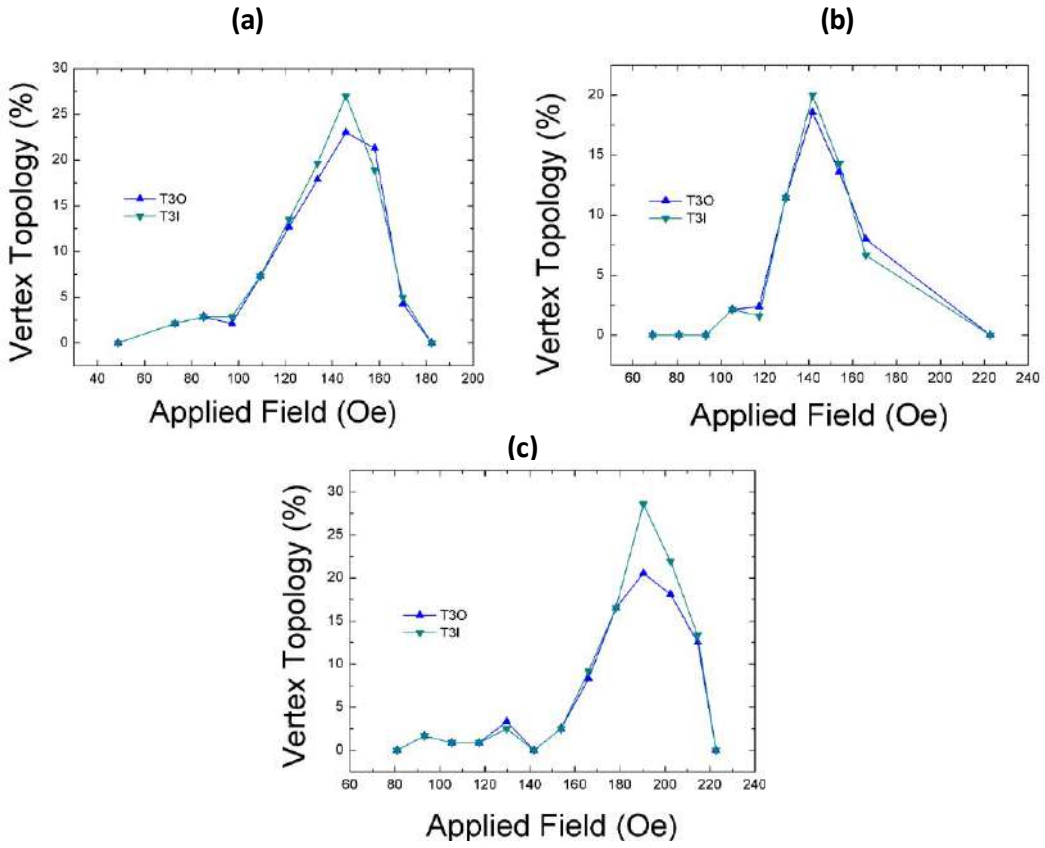

Figure 44: Evolution of the vertices T_{3I} and T_{3O} as a function of the external magnetic field applied **(a)** horizontally; **(b)** vertically; **(c)** diagonally in sample R2.

Additionally, it is possible to observe a significant difference between the creation, recombination and annihilation of the T_{3I} and T_{3O} topologies in Fig. 46. Such monopoles considerably stop evolving in the same number when the field is applied horizontally, and in a more discrete way when the field is applied vertically and diagonally. Once a number of magnetic monopole pairs are created in the system, such vertices should appear equally filled. Due to charge conservation, any incompatibility between the number of T_{3I} and T_{3O} measured in the same region must be seen as the emergence of unpaired monopoles, which are considerably far apart in the lattice, due to the decrease in the energy of the string that connects them. When the field is applied vertically and diagonally, one of the possible reasons for the incompatibility not being so evident also involves the dipolar

interaction between the nanomagnets in these directions, considering that there was no change in the b parameter between samples R2, R3 and R4.

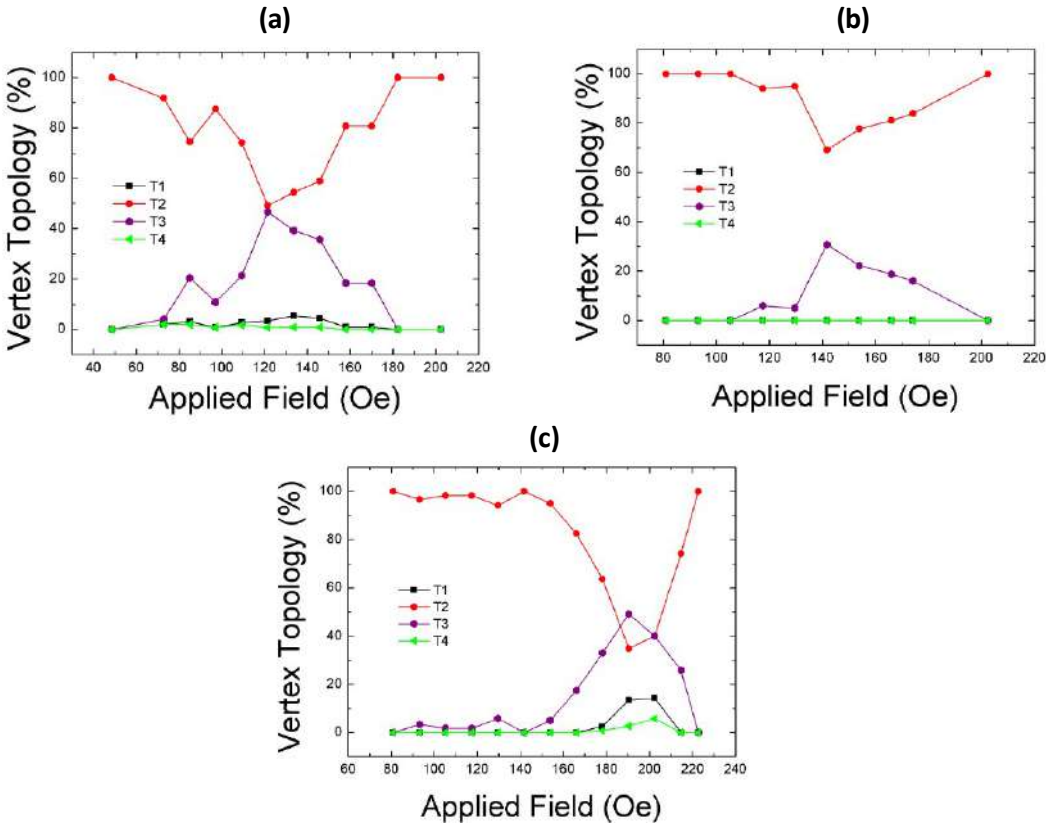

Figure 45: Evolution of the topologies of sample R3 as a function of the external magnetic field applied **(a)** horizontally; **(b)** vertically; **(c)** diagonally.

In Fig. 47, it is possible to observe the behavior of the monopoles in a small part of the sample, more specifically in a matrix of 6 x 6 vertices, for the horizontally applied field in this system with a low energy string. In each item in Fig. 47, the field grows approximately 10 Oe. In item **i)**, with the field around 75 Oe, pairs of monopoles are created. With a small increase in the field to 85 Oe, shown in item **ii)**, more pairs are generated and free monopoles begin to move. In items **iii)** and **iv)** for fields larger than 95 Oe and 125 Oe, it is possible to note the extension, annihilation and unpairing of pairs of monopoles, providing greater freedom of circulation in the lattice. Finally, in items **v)** and **vi)**, acquired in the fields of 170 Oe and 205 Oe, respectively, there is the annihilation of the last pairs of monopoles and it is possible to notice the path left by the free monopoles that crossed the arrangement.

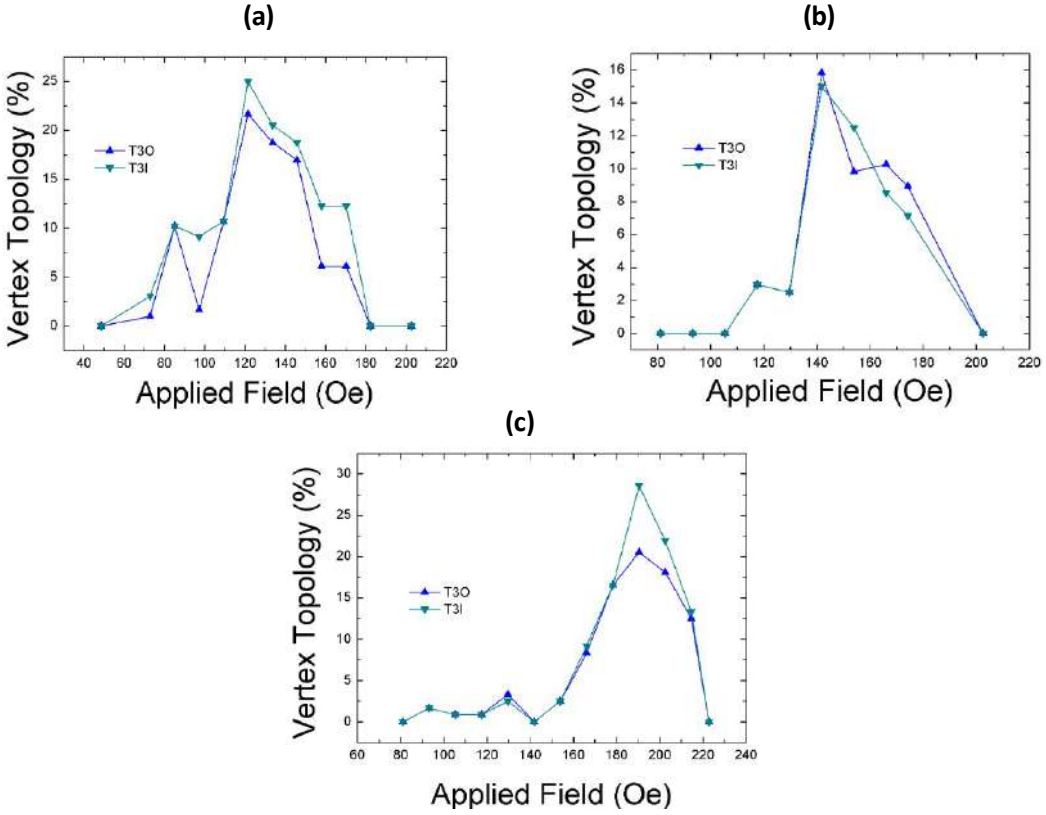

Figure 46: Evolution of the vertices T_{3I} and T_{3O} as a function of the external magnetic field applied **(a)** horizontally; **(b)** vertically; **(c)** diagonally in sample R3.

Finally, the results obtained from MFM measurements of the topologies formed with the application of external magnetic fields for sample R4 are presented in the graphs in Fig. 48, while the behavior of the emerging magnetic monopoles T_{3I} and T_{3O} can be seen in the graphs in Fig. 49. For sample R4, it can be seen that the energy of the system string increases again, and the unpairing of free monopoles observed in sample R3 no longer occurs. The small differences during the creation and annihilation of T_{3I} and T_{3O} for fields applied horizontally, vertically, and diagonally may also be related to edge effects.

In this geometry, due to the almost non-interaction between neighboring nanomagnetic bands resulting from the large spacing between nanomagnets, the magnetic monopoles evolve to form domain walls between themselves, in a similar way to what is present for a unidirectional lattice [66, 67]. This behavior was verified experimentally, as explained in Fig. 50.

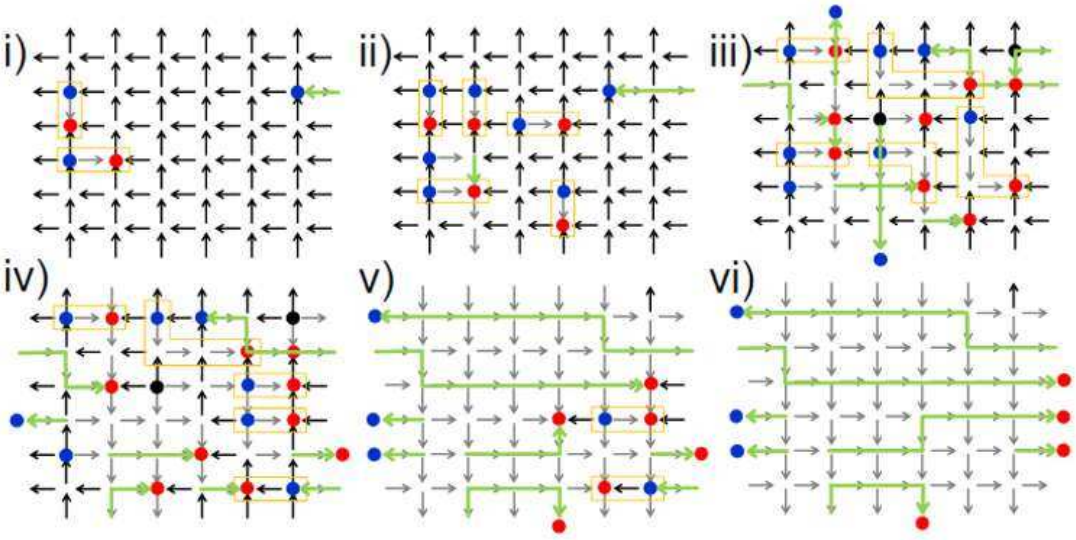

Figure 47: Creation, transport and annihilation of emerging monopoles observed in the same region of sample R3 as the value of the applied external magnetic field increased.

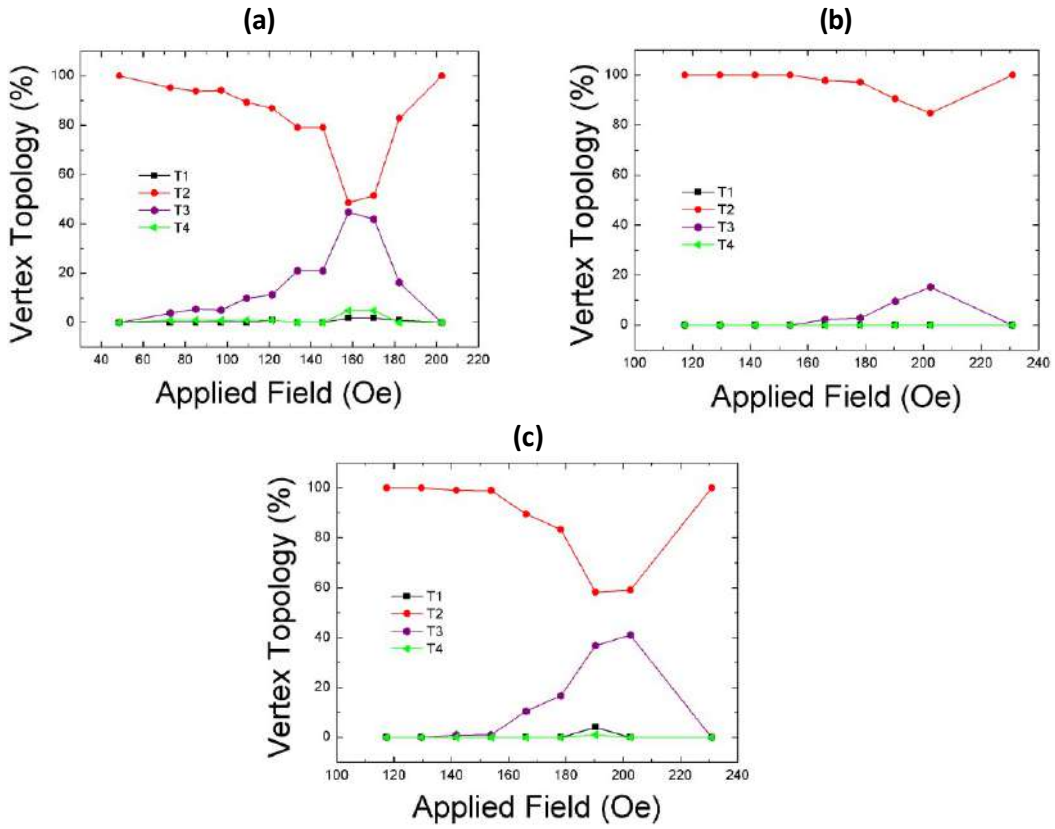

Figure 48: Evolution of the topologies of sample R4 as a function of the external magnetic field applied **(a)** horizontally; **(b)** vertically; **(c)** diagonally.

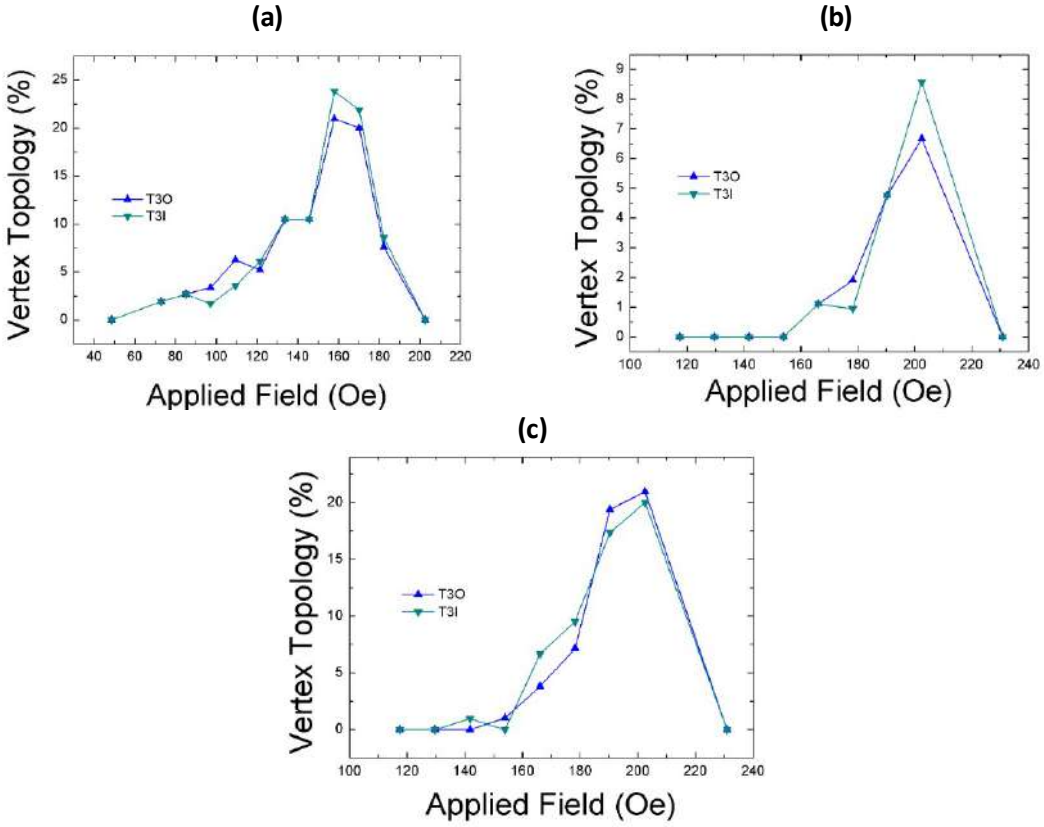

Figure 49: Evolution of the vertices T_{3I} and T_{3O} as a function of the external magnetic field applied **(a)** horizontally; **(b)** vertically; **(c)** diagonally in sample R4.

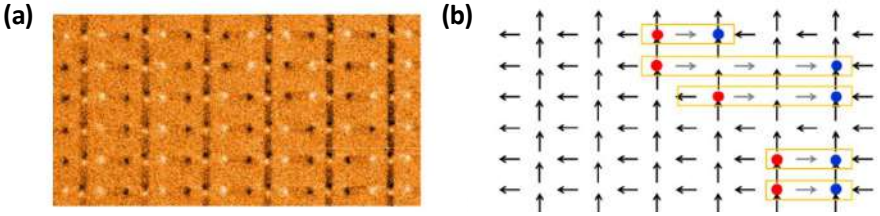

Figure 50: **(a)** Enlarged view of the MFM measurement for sample R4 with an applied field of 130 Oe. **(b)** Scheme made to better visualize the formation of domain walls in the region shown in **(a)**.

The comparison of the difference between the evolution of monopoles and their anti-monopoles for the three rectangular samples is shown in Fig. 51, for the field applied horizontally. The results show systematic and large differences for the R3 geometry, and it is worth highlighting the always positive difference between them, indicating an unequal evolution between the pairs. In the remaining samples, the differences fluctuate around zero and can be attributed to the fixation of monopoles at the edges. Furthermore, for R2 and R4, such differences are both positive and negative, indicating that the number of monopoles and antimonopoles evolve in a very similar way in these samples.

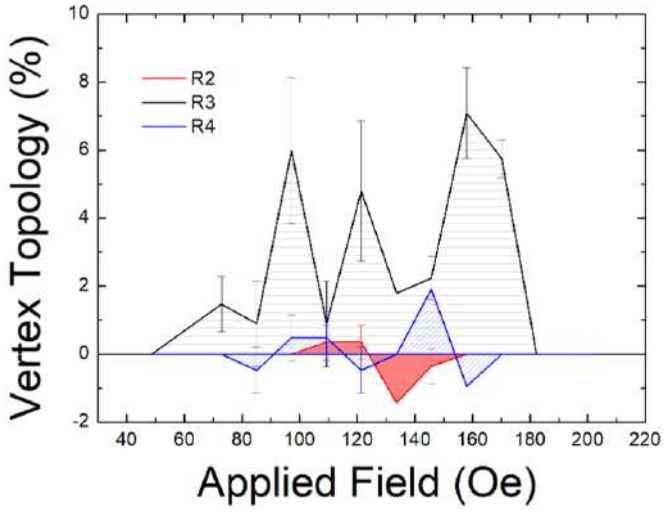

Figure 51: Difference between positive and negative monopoles during magnetization reversal with horizontally applied field, for the three geometries investigated.

6.2 Connected Lattices

In the second part of this work, the primary objective was to nanofabricate ASI lattices with different geometries using EBL at the Physics Department of UFV under 30keV. This technique allows the fabrication of nanostructures on the order of a few tens of nanometers with great resolving power and high quality, as discussed previously. The goal was to experimentally investigate, by comparing the results obtained through various characterizations, the degeneracy of the ground state in a two-dimensional square geometry lattice with connected nanomagnets, as theoretically predicted. More specifically, four geometries were fabricated, with ratio $\gamma = a/b$ varying between 1, $\sqrt{2}$, $\sqrt{3}$ and $\sqrt{4}$, which will be referred to in this work as Q, R2, R3 and R4 respectively. Each of these geometries was characterized at UFV using SEM and MR.

Furthermore, we demonstrated that Permalloy can be deposited using the electrodeposition technique to obtain high-quality samples. To showcase the quality of the samples with Py grown by electrodeposition, static characterizations were performed using SEM and MFM of samples with unconnected nanomagnets.

Frequently, Permalloy is deposited to form nanomagnets using physical vapor deposition techniques such as sputtering. Although this is a great technique for producing thermodynamic samples with very thin thicknesses in order to reach the superparamagnetic regime, it has a high cost and can be a time-consuming process. In this regard, we

fabricated ASI samples using electrodeposition as an alternative material growth method. It is a cheaper and faster technique, requires little physical space to be installed, is highly reproducible, facilitates the lift-off process and the entire process is executed under ambient conditions.

However, it is challenging to produce thin and uniform films on very small areas as required for ASI samples using electrodeposition. To achieve these characteristics, the following protocol was used: n-type silicon substrates (111) with resistivity of 0.15 Ω/cm^2 were used, cleaned with acetone, isopropyl alcohol and 18 MΩ deionized water. They were dipped in 10% HF solution to remove the inherent oxide layer within the defined nanostructures. After EBL, the samples were immersed in 2% HF solution for 10s to create an environment of greater wettability, as without this process air bubbles could form inside the nanostructures developed in the hydrophobic electroresist, as represented in the sketch in Fig. 52, preventing full transfer of the desired geometry. Then, the pulsed electrodeposition process took place with the potentials being controlled with an Ag/AgCl type reference electrode in an electrochemical cell containing the solution, and a platinum counter electrode. The deposits were prepared from a solution containing an aqueous electrolyte based on: 30mM $FeSO_4$, 30mM $NiSO_4$, 2mM $NiCl_2$, 20mM saccharin and 40mM H_3BO_3 to a potential of -1.1 V. The pulsed process consists of applying a 0.5s potential pulse, waiting 1s in the cell's potential regime, and then applying the pulse again. This process guarantees the formation of more nuclei per area, making the film uniform and thinner. Decreasing the concentration makes the process slower, reducing roughness. The deposits were obtained with 12 pulses, which guaranteed a thickness of 30nm of Permalloy nanomagnets, optimal thickness for non-thermodynamic samples.

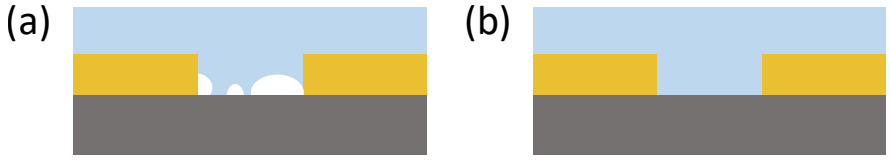

Figure 52: (**a**) Illustration of possible air bubbles formation on the hydrophobic electroresist and substrate as probable cause of non-uniformity in the geometries when the environment with improved wettability is not created. (**b**) Samples with the desired geometry due to dipping for 10s in the 2% HF solution to generate an environment of greater wettability.

To verify the quality and uniformity of Permalloy growth by electrodeposition technique and the effectiveness of the protocol described above, characterizations were

carried out by SEM and MFM, as shown in Fig. 53. In the SEM image of Fig. 53**(a)**, performed on the sample developed with constant potential deposition and no dip in 2% HF solution for 10s, it is possible to see that the lattice geometry is not homogeneous, the films obtained are presenting larger and with non-uniform grains. Those characteristics prevent a good magnetic characterization, as it can be seen in Fig. 53**(b)** showing some lack of dark and bright spots in MFM measurement, which are related to the north and south direction of each nanomagnet. Probably it happens because the large grains allow non-uniformity in sample thickness and formation of magnetic domains in plane, which are not sense by the MFM tip.

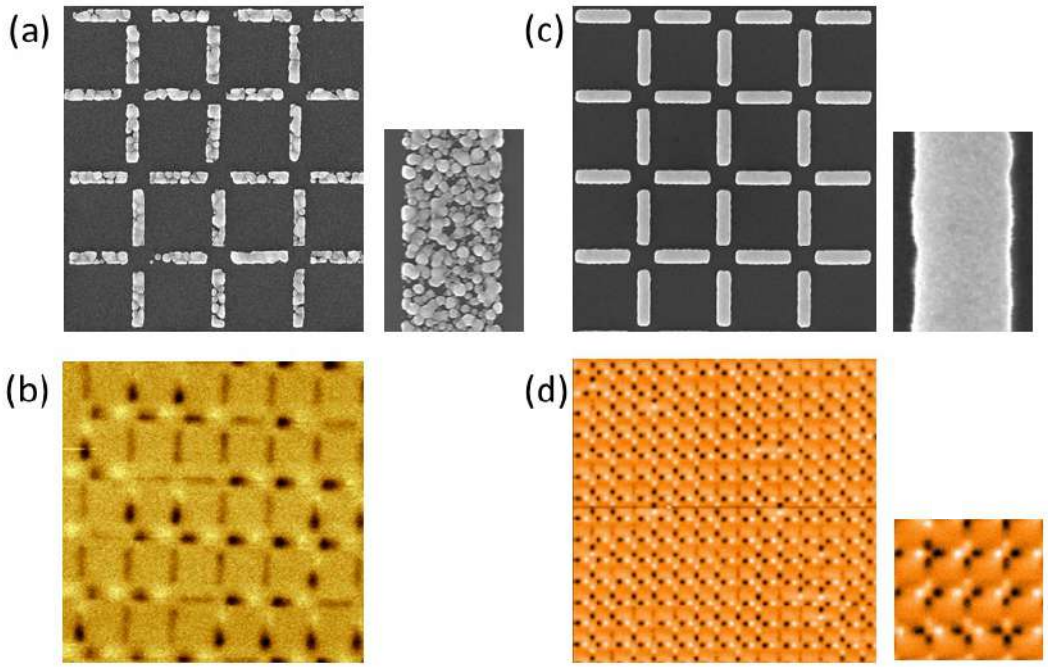

Figure 53: (**a**) SEM image of unconnected ASI lattice with Permalloy growth by constant potentiostatic electrodeposition without wettability improvement. The nanomagnets presented a granular appearance and geometries are not well defined. (**b**) MFM measurements performed in the sample presented in (a), with no good definition of magnetization in several nanomagnets. (**c**) SEM image of unconnected ASI lattice with Permalloy growth by pulsed potentiostatic electrodeposition and protocol of previous 10s dip of substrate in 2 % HF aqueous solution, differing from the previous one by the formation of uniform and conformal films. (**d**) MFM image with a scan size of 30 μm to verify the effectiveness of the electrodeposition technique to generate magnetic monodomains in ASI samples.

In Fig. 53**(c)** we present the images performed in the sample developed with the pulsed electrodeposition protocol described above. Here one can see that both geometry and film uniformity were largely improved in an unconnected lattice of 100 μm x 100

μm, whose nanomagnet dimensions are 3 μm x 200 nm with a thickness of 30 nm. MFM measurements (Fig. 53**(d)**) indicate the successful fabrication through the visualization of magnetic domains and the characteristic topologies between the vertices of the lattice formed by the nanomagnets, with all the sample nanomagnets presenting large signal of bright and dark spots. We attribute that success to the improvement on the sample wettability and formation of smaller Permalloy grains due to the pulsed potentiostatic electrodeposition mode.

After verifying the effectiveness of the electrodeposition protocol discussed in this work, four different lattices geometries with connected nanomagnets were fabricated with the purpose of moving towards electrical transport characterizations. The quality of all of them was verified by SEM, as can be seen in Figure 54.

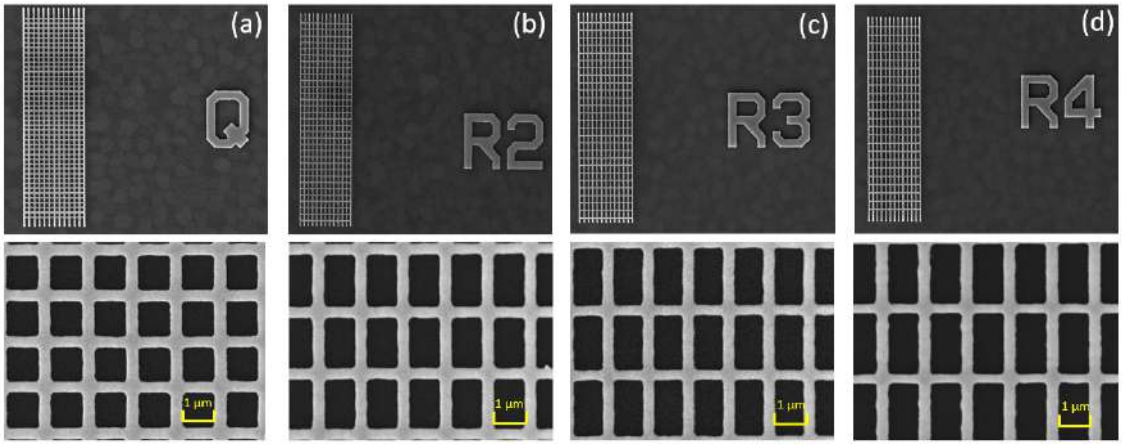

Figure 54: SEM characterization of the four geometries fabricated, with $\gamma = a/b$ varying between: (**a**) 1 (sample Q), (**b**) 2 (sample R2), (**c**) 3 (sample R3), and (**d**) 4 (sample R4).

In addition to the advantages already mentioned, the electrodeposition technique has proven to be highly effective in preventing the oxidation of materials. Generally, when using sputtering, it is necessary to grow a thin layer of another metal to protect the main material from oxidation. However, with electrodeposition, this extra step is often unnecessary, likely due to the specific conditions under which the material is deposited. EDS measurements (Fig. 55) were carried out to investigate the chemical elements present in the sample. These measurements indicated a smaller increase in the amount of oxygen over time for samples grown by electrodeposition. The samples grown by electrodeposition are thicker, as it was necessary for them to form a continuous film over the entire area of the silicon substrate for consistent analysis. A more in-depth study is needed to correlate

the formation of different types of crystalline structures in each growth method with the observed differences in oxidation.

Immediately After Growth

30 nm thick - Sputtering

Chemical formula	mass%	Atom%	Sigma	Net	K ratio	Line
O*	15.44	39.94	0.08	36253	0.0435512	K
Fe*	12.45	9.23	0.21	14852	0.0600221	K
Ni*	72.11	50.84	0.51	46884	0.3033161	K
Total	100.00	100.00				

100 nm thick - Electrodeposition

Chemical formula	mass%	Atom%	Sigma	Net	K ratio	Lin
O*	0.27	0.98	0.01	5276	0.0063378	K
Fe	2.05	2.13	0.03	23568	0.0952499	K
Ni	97.68	96.88	0.16	577104	3.7335851	K
Total	100.00	100.00				

10 Days After Growth

30 nm thick - Sputtering

Chemical formula	mass%	Atom%	Sigma	Net	K ratio	Line
O*	17.10	42.88	0.09	31762	0.0381556	K
Fe*	13.63	9.79	0.24	12639	0.0510813	K
Ni*	69.27	47.33	0.58	35220	0.2278582	K
Total	100.00	100.00				

100 nm thick - Electrodeposition

Chemical formula	mass%	Atom%	Sigma	Net	K ratio	Line
O*	0.22	0.81	0.01	3161	0.0037976	K
Fe*	2.02	2.11	0.03	16975	0.0686041	K
Ni*	97.76	97.09	0.18	421984	2.7300341	K
Total	100.00	100.00				

Figure 55: EDS of Permalloy films grown by electrodeposition and sputtering. On the left are measurements taken immediately after growth. On the right are measurements taken 10 days after growth. It is possible to notice that the presence of oxygen in samples grown by sputtering is considerably greater than those grown by electrodeposition.

One way to indirectly evaluate the ground state degeneracy of connected square geometry is through MR characterizations, which are also effective for investigating potential applications of ASIs in devices. As in the degenerate state the near disappearance of the string energy will represent the low energy required of the external magnetic field to extend it along the sample, the coercivity in degenerate systems is expected to be lower than in non-degenerate systems.

An example of the samples used for the MR measurements is presented in Fig. 56, indicating the direction of the current applied along the greater length of the lattice and the magnetic field aligned perpendicularly to the stripes. In other words, the MR measurement described here is transverse. The magnetoresistive curves obtained with an applied current of 1 mA are shown in Fig. 57. It can be observed that the resistance is high at lower fields and decreases at higher fields in all samples. This behavior is isotropic, as it was also observed for longitudinal measurements, and is similar to that presented in magnetic multilayers with GMR [65, 68].

In the case of connected ASIs, the regions formed at the vertices and the extensions of the nanomagnets can be interpreted as magnetic multilayers with different magnetiza-

tions. Changes in magnetization alter the current polarization, and the more opposite the magnetizations, the greater the depolarization. However, the MR signal obtained in the case of ASIs has a much lower intensity compared to a system with GMR of only three layers, due to the much more intense scattering, considering the large number of vertices in the lattice.

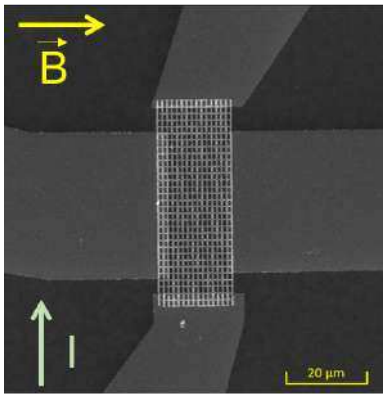

Figure 56: SEM image of a connected spin ice lattice containing copper contacts for MR characterization measurements. The external magnetic field generated by an electromagnet is applied at the sample plane, transversely to the direction of electric current input and output.

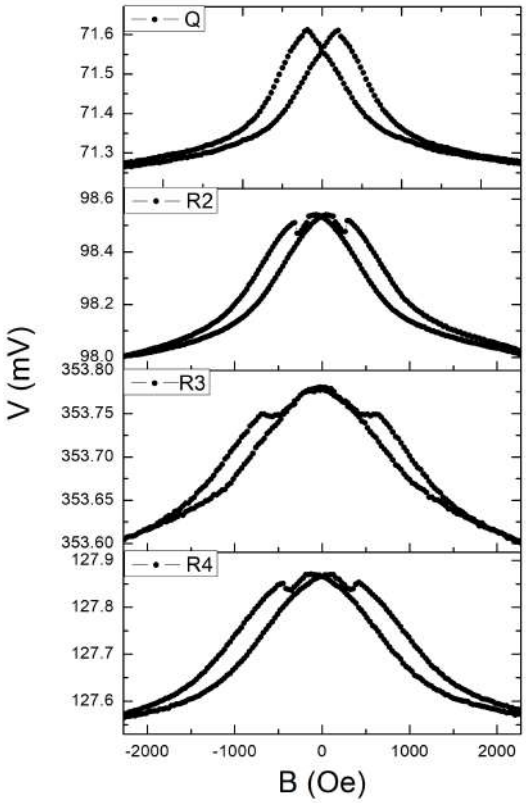

Figure 57: MR curves obtained for the samples Q, R2 R3 and R4.

In Fig. 58, **(a)**, **(b)**, **(c)**, **(d)**, respectively, are the resistance values of the samples, the coercive field of minor peaks, the coercive field at half height of the main peaks, and the magnetoresistive signals, calculated from the data in the Fig. 57. From these results it is possible to note that the lowest energy required to change the magnetization of the nanomagnets was found in the square geometry, corroborating the theoretically predicted quasi-degeneracy. Furthermore, the highest energy required to modify the magnetization of the sample was found in the $\sqrt{3}$ geometry, which is a degenerate ground state in unconnected ASI geometries and would therefore present an opposite behavior.

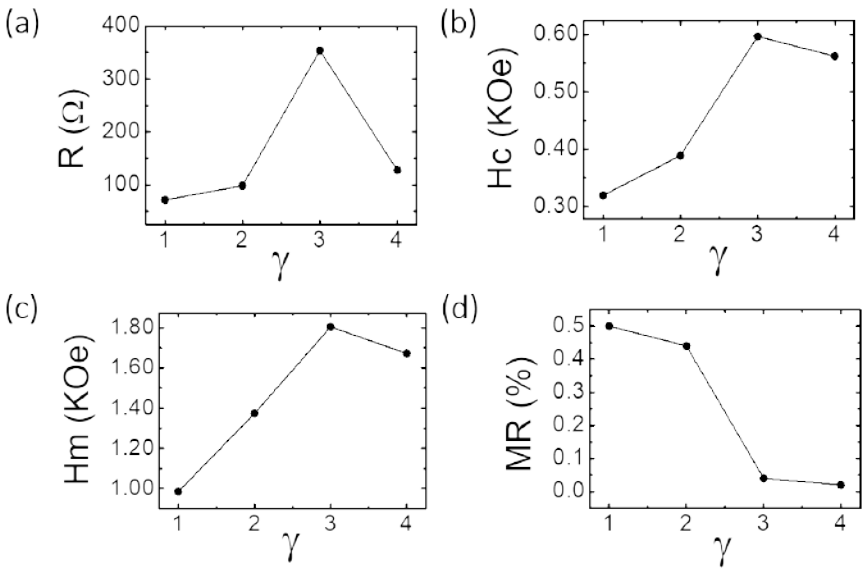

Figure 58: (**a**) Resistance, (**b**) coercive field of minor peaks, (**c**) coercive field at half height of the main peaks and (**d**) magnetoresistive signals for the different lattices.

To better understand the magnetization reversal processes under external magnetic field in these samples, we compare the experimental results obtained with results from micromagnetic simulations [20] on the connected rectangular lattice R4 of size 5μm $\times$ 5μm with the open-source GPU-based software $MUMAX^3$ [69]. The Permalloy numerical parameters used were: magnetic saturation $M_S = 860 \times 10^3$ A m^{-1}, polarization $P = 0.5$, exchange constant $A_{ex} = 13 \times 10^{-12}$ J m^{-1} and Gilbert damping $\alpha = 0.1$. Periodic boundary conditions were used with finite difference discretization for the iterations based on the Landau-Lifshitz-Gilbert (LLG) equation with cubic cell of 5 nm $\times$ 5 nm $\times$ 5 nm:

$$\frac{\partial \boldsymbol{M}}{\partial t} = \gamma \boldsymbol{H}_{\text{eff}} \times \boldsymbol{M} + \frac{\alpha}{M_S}\boldsymbol{M} \times \frac{\partial \boldsymbol{M}}{\partial t} - u\frac{\partial \boldsymbol{M}}{\partial y} + \frac{\beta}{M_S}\boldsymbol{M} \times \frac{\partial \boldsymbol{M}}{\partial y}$$

The theoretical magnetoresistive signal obtained from the simulations was achieved by using the equation proposed for anisotropic magnetoresistance (AMR) taking into account a combination of current and the magnetization according to [70, 71]:

$$\vec{\mathbf{E}} = \rho_0 \vec{\mathbf{J}} + \hat{\mathbf{m}}(\rho_{||} - \rho_{\perp})(\hat{\mathbf{m}} \cdot \vec{\mathbf{J}}), \tag{6.1}$$

Where $\rho_{||}$ and $\rho_{\perp}$ are the resistivity parallel and perpendicular to the normalized magnetization vector $\mathbf{m}$, respectively, and $\vec{\mathbf{J}}$ is the current density. We assume $\rho_{||} > \rho_{\perp}$. The physical origin of the effect is well documented, and is due to the scattering properties of electrons, depending on the orientation of magnetization [72]. The first term in Eq. 6.1 is related to the Ohm's law in the continuous medium and the second one is the first order contribution to the electric field due the AMR effect.

In Fig. 59**(a)**, we present the three main vertex configurations possible during the MR process. These configurations correspond to the T_1, T_2, and T_3 topologies. In Fig. 59**(b)**, we present the MR obtained as a result of the micromagnetic simulation. A qualitative correspondence with the experimental results is observed, allowing an understanding of the origin of the smaller peaks (pointing downwards). The discrepancies in the coercive field and saturation field values between the experimental and theoretical MR could be attributed to defects in the experimental samples, which were not considered in the simulation. These defects could create magnetostatic traps for magnetization reversal. Another consideration is that saturation occurs earlier in the simulations due to the smaller number of nanowire branches.

With the snapshots of simulations related to the most important points in the MR curve, we could conclude that the smaller resistance at magnetization saturation (point A) is related to the total uniformity in the product between current and magnetization in Eq. 6.1. In the opposite way, larger resistance is observed at zero field (point B), with the domain wall formation during magnetization reversal in nanomagnets perpendicular to the magnetic field, stimulated by the internal characteristic sample magnetic frustration. At point C, the resistance drops once some nanomagnets are already flipped, but returns to increase at point D with the formation of the T_3 configuration, which could be related to the magnetic texture, similar to the configuration of magnetic monopole formation in non-connected ASIs. Sketches of the configurations at each point can be seen in Fig. 59**(c)**.

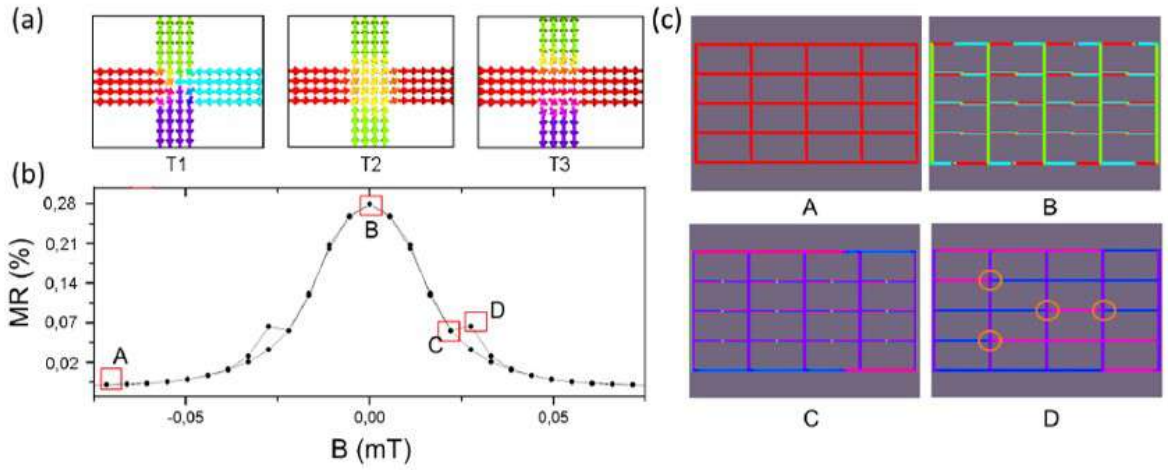

Figure 59: (**a**) Characteristic magnetic textures observed in connected vertex configurations which are related to T_1, T_2, and T_3 topologies in connected regular ASIs. (**b**) MR simulation result for the magnetic field being applied transversely to the direction of the applied electric current. (**c**) Sketch of the configurations of the highlight points in the graph (b). Different colors on the lattice indicate different magnetization directions, and the orange circles in D represents the emergent magnetic monopoles in the lattice that would be linked to the T3 topology presented in (a). Fig. taken from Ref. [20].

7 Conclusions

In this work, we performed MFM measurements on samples of rectangular lattice artificial spin ice with disconnected nanomagnets, where the ratio between the parameters a and b given by γ varied between $\sqrt{2}$, $\sqrt{3}$ and $\sqrt{4}$. Additionally, we also carried out MR measurements for these same geometries, including the square geometry, but in samples with connected nanomagnets. The objective was to analyze the freedom of pairs of emergent magnetic monopoles in these systems, in order to corroborate theoretical predictions that the sample with $\gamma = \sqrt{3}$ for disconnected nanomagnets, and with $\gamma = 1$ for connected nanomagnets, possessed a degenerate ground state and, consequently, a reduction in the string energy connecting monopoles of opposite charges.

When analyzing the results obtained from MFM images of unconnected lattices, we verified that for the sample with $\gamma = \sqrt{3}$, the vertices T_{3I} and T_{3O} representing the monopole-antimonopole pairs evolve in a much more uneven compared to other geometries, especially for external magnetic fields applied horizontally and diagonally. As the vertical distance between the nanomagnets is the same in all samples, it is believed that this is the reason why this uneven evolution was not so evident for the field applied in this direction. Furthermore, we believe that the parameter $\gamma = \sqrt{3}$ would represent the maximum distance between the nanomagnets for observing this behavior, since the sample whose $\gamma = \sqrt{4}$ presents behavior analogous to one-dimensional spin ice, due to the large distance between the nanomagnets.

Regarding the MR measurements performed on connected samples, and with the support of micromagnetic simulations, we also indirectly corroborate the degeneracy of the ground state in these systems. The small peaks recorded at a lower field in the Q samples suggest the very rapid formation and annihilation of T_3 magnetic textures, which is consistent with low-energy strings attached to them. Surprisingly, the highest energy required for the formation and annihilation of the T_3 texture was observed in the rectangular R3 geometry, opposite to what is expected for unconnected nanomagnets. The same behavior was observed with higher resistance and lower MR for that geometry. The consistency of our results is corroborated by the subsequent decrease in coercivity for the R4 geometry, evidence that coercivity is not necessarily proportional to lattice spacing; on the contrary, it is an individual characteristic of each geometry, favoring the

formation of different textures at the vertices of each lattice. In this aspect, the behavior of sample R4 once again resembles that of a one-dimensional lattice, since the distance of the transversal wires could hide the characteristic frustration of the system.

We also present a fast and low-cost production alternative for developing athermal ASI samples through a complete electrochemical route using electrodeposition. This was only possible with the implementation of a pulsed potentiostatic deposition protocol and improvement of ambient wettability. We showed through SEM characterizations that without such a protocol it would not be possible to obtain uniform, closed nanomagnets with the expected geometry. Using MFM images, we concluded that in samples made without the proposed protocol it was not possible to characterize nanomagnets with uniform magnetization throughout the sample, a necessary condition for subsequent characterization of ASI lattices.

Finally, we believe that this work could contribute to the future use of ASIs systems in transporting, processing and storing information, as well as facilitating their manufacturing methods.

Bibliography

[1] David J Griffiths. Introduction to electrodynamics fourth edition. 2021.

[2] Sergio M Rezende. *Introduction to electronic materials and devices*. Springer Nature, 2021.

[3] Sergio M Rezende. *Fundamentals of magnonics*, volume 969. Springer, 2020.

[4] Cristiano Nisoli. Frustration (s) and the ice rule: From natural materials to the deliberate design of exotic behaviors. *Frustrated Materials and Ferroic Glasses*, pages 57–99, 2018.

[5] Masafumi Udagawa, Ludovic Jaubert, et al. *Spin Ice*, volume 197. Springer, 2021.

[6] Fábio Santos Nascimento. *Estudo das propriedades térmicas e magnéticas de gelos de spin retangulares*. PhD thesis, Universidade Federal de Viçosa, Viçosa - MG, 2014.

[7] Claudio Castelnovo, Roderich Moessner, and Shivaji L Sondhi. Magnetic monopoles in spin ice. *Nature*, 451(7174):42–45, 2008.

[8] RF Wang, C Nisoli, RS Freitas, J Li, W McConville, BJ Cooley, MS Lund, N Samarth, C Leighton, VH Crespi, et al. Artificial 'spin ice'in a geometrically frustrated lattice of nanoscale ferromagnetic islands. *Nature*, 439(7074):303–306, 2006.

[9] Sandra H Skjærvø, Christopher H Marrows, Robert L Stamps, and Laura J Heyderman. Advances in artificial spin ice. *Nature Reviews Physics*, 2(1):13–28, 2020.

[10] Jason P Morgan, Aaron Stein, Sean Langridge, and Christopher H Marrows. Thermal ground-state ordering and elementary excitations in artificial magnetic square ice. *Nature Physics*, 7(1):75–79, 2011.

[11] Gabriel Alves de Oliveira. Um estudo sobre bicamadas retangulares de gelo de spin artificiais. Master's thesis, Universidade Federal de Viçosa, Viçosa - MG, 2023.

[12] Yann Perrin, Benjamin Canals, and Nicolas Rougemaille. Quasidegenerate ice manifold in a purely two-dimensional square array of nanomagnets. *Physical Review B*, 99(22):224434, 2019.

[13] FS Nascimento, LB de Oliveira, DG Duarte, CIL de Araujo, WA Moura-Melo, and AR Pereira. Conditions for an emergent gauge field in planar artificial spin ices with the dumbbell model approach. *Journal of Applied Physics*, 135(24), 2024.

[14] NanoScience Instruments. Scanning electron microscopy. https://www.nanoscience.com/techniques/scanning-electron-microscopy/. Accessed: 2024 - 06 -10.

[15] Humaira Ghazal and Nadeem Sohail. Sputtering deposition. https://www.intechopen.com/chapters/84564. Accessed: 2024-06-10.

[16] Victor Mironov. *Fundamentals of Scanning Probe Microscopy*. 2014.

[17] C.J. Muller. *AFM assisted nanomanipulation* . PhD thesis, Eindhoven University of Technology, Eindhoven, 2019.

[18] Clodoaldo Irineu Levartoski de Araujo. Magnetorresistência em ligas ferro-níquel eletrodepositadas em silício tipo-n. Master's thesis, Universidade Federal de Santa Catarina, Florianópolis - SC, 2007.

[19] Rafael Silva Gonçalves. *Estudo da Interação Magnética em Válvulas de Spin e Gelos De Spin Artificiais Unidirecionais para Aplicação em Efeito de Proximidade Supercondutora* . PhD thesis, Universidade Federal de Viçosa, Viçosa - MG, 2019.

[20] Teônis Silva de Paiva. *Magnetização e Densidade de Cargas Emergentes em Função do Campo em Gelos de Spin Artificiais* . PhD thesis, Universidade Federal de Viçosa, Viçosa - MG, 2019.

[21] S Tetal Bramwell, SR Giblin, S Calder, R Aldus, D Prabhakaran, and T Fennell. Measurement of the charge and current of magnetic monopoles in spin ice. *Nature*, 461(7266):956–959, 2009.

[22] Hikaru Takeda, Masataka Kawano, Kyo Tamura, Masatoshi Akazawa, Jian Yan, Takeshi Waki, Hiroyuki Nakamura, Kazuki Sato, Yasuo Narumi, Masayuki Hagiwara, et al. Magnon thermal hall effect via emergent su (3) flux on the antiferromagnetic skyrmion lattice. *Nature Communications*, 15(1):566, 2024.

[23] Shu Zhang and Yaroslav Tserkovnyak. Antiferromagnet-based neuromorphics using dynamics of topological charges. *Physical Review Letters*, 125(20):207202, 2020.

[24] Steven T Bramwell and Michel JP Gingras. Spin ice state in frustrated magnetic pyrochlore materials. *Science*, 294(5546):1495–1501, 2001.

[25] J Snyder, JS Slusky, RJ Cava, and P Schiffer. How 'spin ice'freezes. *Nature*, 413(6851):48–51, 2001.

[26] Ricardo Junior Campos Lopes. Análise da termodinâmica e da fenomenologia de Gelos de Spin artificiais em geometrias exóticas. Master's thesis, Universidade Federal de Viçosa, Viçosa - MG, 2016.

[27] FS Nascimento, LAS Mól, WA Moura-Melo, and AR Pereira. From confinement to deconfinement of magnetic monopoles in artificial rectangular spin ices. *New Journal of Physics*, 14(11):115019, 2012.

[28] IRB Ribeiro, FS Nascimento, SO Ferreira, WA Moura-Melo, CAR Costa, J Borme, PP Freitas, GM Wysin, CIL De Araujo, and AR Pereira. Realization of rectangular artificial spin ice and direct observation of high energy topology. *Scientific reports*, 7(1):1–9, 2017.

[29] DG Duarte, LB de Oliveira, FS Nascimento, WA Moura-Melo, AR Pereira, and CIL de Araujo. Magnetic monopole free motion in two-dimensional artificial spin ice. *Applied Physics Letters*, 124(11), 2024.

[30] Michel Le Bellac, Fabrice Mortessagne, and G George Batrouni. *Equilibrium and non-equilibrium statistical thermodynamics*. Cambridge University Press, 2004.

[31] Charles Kittel. *Introduction to Solid State Physics*. Wiley, 8 edition, 2004.

[32] Sophia Kivelson and Steven A Kivelson. Defining emergence in physics. *npj Quantum Materials*, 1(1):1–2, 2016.

[33] Denis L Nika and Alexander A Balandin. Phonons and thermal transport in graphene and graphene-based materials. *Reports on Progress in Physics*, 80(3):036502, 2017.

[34] Xiaokun Gu, Yujie Wei, Xiaobo Yin, Baowen Li, and Ronggui Yang. Colloquium: Phononic thermal properties of two-dimensional materials. *Reviews of Modern Physics*, 90(4):041002, 2018.

[35] Felix Bloch. Zur theorie des ferromagnetismus. *Zeitschrift für Physik*, 61(3):206–219, 1930.

[36] Rodrigo da Costa Silva. *Contribuições ao Estudo de Sistemas Magnéticos Frustrados: Efeitos Termodinâmicos e de Defeitos Estruturais em Gelos de Spin Artificiais*. PhD thesis, Universidade Federal de Viçosa, Viçosa - MG, 2014.

[37] C Castelnovo, R Moessner, and Shivaji Lal Sondhi. Spin ice, fractionalization, and topological order. *Annu. Rev. Condens. Matter Phys.*, 3(1):35–55, 2012.

[38] W-P_ Su, JR Schrieffer, and AJ Heeger. Soliton excitations in polyacetylene. *Physical Review B*, 22(4):2099, 1980.

[39] Daniel C Tsui, Horst L Stormer, and Arthur C Gossard. Two-dimensional magnetotransport in the extreme quantum limit. *Physical Review Letters*, 48(22):1559, 1982.

[40] Robert B Laughlin. Anomalous quantum hall effect: an incompressible quantum fluid with fractionally charged excitations. *Physical Review Letters*, 50(18):1395, 1983.

[41] Edwin H Hall et al. On a new action of the magnet on electric currents. *American Journal of Mathematics*, 2(3):287–292, 1879.

[42] K v Klitzing, Gerhard Dorda, and Michael Pepper. New method for high-accuracy determination of the fine-structure constant based on quantized hall resistance. *Physical review letters*, 45(6):494, 1980.

[43] Karol I Wysokinski. Integer and fractional quantum hall effects. *European Journal of Physics*, 21(6):535, 2000.

[44] Konrad H Fischer and John A Hertz. *Spin glasses*. Number 1. Cambridge university press, 1993.

[45] Cristiano Nisoli, Roderich Moessner, and Peter Schiffer. Colloquium: Artificial spin ice: Designing and imaging magnetic frustration. *Reviews of Modern Physics*, 85(4):1473, 2013.

[46] Roderich Moessner and Arthur P Ramirez. Geometrical frustration. *Physics Today*, 59(2):24–29, 2006.

[47] John D Bernal, Ralph H Fowler, et al. A theory of water and ionic solution, with particular reference to hydrogen and hydroxyl ions. *J. chem. Phys*, 1(8):515–548, 1933.

[48] William F Giauque and Muriel F Ashley. Molecular rotation in ice at 10 k. free energy of formation and entropy of water. *Physical review*, 43(1):81, 1933.

[49] Linus Pauling. The structure and entropy of ice and of other crystals with some randomness of atomic arrangement. *Journal of the American Chemical Society*, 57(12):2680–2684, 1935.

[50] Steven T Bramwell. Ferroelectric ice. *Nature*, 397(6716):212–213, 1999.

[51] WF Giauque and JW Stout. The entropy of water and the third law of thermodynamics. the heat capacity of ice from 15 to 273° k. *Journal of the American Chemical Society*, 58(7):1144–1150, 1936.

[52] Mark J Harris, ST Bramwell, DF McMorrow, TH Zeiske, and KW Godfrey. Geometrical frustration in the ferromagnetic pyrochlore ho 2 ti 2 o 7. *Physical Review Letters*, 79(13):2554, 1997.

[53] K Matsuhira, Y Hinatsu, K Tenya, and T Sakakibara. Low temperature magnetic properties of frustrated pyrochlore ferromagnets ho2sn2o7 and ho2ti2o7. *Journal of Physics: Condensed Matter*, 12(40):L649, 2000.

[54] David Jonathan Pryce Morris, David Alan Tennant, Santiago Andres Grigera, B Klemke, C Castelnovo, R Moessner, C Czternasty, M Meissner, KC Rule, J-U Hoffmann, et al. Dirac strings and magnetic monopoles in the spin ice dy2ti2o7. *Science*, 326(5951):411–414, 2009.

[55] Paul Adrien Maurice Dirac. Quantised singularities in the electromagnetic field. *Proceedings of the Royal Society of London. Series A, Containing Papers of a Mathematical and Physical Character*, 133(821):60–72, 1931.

[56] LA Mól, RL Silva, RC Silva, AR Pereira, WA Moura-Melo, and BV Costa. Magnetic monopole and string excitations in two-dimensional spin ice. *Journal of Applied Physics*, 106(6), 2009.

[57] LAS Mól, WA Moura-Melo, and AR Pereira. Conditions for free magnetic monopoles in nanoscale square arrays of dipolar spin ice. *Physical Review B*, 82(5):054434, 2010.

[58] The Columbia Museum of Art. Lithography: It's a process. https://www.columbiamuseum.org/news/lithography-its-process, 2023. Accessed: 2024-05-20.

[59] Joe Nabity, Lesely Anglin Compbell, Mo Zhu, and Weilie Zhou. E-beam nanolithography integrated with scanning electron microscope. In *Scanning Microscopy for Nanotechnology: Techniques and Applications*, pages 120–151. Springer, 2006.

[60] Igor Renato Bueno Ribeiro. *Estudo Experimental de Sistemas Frustrados e Dispositivos Híbridos para Aplicações em Altas e Baixas Frequências*. PhD thesis, Universidade Federal de Viçosa, Viçosa - MG, 2017.

[61] Andriele da Silva Vieira. Fabricação e Caracterização de Filmes Finos de MoS2 para Aplicações em Spintrônica. Master's thesis, Universidade Federal de Viçosa, Viçosa - MG, 2023.

[62] Hamilton Aparecido Teixeira. *Microfabricação e caracterização de transistores spintrônicos balísticos e lógicos* . PhD thesis, Universidade Federal de Viçosa, Viçosa - MG, 2021.

[63] NanoAndMore. Contact mode versus tapping mode afm. https://www.nanoandmore.com/. Accessed: 2024-06-03.

[64] RC O'Hendley. Modern magnetic materials. *Principles and Applications (Johns Wiley & Sons, Inc., 2000)*, 1999.

[65] Mario Norberto Baibich, Jean Marc Broto, Albert Fert, F Nguyen Van Dau, Frédéric Petroff, P Etienne, G Creuzet, A Friederich, and J Chazelas. Giant magnetoresistance of (001) fe/(001) cr magnetic superlattices. *Physical review letters*, 61(21):2472, 1988.

[66] Renan Pires Loreto, LA Morais, CIL De Araujo, WA Moura-Melo, AR Pereira, RC Silva, FS Nascimento, and LAS Mól. Emergence and mobility of monopoles in a unidirectional arrangement of magnetic nanoislands. *Nanotechnology*, 26(29):295303, 2015.

[67] RS Gonçalves, RP Loreto, TS De Paiva, J Borme, PP Freitas, and CIL De Araujo. Tuning magnetic monopole population and mobility in unidirectional array of nanomagnets as a function of lattice parameters. *Applied Physics Letters*, 114(14), 2019.

[68] Grünberg Binasch, Peter Grünberg, F Saurenbach, and W Zinn. Enhanced magnetoresistance in layered magnetic structures with antiferromagnetic interlayer exchange. *Physical review B*, 39(7):4828, 1989.

[69] Arne Vansteenkiste and Ben Van de Wiele. Mumax: A new high-performance micromagnetic simulation tool. *Journal of Magnetism and Magnetic Materials*, 323(21):2585–2591, 2011.

[70] Wesley BJ Fonseca, Flavio Garcia, Francesco Caravelli, and Clodoaldo IL de Araujo. Memristive effects in nanopatterned permalloy kagomé array. *Physical Review Applied*, 18(1):014070, 2022.

[71] Francesco Caravelli, Ezio Iacocca, Gia-Wei Chern, Cristano Nisoli, and Clodoaldo IL de Araujo. Anisotropic magnetomemristance. *Communications Physics*, 5(1):166, 2022.

[72] T McGuire and RL Potter. Anisotropic magnetoresistance in ferromagnetic 3d alloys. *IEEE Transactions on magnetics*, 11(4):1018–1038, 1975.

A APPENDIX

Published Articles

- Duarte, D. G., de Oliveira, L. B., Nascimento, F. S., Moura-Melo, W. A., Pereira, A. R., de Araujo, C. I. L. (2024). Magnetic monopole free motion in two-dimensional artificial spin ice. Applied Physics Letters, 124(11).
- Oliveira, L. B., Paiva, T. S., Teixeira, H. A., de Araujo, C. I. (2024). Magnetoresistive Evidence of Degeneracy in Nanomagnets Obtained by Electrodeposition Technique. Magnetism, 4(2), 104-113.
- Nascimento, F. S., de Oliveira, L. B., Duarte, D. G., de Araujo, C. I. L., Moura-Melo, W. A., Pereira, A. R. (2024). Conditions for an emergent gauge field in planar artificial spin ices with the dumbbell model approach. Journal of Applied Physics, 135(24).